

**University of Alberta**

**Role of hydrophobic effect and hydrogen bonding in surface interactions  
of polymers**

by

**Ali Faghiehnejad**

A thesis submitted to the Faculty of Graduate Studies and Research  
in partial fulfillment of the requirements for the degree of

**Doctor of Philosophy**

in

**Chemical Engineering**

**Department of Chemical & Materials Engineering**

©Ali Faghiehnejad

Fall 2013

Edmonton, Alberta

Permission is hereby granted to the University of Alberta Libraries to reproduce single copies of this thesis and to lend or sell such copies for private, scholarly or scientific research purposes only. Where the thesis is converted to, or otherwise made available in digital form, the University of Alberta will advise potential users of the thesis of these terms.

The author reserves all other publication and other rights in association with the copyright in the thesis and, except as herein before provided, neither the thesis nor any substantial portion thereof may be printed or otherwise reproduced in any material form whatsoever without the author's prior written permission.

## **Abstract**

Polymers are widely used as coatings, adhesives, biomaterials and many other applications. These successful applications rely on the physical and chemical properties of the polymer molecules and surfaces. One type of important molecular and surface interaction is hydrophobic interaction which is believed to be responsible for many interfacial and colloidal phenomena such as micelle formation, protein folding and is widely used in industrial applications such as mineral floatation. Nevertheless, direct probing of hydrophobic interaction between polymer surfaces has received only limited attention. Using polystyrene (PS) as a model polymer, the surface interactions were measured in different electrolyte solutions by a surface forces apparatus (SFA) coupled with a top-view optical microscope. A long-range attraction was observed between two PS surfaces which was found to be due to the bridging of microscopic and sub-microscopic bubbles on the PS surfaces and depended on the type and concentration of the electrolyte solutions due to ion specificity. The interaction forces in asymmetric system (PS vs. mica) were also studied and long-range repulsion was observed associated with the deformation of bubbles on PS surface. The range of the surface interactions was significantly reduced to <20 nm after degassing the solutions which indicates the important role of dissolved gases on the measured forces.

Another important type of intermolecular interaction widely used for the development of new polymers is hydrogen bonding through supramolecular chemistry where the reversible interaction is used for tuning polymer properties.

In this work, the surface interactions of poly(butyl acrylate) (PBA) functionalized with a quadruple hydrogen bonding group called UPy were investigated. The adhesion and mechanical properties of PBA-UPy were found to be significantly enhanced by the UPy groups and strongly depend on temperature, relative humidity in air and contact time. The PBA-UPy polymer shows self-healing capability. Interesting surface patterns (e.g. fingers, stripes) were observed associated with the separation of two PBA-UPy films. Our results provide new insights into the fundamental understanding of the molecular interaction mechanisms of polymers containing hydrogen bonding and hydrophobic groups and the development of novel functional materials.

## **Acknowledgement**

I would like to express my sincere gratitude to my supervisor Dr. Hongbo Zeng for his guidance, valuable suggestions, help and encouragement throughout my PhD study.

It was Dr. Zeng who introduced me into the research field of surface science and gave me precious suggestions and encouraged me to work harder and think deeper. His attitude towards research is educative for me and I learned a lot from him.

I would also like to thank people in our research group including Dr. Qingye Lu and Ling Zhang for their help.

The financial support from an NSERC Discovery Grant Award and an NSERC RTI Grant Award from the Natural Sciences and Engineering Research Council of Canada and a CFI grant from the Canada Foundation for Innovation is acknowledged.

Finally, I would like to appreciate my parents and my love, Marjan, for their endless help, support and kindness.

## Table of Contents

Chapter 1. Introduction.....	1
1.1    Intermolecular and surface forces .....	2
1.2    Surface energy .....	9
1.3    Adhesion and contact mechanics .....	12
1.3.1    Hertz model .....	13
1.3.2    Johnson-Kendal-Roberts (JKR) model.....	14
1.3.3    Derjaguin-Muller-Toporov (DMT) model .....	17
1.3.4    Maugis model .....	17
1.3.5    Effect of environmental conditions on adhesion .....	18
1.3.6    Adhesion of rough surfaces .....	20
1.3.7    Adhesion hysteresis .....	21
1.4    Experimental techniques .....	22
1.4.1    X-ray Photoelectron Spectroscopy (XPS) .....	23
1.4.2    Atomic Force Microscope (AFM) .....	24
1.4.3    Surface Forces Apparatus (SFA) .....	28
1.5    Role of hydrophobic effect and hydrogen bonding in surface interactions of polymers .....	31
Chapter 2. Hydrophobic Interactions between Polymer Surfaces: Using Polystyrene as a Model System .....	43
2.1    Introduction .....	43
2.2    Materials and experimental methods.....	46
2.3    Results and discussion.....	50

2.3.1	Effects of electrolyte type and concentration on PS-PS hydrophobic interaction .....	50
2.3.2	Effect of degassing .....	61
2.3.3	Formation of bubbles on hydrophobic polymer surfaces .....	66
2.3.4	Fracture of polymer surfaces due to the hydrophobic interactions...	72
2.3.5	Three-regime hydrophobic interaction model .....	76
2.4	Conclusion.....	83
2.5	Supporting information .....	85
	References.....	87
Chapter 3. Interaction Mechanism between Hydrophobic and Hydrophilic Surfaces: using Polystyrene and Mica as a Model System..... 103		
3.1	Introduction .....	103
3.2	Materials and Methods .....	105
3.3	Results and Discussion.....	107
3.4	Conclusion.....	123
	References.....	124
Chapter 4. Adhesion and Surface Interactions of a Self-healing Polymer with Multiple Hydrogen-bonding Groups..... 133		
4.1	Introduction .....	133
4.2	Materials and Methods .....	135
4.3	Results and discussion.....	138
4.3.1	Characterization of the polymer thin films and their surfaces.....	138

4.3.2	Contact and adhesion mechanics of polymer thin films: effects of relative humidity, temperature and time.....	141
4.3.3	Self-healing of multiple hydrogen-bonding PBA-UPy polymer ....	152
4.3.4	Characterization of surface patterns associated with adhesion tests	153
4.4	Conclusion.....	160
4.5	Supporting information .....	162
	References.....	169
Chapter 5.	Conclusion .....	175

## List of Tables

Table 1.1 Major types of non-specific intermolecular and surface interactions ...	2
Table 1.2 van der Waals and electric double-layer interaction potential between two macroscopic bodies of different geometries with separation distance $D$ ( $D \geq R$ ), and the force is given by $F(D) = -dE(D)/dD$ .....	4
Table 1.3 Distance controls and their specifications in SFA. <sup>68</sup> .....	29
Table 2.1 Effect of electrolytes on air solubility and air-water interfacial properties .....	69
Table 4.1 Surface energy components of the three probe liquids <sup>39</sup> and the two polymers PBA-UPy4.0 and PBA-UPy7.2 in ( $\text{mJ m}^{-2}$ ) estimated from the initial contact angles (Figure 4.2) using Equation 4.1 to 4.5. ....	140
Table 4.2. Surface energies of polymers PBA-UPy4.0 and PBA-UPy7.2 in $\text{mJ m}^{-2}$ estimated from JKR fitting of the loading curves in contact mechanics tests (Figure 4.3). ....	144



## List of Figures

Figure 1.1 The main features of classical contact mechanics theories. (Modified based on Horn, R.G.; Israelachvili, J.N.; Pribac, F. (1987) Journal of Colloid and Interface Science, 115, 480 – 492.) © Elsevier. ....	15
Figure 1.2 (a) Schematic of the working principle of an AFM, and (b) typical normal force versus distance curve obtained using an AFM. ....	24
Figure 1.3 (a) A section view through the center of SFA 2000. (b) Side view of SFA 2000 with piezoelectric bimorph slider and friction device attachment. (Reprinted from Israelachvili, et al. (2010) Recent advances in the surface forces apparatus (SFA) technique. <i>Reports on progress in physics</i> , 73, 036601. © IOP Publishing.) ....	29
Figure 2.1 (a) Schematic of SFA experiment setup for studying the surface interactions between two polystyrene (PS) films in various aqueous solutions. AFM image of spin-coated PS in the top right shows the surface topography of PS with root-mean-square (RMS) roughness of 0.3 nm. Multiple-beam interference fringes of equal chromatic order (FECO) for (b) two mica surfaces and (c) two PS surfaces in contact in air, and (d) the same pair of PS surfaces in aqueous solution. Note the shift in the wavelength of FECO and change in the shape (contact area) of the fringes. FECO can be used to measure the deformation and separation of surfaces and refractive index of the medium. ....	50

Figure 2.2 Force-distance profiles measured during the approaching of two PS surfaces in four different electrolytes with concentrations ranging from 0.001 to 1.0 M: (a) NaCl, (b) CaCl<sub>2</sub>, (c) HCl, and (d) CH<sub>3</sub>COOH. .... 52

Figure 2.3 FECO fringes (left), top-view optical microscope image (middle) and illustration of the interaction between two PS surfaces (right) in 1.0 M CH<sub>3</sub>COOH solution. (a) PS Surfaces were far from each other, and air bubbles were present on the PS surfaces as directly visualized by top-view optical microscope and evident by discontinuity in FECO fringes due to refractive index difference of air and water. (b) Air bubbles started to coalesce which led the two PS surfaces to get closer. (c) The PS surfaces jumped into adhesive contact and air meniscus was formed at the contact edge and propagated outward as fingering patterns (at air-water interface). The adhesive contact area was indicated by the flattened region of the FECO fringes. (d) Propagation of the air-water interface as outward fingering patterns, pointed out by the arrows in (c) and (d). (e) Associated with the detachment of PS surfaces, inward fingering patterns occurred at the air-water interface. (f) After the PS surfaces jumped apart from contact, air bubbles were normally left on the PS surfaces which were commonly damaged upon separation. .... 57

Figure 2.4 FECO fringes and top-view optical microscope images of the interaction of two PS surfaces in (a)&(c) 0.001 M and (b)&(d) 1.0 M NaCl solution before and after contact respectively. .... 60

Figure 2.5 Force-distance profiles measured between two PS surfaces interacting in different concentrations of degassed (a) NaCl and (b) CH <sub>3</sub> COOH solutions. ....	62
Figure 2.6 FECO (left) and illustration (right) of two interacting PS surfaces in degassed 0.001 M NaCl: (a) 0.5 s before jump into contact, (b) 0.2 s before jump into contact, (c) at the instant of contact ( $t=t_c$ ). The discontinuity on FECO fringes observed before the PS surfaces jumped in contact could be due to: (1) spontaneous cavitation of water between hydrophobic surfaces, and/or (2) bridging of nanoscopic bubbles. ....	63
Figure 2.7 Force-distance profiles between two PS surfaces in 0.1 M degassed CH <sub>3</sub> COOH after re-exposing to air for different times. ....	65
Figure 2.8 (a) and (b) SEM images, and (c) and (d) optical microscope images of different topographic patterns of damaged PS surfaces after separation from adhesive contact; (e) illustration of the contact shape and stress distribution for two surfaces in contact predicted by JKR and DMT theories. ....	74
Figure 2.9 A proposed three-regime hydrophobic interaction model: (I) a very long-range interaction regime from ~20 nm to hundreds of nm, due to the bridging of microscopic and sub-microscopic bubbles or electrostatic interactions; (II) an intermediate interaction regime around 10 nm (typically from several nm up to 10–20 nm), due to bridging of nanoscopic bubbles or enhanced Hamaker constant associated with enhanced proton hopping in water (so-called Grotthuss Effect); and (III)	

a short range interaction regime (from  $<1$  nm to several nm), mainly due to the water structure changes (i.e., orientation, density and hydrogen bonding of water molecules) close to the hydrophobic surfaces. The insert shows the DLVO force-distance profiles for two polystyrene surfaces interacting in 0.1 M 1:1 electrolyte (e.g., NaCl) to illustrate the range of DLVO forces and modified DLVO forces in the presence of bubbles. .... 80

Figure 3.1 Force-distance profiles of PS vs. mica during approach and separation as measured by SFA in (a and b) NaCl, (c and d)  $\text{CaCl}_2$ , (e and f) NaOH, (g and h) HCl, (i and j)  $\text{CH}_3\text{COOH}$  of concentration of 0.001 M and 1.0 M respectively. .... 110

Figure 3.2 FECO (left), the corresponding top-view optical microscope images (middle) and illustration (right) associated with the interaction between PS and mica surfaces in 0.001 M NaCl solution. (a) PS and mica surfaces were far from each other, and microscopic and submicroscopic bubbles were present on the PS surface. (b) As the two surfaces approached each other, bubbles were deformed and confined between them. (c) Bubbles were displaced to the periphery of the contact area and two surfaces were in contact. (d) As the surfaces were separated bubbles appeared again on PS surface. .... 112

Figure 3.3 (a) Schematic of the interactions between PS and mica surfaces in the presence of air bubbles. (b) Comparison between typical experimental force-distance profile of PS-mica in 0.001 and 1.0 M NaCl (in blue dots)

and the theoretical prediction by a modified DLVO model (in black line).	114
Figure 3.4 Force-distance profiles of PS vs. mica in (a) degassed 0.001 M NaCl, (b) degassed 1.0 M NaCl, and (c) degassed 0.001 M NaCl after re-exposing to air for different times.	119
Figure 3.5 Typical AFM images in air of (a) PS (rms=0.3 nm) and (b) PS treated with UV-ozone for 120 s (rms=0.3 nm).	121
Figure 3.6 (a) Normalized XPS spectra of oxygen (O1s), and (b) contact angle of water on PS surface as a function of UV-Ozone treatment time.	121
Figure 3.7 Force-distance profiles of PS vs. UV-Ozone treated PS in 0.001 M NaCl for different UV-Ozone treatment time.	123
Figure 4.1 Schematics of (a) the chemical structure of P(nBA- <i>r</i> -UPy) and (b) hydrogen bonds between two UPy groups and (c) polymer chains functionalized with UPy groups.	136
Figure 4.2 Contact angles of three liquids on the polymer films of (a) PBA-UPy4.0 and (b) PBA-UPy7.2 of thickness 120 nm vs. time, $t$ . PBA-UPy4.0 film became ruptured after contacting with water for time $t_r$ , so-called rupture time.	139
Figure 4.3 Contact diameter vs. applied load for (a,c) PBA-UPy4.0, (b,d) PBA-UPy7.2 polymer films (thickness ~ 100 nm) at (a,b) room temperature ( $T=23\text{ }^{\circ}\text{C}$ ) and (c,d) $T=40\text{ }^{\circ}\text{C}$ and two relative humidity levels of RH=0% and RH=100%. (e) Summary of adhesion forces and effective surface energies of PBA-UPy polymers at different experiment conditions.	

Loading and unloading rates were  $k_{\perp}V_{\perp}=0.3 \text{ mN s}^{-1}$  or  $V_{\perp} = 0.33 \text{ }\mu\text{m s}^{-1}$  and waiting time at the maximum load  $F_{\perp,\text{max}}=33 \text{ mN}$  was 15 s. .... 143

Figure 4.4 Contact diameter vs. external load during JKR tests under different contact time for (a) PBA-UPy4.0 and (b) PBA-UPy7.2 polymer films of thickness  $\sim 100 \text{ nm}$  at room temperature, (c) the adhesion force measured vs. total contact time and (d) the adhesion force vs. unloading rate. Note that the unloading rate was  $k_{\perp}V_{\perp}=0.3 \text{ mN s}^{-1}$  or  $V_{\perp} = 0.33 \text{ }\mu\text{m s}^{-1}$  for (a)–(c). (e) The effect of total contact time on the self-healing adhesion between two PBA-UPy7.2 films of thickness  $107 \text{ nm}$  under zero pre-loading condition ( $F_{\perp,\text{max}} = 0$ ). The red data point shows the initial adhesion of the polymer films (for  $F_{\perp,\text{max}} = 33 \text{ mN}$  and  $t_c \sim 3700 \text{ s}$ ). .... 149

Figure 4.5 FECO fringe patterns (left), corresponding top-view optical microscope images (middle) and illustrations (right) of the contact junction of PBA-UPy7.2 polymer of thickness  $100 \text{ nm}$  at  $T=40 \text{ }^{\circ}\text{C}$  and  $\text{RH}=0\%$ . Illustration in (a) shows that one surface is supported by a force measuring spring with stiffness  $k_{\perp}$  which can drive the surface close to or away from the opposing surface. .... 154

Figure 4.6 FECO fringe patterns (left), corresponding top-view optical microscope images (middle) and illustrations (right) of the contact junction of PBA-UPy7.2 polymer of thickness  $100 \text{ nm}$  at  $T=40 \text{ }^{\circ}\text{C}$  and  $\text{RH}=100\%$ . .... 155

Figure 4.7 Typical topographical AFM images of surface patterns associated with the detachment of two PBA-UPy7.2 films (of thickness $\sim 100$ nm) from adhesive contact in contact mechanics tests: (a) more viscous state, RH=100%, (b-d) more elastic state, RH=0%. The experiment temperature was $T=40$ °C.....	157
Figure 4.8 Schematic of the adhesion mechanisms of multiple hydrogen-bonding polymers. ....	159
Figure S4.1 Typical tapping mode AFM images (height) of (a, b) PBA-UPy4.0 and (c, d) PBA-UPy7.2 films of thickness 100 nm in (a, c) dry air (RH=0) and (b, d) after exposure to humid air (RH=100%).....	162
Figure S4.2 Normalized XPS spectra of (a) nitrogen (N1s) for polymer surfaces of PBA-UPy4.0 (green curve) and PBA-UPy7.2 (red curve), and (b) nitrogen (N1s) and oxygen (O1s) for PBA-UPy7.2 surface.....	163
Figure S4.3 Morphological patterns of ruptured polymer PBA-UPy4.0 films on mica after contacting with water for a time $t > t_r$ . Film thicknesses were 25, 90, 120 nm for (a)-(c), respectively. Panels (d)-(f) are higher resolution of panels (a)-(c), respectively. The original contact boundary is shown by the red line.....	163
Figure S4.4 Rupture time of polymer PBA-UPy4.0 film in contact with water droplet vs. polymer film thickness.....	164
Figure S4.5 Different stages of a thin film dewetting/rupture: (a) capillary waves always exist at the fluid-fluid interface ( $\alpha \ll h_0$ ); (b) capillary waves grow if the attractive interfacial forces across the interface surpass the	

stabilizing effects of surface tension ( $\alpha < h_0$ ); (c) rupture of the film starts through formation of holes ( $\alpha \approx h_0$ ); (d) holes grow in size due to surface tension forces leading to different morphological patterns such as polygonal and branched-like; (e) total interfacial forces between mica and air/water surfaces separated by a thin film of polymer PBA-UPy4.0...166

Figure S4.6 Microscope images of typical surface patterns (parallel or radial stripes) associated with detachment from adhesive contact of (a) more elastic polymer films (PBA-UPy7.2 at T=40 °C, RH=0%) and (b) more viscous polymer films (PBA-UPy7.2 at T=40 °C, RH=100%). Polymer film thickness ~ 100 nm.....169



## List of Symbols and Nomenclature

D	separation distance, m
F	force, N
E	interaction energy, J
A	Hamaker constant, J
$\rho_1, \rho_2$	number density of molecules
$k_B$	Boltzmann constant, $1.381 \times 10^{-23} \text{ J K}^{-1}$
T	temperature, K
$\epsilon$	dielectric permittivity
n	refractive index
$h_P$	Plank's constant, $6.626 \times 10^{-34} \text{ m}^2 \text{ Kg s}^{-1}$
$\nu_e$	electronic absorption frequency,
$1/\kappa$	Debye length, m
$z_i$	valency of ions
$e_0$	elementary charge of an electron
$\psi_0$	surface potential, V
R	radius of cylinder or sphere, m
$R_g$	radius of gyration, m
l	monomer length, m
N	number of monomers in polymer chain
$\Gamma$	number of adsorbed polymer chains per unit area, $\text{m}^{-2}$
s	mean distance between adsorbed polymer chains, m
L	thickness of brush layer, m

$\gamma$	surface energy, $\text{mJ m}^{-2}$
$W$	adhesion energy, $\text{mJ m}^{-2}$
$\sigma$	interatomic center-to-center distance, m
$\theta$	contact angle
$E_1, E_2$	Young's moduli, $\text{N m}^{-2}$
$\nu_1, \nu_2$	Poisson's ratio
$F_{\perp}$	applied normal load, N

## Chapter 1. Introduction<sup>1</sup>

Polymeric materials are central to a wide range of engineering and biomedical applications, and are used in nearly every industry and area of life from structural components for products such as computers, televisions, cars and aircrafts, to adhesives and lubricants to produce desired adhesion or friction. With the rapid development of nanotechnology and nanomaterials during the past two decades, the ratio between the surface area to the volume of the materials is getting larger and larger. Understanding the surface properties and functionality, surface contact and interactions of polymers at the molecular, nano- and micro-scale has become an extremely important and fundamental issue for the further development of new materials and novel applications.

Many industrial processes and biomedical applications rely on the fundamental interfacial interactions which occur in the thin-film regions where polymers are involved. For example, in emulsion polymerization process which is used commercially for the polymerization of monomers like vinyl acetate, styrene and several acrylates these interfacial interactions play an important role.<sup>1</sup> Also the intermolecular and interfacial interactions between biomaterial surfaces, which are polymers in many cases, and biological environments have crucial importance in understanding phenomena like bacterial adhesion or cell adhesion.<sup>2-4</sup> Moreover the automotive, aerospace and building industries are in great demand for polymers with good adhesive properties. Most polymers have

---

<sup>1</sup> A version of this chapter has been published. A. Faghihnejad, H. Zeng “Fundamentals of surface adhesion, friction and lubrication” in Polymer Adhesion, Friction and Lubrication, John Wiley & sons, 2013.

low surface free energy which results in poor adhesion properties. In this chapter, the basics of intermolecular and surface forces, surface energy, adhesion and contact mechanics are reviewed and followed by the experimental techniques used in the present study.

### 1.1 Intermolecular and surface forces

The intermolecular and surface forces can be attractive or repulsive and their range of action and magnitude can be very different. The types of forces operating between two surfaces depend on the nature of the interacting surfaces and medium between them. The major types of non-specific intermolecular and surface forces are listed in Table 1.1.

**Table 1.1** Major types of non-specific intermolecular and surface interactions

Type of interaction	Main features
Van der Waals	A forces existing between all bodies. Usually attractive, and can be repulsive.
Electrostatic (ionic, double layer)	A force existing between charged molecules/surfaces in liquid. Attractive or repulsive.
Steric	A quantum-mechanical force that is normally short-range and increases very sharply as the two molecules get close (depending geometry/shape or conformation of the interacting molecules).
Thermal fluctuation (i.e., osmotic, entropic, protrusion)	A temperature-dependent force associated with entropic confinement of molecular groups. Usually repulsive.
Hydrophobic	An attractive interaction between hydrophobic molecules or surfaces in water. Usually long-range.
Solvation	Forces associated with local structuring of solvent molecules between interacting surfaces. For water, it is normally called hydration force.
Hydrogen bonding	A special electrostatic attractive interaction involving positively charged H atoms covalently bonded to electronegative atoms (e.g. N, O).

The *Van der Waals* (VDW) forces exist between any two molecules or surfaces which can be attractive or repulsive, but always attractive between similar molecules. The van der Waals forces originate from interaction between electric dipole moments of the molecules. There are three major contributions to van der Waals forces: (1) force between two permanent dipoles (Keesom interaction), (2) force between a permanent dipole and a corresponding induced dipole (Debye interaction), and (3) force between two instantly induced dipoles (London dispersion forces).<sup>5</sup> The van der Waals interaction energy between two molecules or surfaces is given by

$$E(D) = -\frac{C_{VDW}}{D^6}, \quad (1.1)$$

and the corresponding force becomes:

$$F(D) = -\frac{dE}{dD} = -\frac{6C_{VDW}}{D^7}, \quad (1.2)$$

where  $D$  is the separation distance between the two molecules or surfaces, and  $C_{VDW}$  is a constant depending on the optical properties and geometry of the interacting bodies. The van der Waals interaction energy between two macroscopic bodies can be calculated assuming the interaction to be *additive*. Thus by integrating the interaction energy of all the molecules in one body with all the molecules in the other body, the two-body interaction energy would be obtained. The result of such analysis is summarized in Table 1.2 for different geometries in terms of Hamaker constant  $A$ ,

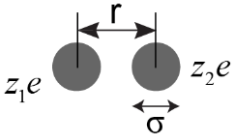
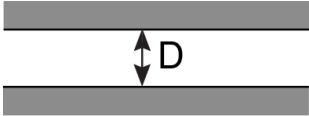
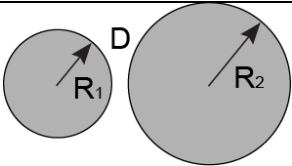
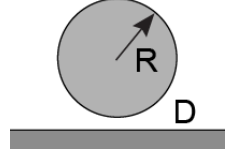
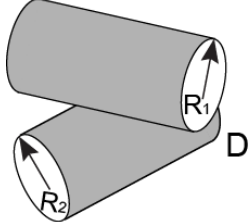
$$A = \pi^2 C_{VDW} \rho_1 \rho_2, \quad (1.3)$$

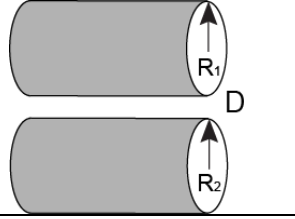
where  $\rho_1$  and  $\rho_2$  are the number density of the molecules in bodies 1 and 2 respectively. The Hamaker constant for two macroscopic bodies 1 and 2 interacting across a medium 3 is given by the Lifshitz theory as follows<sup>6</sup>

$$A_{132} \approx \frac{3}{4} k_B T \left( \frac{\varepsilon_1 - \varepsilon_3}{\varepsilon_1 + \varepsilon_3} \right) \left( \frac{\varepsilon_2 - \varepsilon_3}{\varepsilon_2 + \varepsilon_3} \right) + \frac{3h_p \nu_e}{8\sqrt{2}} \frac{(n_1^2 - n_3^2)(n_2^2 - n_3^2)}{(n_1^2 + n_3^2)^{1/2} (n_2^2 + n_3^2)^{1/2} \left\{ (n_1^2 + n_3^2)^{1/2} + (n_2^2 + n_3^2)^{1/2} \right\}}, \quad (1.4)$$

where  $k_B$  is the Boltzmann constant ( $1.381 \times 10^{-23} \text{ J K}^{-1}$ ),  $\varepsilon$  is the dielectric permittivity,  $n$  is the refractive index,  $h_p$  is the Plank's constant ( $6.626 \times 10^{-34} \text{ m}^2 \text{ Kg s}^{-1}$ ) and  $\nu_e$  is the main electronic absorption frequency.

**Table 1.2** van der Waals and electric double-layer interaction potential between two macroscopic bodies of different geometries with separation distance  $D$  ( $D \gg R$ ), and the force is given by  $F(D) = -dE(D)/dD$

Geometry of two bodies		$E_{vdw}(D)$	$E_{edl}(D)$
Two atoms or small molecules		$-C/r^6$	$\frac{z_1 z_2 e^2}{4\pi\epsilon_0 \epsilon r} \frac{e^{-\kappa(r-\sigma)}}{1 + \kappa\sigma}$
Two flat surfaces (per unit area)		$-A/12\pi D^2$	$(\kappa/2\pi) Z e^{-\kappa D}$
Two spheres		$-(\frac{R_1 R_2}{R_1 + R_2}) \frac{A}{6D}$	$(\frac{R_1 R_2}{R_1 + R_2}) Z e^{-\kappa D}$
Sphere-surface (per unit length)		$-AR/6D$	$RZ e^{-\kappa D}$
Two crossed cylinders (per unit length)		$-A\sqrt{R_1 R_2}/6D$	$\sqrt{R_1 R_2} Z e^{-\kappa D}$

Two parallel cylinders (per unit length)		$-\sqrt{\frac{R_1 R_2}{R_1 + R_2}} \frac{A}{12\sqrt{2}D^{3/2}}$	$\sqrt{\frac{R_1 R_2}{R_1 + R_2}} \sqrt{\frac{\kappa}{2\pi}} Z e^{-\kappa D}$
--	---	---	---

The *electrostatic double-layer* force is another major interaction that exists between two charged entities or surfaces in liquid solutions. When surfaces are charged in an electrolyte solution the long-range double-layer force comes to play a role. The electrostatic double-layer interaction energy between two similarly charged surfaces as a function of their separation is given by

$$E(D) \approx +C_{DL} e^{-\kappa D}, \quad (1.5)$$

where  $C_{DL}$  is a constant that depends on geometry of the surfaces, solution conditions and surface charge densities. The parameter  $1/\kappa$  is the Debye length which depends only on electrolyte conditions (i.e. type and concentration) and temperature. Debye length is the characteristic decay length of the electrostatic double-layer interaction and decreases with increasing ionic strength of the solution which is given as

$$1/\kappa = \left( \epsilon_0 \epsilon_s k_B T / \sum_i \rho_{\infty i} e_0^2 z_i^2 \right)^{1/2}, \quad (1.6)$$

where  $\epsilon_0$  is the dielectric permittivity of free space,  $\epsilon_s$  is the dielectric constant of solution,  $e_0$  is the elementary charge of a single electron,  $\rho_{\infty i}$  is the number density of  $i$ th ion in the bulk solution and  $z_i$  is the valancy of the  $i$ th ion. The electric double-layer interaction energy for different geometries is given in Table 1.2 in terms of an interaction constant  $Z$  defined as<sup>6</sup>

$$Z = 64\pi\epsilon_0\epsilon(k_B T/e_0)^2 \tanh^2(z e_0 \psi_0/4k_B T), \quad (1.7)$$

where  $\psi_0$  is the surface potential in mV and  $z$  is the electrolyte valency.

The sum of the van der Waals and double-layer forces between two surfaces form the so-called DLVO theory, after Derjaguin and Landau,<sup>7</sup> and Verwey and Overbeek.<sup>8</sup> van der Waals and double-layer forces depend differently on separation distance, the former being a power law while the later an exponential. van der Waals force is almost insensitive to solution conditions while double-layer force it is significantly affected. As a result of these differences, DLVO forces can be repulsive or attractive depending on separation distance, solution conditions and surface properties.

*Steric and bridging* forces normally occur between surfaces covered by large chain molecules (i.e. polymers, proteins) that can extend out into the solution. The net interaction between two polymer-covered surfaces includes the polymer-polymer and polymer-surface interactions, of which the former normally leads to steric forces while the latter leads to bridging forces. Polymer molecules can attach to a surface via either physical forces (physisorption) or chemical bonds (chemisorption). The state/conformation of an adsorbed polymer chain on a surface depends on parameters such as solution conditions, temperature and type of adsorption. If a polymer is completely soluble in a solvent, then the polymer chain is expanded and conversely, in a poor solvent the polymer chain tends to shrink. A polymer molecule is known as an ideal chain or freely jointed chain if the monomers of the polymer chain are able to rotate freely about each other in any direction and their movement is not affected by



the monomer-monomer interaction. In this state the polymer molecule has a random coil conformation and its dimension is defined by the radius of gyration ( $R_g$ ) as

$$R_g = \frac{l\sqrt{N}}{\sqrt{6}}, \quad (1.8)$$

where  $l$  is the monomer length and  $N$  is number of monomer units in polymer chain. The solubility and state of a polymer in a solvent also depends on temperature. The temperature in which a polymer molecule acts like a freely jointed chain ( $R=R_g$ ) is known as the theta temperature ( $T_\theta$ ) and a solvent at  $T=T_\theta$  is known as theta solvent. The surface coverage  $\Gamma$  which is the number of adsorbed polymer chains per unit area is defined as

$$\Gamma = \frac{1}{s^2}, \quad (1.9)$$

where  $s$  is the mean distance between the attachment points of adsorbed polymer chains. As two polymer-covered surfaces approach each other a repulsive osmotic force is experienced between them which is known as *steric* repulsion. The origin of this repulsive force is the unfavourable entropy associated with confining polymer chains between the two surfaces. When the surface coverage is low ( $s > R_g$ ) also known as the *mushroom* regime, the repulsive steric interaction energy between two flat surfaces is given by<sup>6</sup>

$$E(D) \approx 36\Gamma k_B T e^{-D/R_g}. \quad (1.10)$$

For high surface coverage ( $s < R_g$ ) known as the *brush* regime, the repulsive steric force per unit area (pressure) between two flat surfaces is given by the Alexander-de Gennes equation as<sup>6,9</sup>

$$P(D) = \frac{k_B T}{s^3} \left[ (2L/D)^{9/4} - (D/2L)^{3/4} \right] \quad \text{for } D < 2L, \quad (1.11)$$

where  $L$  is the thickness of the brush layer. The first term in Equation 1.11 is the osmotic repulsion and the second term is the elastic stretch energy of the chains. When two polymer-covered surfaces approach, the net interaction also depends on the forces between the polymer and the opposite surface that can be either repulsive or attractive. If the interaction between polymer and the opposite surface is attractive then it is normally referred to as the bridging forces. In general the bridging forces depend on the type of interaction (i.e., specific or non-specific) between the polymer and the surface. Therefore, there is no single expression available for describing bridging forces although linear or exponential dependence on distance have been observed in certain systems.<sup>6</sup>

*Hydrophobic force* normally refers to the attractive force between two hydrophobic particles, surfaces or molecules in water and aqueous solutions. Hydrophobic force has been reported to be much stronger than the theoretically expected van der Waals force. The first direct measurement of the force between two hydrophobic surfaces was done by Israelachvili and Pashley in 1982 which showed that the magnitude of the force is much bigger than van der Waals force.<sup>10</sup> Experimental force measurements between various hydrophobic surfaces have intended to reveal the long-range nature of the force and corresponding strong adhesion force between the surfaces.<sup>11</sup> The magnitude of the hydrophobic force also depends on hydrophobicity of the surface which is usually quantified by water contact angle measurement. The surfaces are normally considered to be hydrophobic if water contact angle exceeds 90°. Nevertheless the origin of the

hydrophobic force is not fully understood yet. Some of the suggested mechanisms include cavitation due to the metastability of a thin aqueous film separating the hydrophobic surfaces,<sup>12, 13</sup> correlated dipole interactions,<sup>14</sup> rearrangements of water molecules near hydrophobic surfaces<sup>15</sup> and the bridging of nanobubbles.<sup>16, 17</sup>

Other intermolecular and intersurface interactions that are important in understanding the various tribological phenomena include, but are not limited to, thermal fluctuation forces, solvation forces and hydrogen bonding.

## 1.2 Surface energy

It is useful to introduce the concept of surface energy which will be used throughout the discussion. The energy required to separate unit areas of two surfaces 1 and 2 from contact is referred to as work of adhesion ( $W_{12}$ ) and for identical surfaces it is called work of cohesion ( $W_{11}$ ). The energy required to increase the surface area of medium 1 by unit area is surface energy or surface tension ( $\gamma_1$ ), which is related to the work of cohesion by Equation 1.12:

$$W_{11} = 2\gamma_1. \quad (1.12)$$

For solids the term surface energy is mostly used which has the unit of energy per unit area ( $\text{J/m}^2$ ) and for liquids the term surface tension is usually used in units of force per unit length ( $\text{N/m}$ ). The two terms are dimensionally and numerically the same although the term surface energy is more general in the sense that it can be applied to both liquids and solids. The surface tension of a liquid is the magnitude of the force exerted parallel to the liquid surface divided by the length of the line over which the force acts, which is determined

by the cohesive forces between liquid molecules. Surface energy represents the excess energy that the molecules on the surface possess compared to molecules in the bulk of a material. There is a direct relationship between the surface energy and intermolecular forces of a material. The intermolecular forces that determine the boiling point and latent heat of a material also define its surface energy.<sup>6, 18</sup> Therefore it is expected that materials with high boiling point usually have high surface energy (e.g., for mercury:  $\gamma = 485 \text{ mJ/m}^2$ ,  $T_B = 357^\circ\text{C}$ ) and lower boiling point substances have lower surface energy (e.g., for neon:  $\gamma = 3.8 \text{ mJ/m}^2$ ,  $T_B = -246^\circ\text{C}$ ). For surfaces between which attractive forces can be accounted for by conventional van der Waals forces, the surface energy can be approximated by Equation 1.13:<sup>6</sup>

$$\gamma \approx \frac{A}{24\pi(\sigma/2.5)^2}, \quad (1.13)$$

where  $\sigma$  is the interatomic or intermolecular centre-to-centre distance and  $A$  is the Hamaker constant. Equation 1.13 predicts the surface energy of non-polar and non-metallic compounds well. For metals, another attractive surface interaction (i.e., metallic bond) also exists which is much stronger than conventional van der Waals forces and is due to electron exchange interactions at short separations. The metallic bonds are responsible for the much higher surface energy of metals compared to other materials. Moreover the surface energy of metals and crystalline materials is very sensitive to the lattice mismatches. Since the atoms of two mismatched lattices cannot pack together as closely as that of two perfectly matched lattices, the adhesion energy of mismatched interface is

usually significantly lower.<sup>6, 19</sup> Other contributions to the surface energy can be from charge exchange interactions such as acid-base and hydrogen bonding.

The surface and interfacial energies also determine the shape of a liquid droplet on a surface. One of the most widely used methods for measuring surface energy of a material is based on measuring the liquid droplet contact angle  $\theta$ . If a droplet of liquid 2 forms a contact angle  $\theta$  on a surface of material 1 in a medium 3, the interfacial energies are related by the well-known Young's equation as

$$\gamma_{12} + \gamma_{23} \cos \theta = \gamma_{13}. \quad (1.14)$$

If medium 3 is air, Equation 1.14 can be simplified to

$$\gamma_{12} + \gamma_2 \cos \theta = \gamma_1. \quad (1.15)$$

Only  $\gamma_2$  and  $\theta$  can be directly measured by experiments, and thus there are two unknowns in Equation 1.15:  $\gamma_{12}$  and  $\gamma_1$ . Different approaches have been suggested to resolve this problem. Zisman et al.<sup>20, 21</sup> found that a plot of  $\cos \theta$  versus  $\gamma_2$  for a homologous series of liquids (so-called Zisman Plot) usually generates a straight line and the intercept of such plot with the horizontal line  $\cos \theta = 1$  is called the critical surface tension  $\gamma_c$  which can be approximated as the solid surface energy  $\gamma_1$ . This approach should be used with caution as it is assumed that when  $\cos \theta = 1$ ,  $\gamma_{12}$  is zero which may not be necessarily true.

Another widely used method was developed by van Oss et al.<sup>22</sup> In the van Oss method the surface energy is comprised of two terms which take into account the relative contributions from Lifshitz-van der Waals ( $\gamma^{LW}$ ) and Lewis acid-base ( $\gamma^{AB}$ ) interactions as

$$\gamma = \gamma^{LW} + \gamma^{AB}. \quad (1.16)$$

The Lewis acid-base component of the surface energy is defined such that it comprises all the electron-acceptor and electron-donor interactions given by

$$\gamma^{AB} = 2\sqrt{\gamma^+\gamma^-}. \quad (1.17)$$

Based on Equations 1.16 and 1.17, the Young's equation can be written as

$$\gamma_2 (\cos \theta + 1) = 2 \left( \sqrt{\gamma_1^{LW} \gamma_2^{LW}} + \sqrt{\gamma_1^+ \gamma_2^-} + \sqrt{\gamma_1^- \gamma_2^+} \right). \quad (1.18)$$

Therefore at least three different liquids should be used in contact angle measurements to obtain the three components of the surface tension of solid  $\gamma_1^{LW}$ ,  $\gamma_1^+$ ,  $\gamma_1^-$  in Equation 1.18 and thus the total surface energy in Equation 1.16.

### 1.3 Adhesion and contact mechanics

*Adhesion* is the process of attraction between two particles or surfaces which brings them into contact. For the attracted particles or surfaces of the same material this process is normally referred to as *cohesion*. Although at first sight there might not be any direct relation between tribology and adhesion (while one deals with surfaces in *relative motion* the other tends to bring them into *contact*), adhesion plays a crucial role in tribological phenomena specifically friction and wear. Adhesion also plays an important role in a wide range of practical applications from adhesives, cold welding of metals to biomedical applications. Research on developing better adhesives in automotive and aerospace industries has continued for decades. Understanding the adhesion mechanisms of cells, bacteria and proteins on biomedical surfaces is critical for the advances of biotechnology and biomedical science. In this section, the classical theoretical

models for the adhesion or contact of two elastic surfaces are reviewed, which are commonly known as *contact mechanics* theories for analyzing surface deformations, stress distribution and strength of the adhesion between two surfaces in contact.

### 1.3.1 Hertz model

The deformation of two elastic surfaces in contact was first studied by Hertz in 1886.<sup>23</sup> Hertz assumed that no adhesion was present between the two contacting surfaces, and analyzed the stress distribution and contact geometry of two spheres as a function of compressive load ( $F_{\perp}$ ). Based on the Hertz theory, the radius  $a$  of contact area under compressive load  $F_{\perp}$  is given by Equation 1.19 for two spheres of radii  $R_1$  and  $R_2$ , Young's moduli  $E_1$  and  $E_2$  and Poisson ratio  $\nu_1$  and  $\nu_2$ , where  $R$  and  $K$  are given by Equations 1.20 and 1.21:

$$a^3 = \frac{RF_{\perp}}{K}, \quad (1.19)$$

$$\frac{1}{R} = \frac{1}{R_1} + \frac{1}{R_2}, \quad (1.20)$$

$$\frac{1}{K} = \frac{3}{4} \left[ \frac{1-\nu_1^2}{E_1} + \frac{1-\nu_2^2}{E_2} \right]. \quad (1.21)$$

And the pressure or normal stress distribution within the contact area is given by

$$P(x) = \frac{3Ka(1-x^2)^{1/2}}{2\pi R}, \quad (1.22)$$

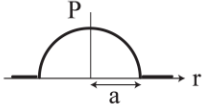
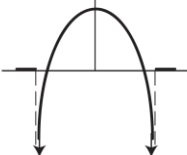
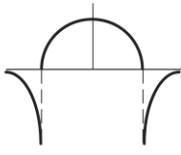
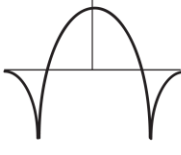
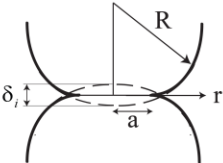
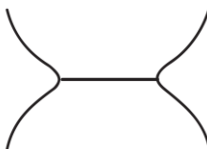
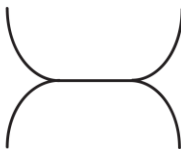
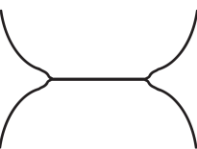
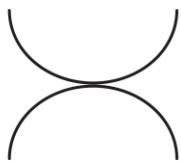
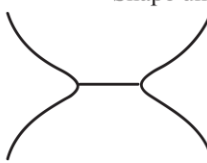
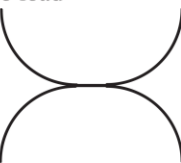
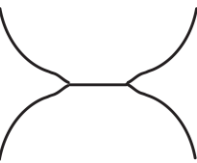
where  $x = r/a$  (see Figure 1.1). According to Equation 1.22, pressure at the centre of contact region ( $x=0$ ) is  $P(0) = 3F_{\perp}/2\pi a^2$  that is 1.5 times of the mean

pressure across the contact area. Hertz studied the contact of glass spheres by using an optical microscope and verified his theory experimentally. Based on the Hertz theory, there is infinite repulsion between the surfaces at  $D=0$ ; thus during the unloading process, the surfaces separate when contact area decreases to zero as the compressive load reduces to zero. (see Equation 1.19).

### **1.3.2 Johnson-Kendal-Roberts (JKR) model**

The main limitation of the Hertz theory is that it neglects the surface energy in the contact of two surfaces. For the first time, in 1921 Griffith pointed out the role of surface energy in elastic contact and fracture of solids.<sup>24</sup> He pointed out that during the formation of a crack in an elastic body, work must be done to overcome the attractive forces between the molecules of the two sides of the crack. He further pointed out that if the width of a crack is greater than the radius of the molecular action, the molecular attractions are negligible across the crack except near its end. Thus Griffith stated that conventional theory of elasticity is capable of analyzing the stresses correctly at all points of an elastic body except those near the end of a crack where molecular attractions cannot be neglected. For the same reason, there was a lot of controversy about the stress distribution and surface deformation at the edge of contact region until almost five decades after Griffith's paper (see Figure 1.1).<sup>25-31</sup>



Hertz	JKR	DMT	Maugis
Stress distribution under compressive load			
			
Shape under compressive load			
			
Shape under zero load			
			
Adhesion Force			
0	$3\pi\gamma R$	$4\pi\gamma R$	$(3-4)\pi\gamma R$

**Figure 1.1** The main features of classical contact mechanics theories. (Modified based on Horn, R.G.; Israelachvili, J.N.; Pribac, F. (1987) *Journal of Colloid and Interface Science*, 115, 480 – 492.) © Elsevier.

Although Griffith pointed out that surface forces deform the crack and affect the energy balance of the system, he did not quantify the model. The Hertz theory failed to predict the contact mechanics experiments by Johnson et al. using glass and rubber spheres: at low loads, the contact area was shown to be much bigger than that predicted by the Hertz theory and during the unloading process the contact radius reached a finite value before detachment.<sup>32</sup> Almost a century after the Hertz model, in 1971, Johnson, Kendal and Roberts (JKR) proposed a model for contact of elastic surfaces which takes into account the role of surface forces.<sup>32</sup> They analyzed the contact between two elastic spheres and

stated that equilibrium condition can be obtained when Equation 1.23 is satisfied:

$$\frac{dU_T}{da} = 0. \quad (1.23)$$

The total energy of the system ( $U_T$ ) consists of three terms, the stored elastic energy, the mechanical energy under the applied load and the surface energy. The appropriate expressions for these three components were derived and put into Equation 1.23 to obtain the relation shown in Equation 1.24, where  $W_{ad}$  is the adhesion energy and  $W_{ad} = 2\gamma$  for two surfaces of the same materials:

$$a^3 = \frac{R}{K} \left( F_{\perp} + 3\pi R W_{ad} + \sqrt{6\pi R F_{\perp} W_{ad} + (3\pi R W_{ad})^2} \right). \quad (1.24)$$

When  $W_{ad} = 0$  (non-adhesive) the Equation 1.24 (JRK theory) reduces to Equation 1.19 (Hertz theory). At zero load ( $F_{\perp} = 0$ ), the contact area is finite and given by:

$$a^3 = \frac{6\pi R^2 W_{ad}}{K}. \quad (1.25)$$

The adhesion force (or so-called pull-off force) is the force required to separate the spheres from adhesive contact. The corresponding adhesion force between the spheres based on JKR theory is given by:

$$F_{JKR} = 3\pi R W_{ad} / 2. \quad (1.26)$$

And the normal stress distribution within the contact area is given by Equation 1.27, where  $x = r/a$  (see Figure 1.1):

$$P(x) = \frac{3Ka}{2\pi R} (1-x^2)^{1/2} - \left( \frac{3KW_{ad}}{2\pi a} \right)^{1/2} (1-x^2)^{-1/2}. \quad (1.27)$$

### 1.3.3 Derjaguin-Muller-Toporov (DMT) model

As shown in Equation 1.27, at the edge of contact region (i.e.  $x=1$ ) the normal stress is tensile and infinite in magnitude which causes each surface to bend through a right angle along the contact edge. To resolve this unphysical situation, Derjaguin, Muller and Toporov (DMT)<sup>33</sup> proposed another model for contact mechanics. According to DMT theory, adhesion arises from attractive surface forces but the surface shape outside the contact area is *assumed* to be Hertzian and not deformed by the surface forces. The stress distribution within the contact area is also assumed to be the same as that in Hertz theory. In the DMT model, the contact radius is given by Equation 1.28 and the adhesion (pull-off) force is given by Equation 1.29:

$$a^3 = \frac{R}{K} (F_{\perp} + 2\pi R W_{ad}), \quad (1.28)$$

$$F_{DMT} = 2\pi R W_{ad}. \quad (1.29)$$

### 1.3.4 Maugis model

For a while there was some debate on which theory (JKR or DMT) is more suitable to explain the contact area dependence on the load.<sup>25-28</sup> Several models were proposed to show that either of the two theories (JKR and DMT) was a limiting case of a more general approach.<sup>29-31, 34, 35</sup> In these analyses, the intermolecular interaction between single asperities was described by a potential function. For examples, Muller et al.<sup>30, 34</sup> used a Lennard-Jones and Maugis<sup>31</sup> used a Dugdale potential function. In a unified model proposed by Maugis, the transition from JKR to DMT contact is determined by a dimensionless

parameter, which is proportional to the parameter proposed by Tabor in 1977 generally known as the so-called Tabor number ( $Ta$ ) shown in Equation 1.30<sup>25</sup>,

36

$$Ta = \left( \frac{16RW_{ad}^2}{9K^2z_0^3} \right)^{1/3}, \quad (1.30)$$

where  $z_0$  is the equilibrium separation between the two surfaces in contact, and  $W_{ad} = 2\gamma$  for the cohesion case. The Tabor number depends on the size of interacting particles, their elastic properties and the characteristic length of molecular interaction of the materials. For soft materials with large surface energy and radius (i.e.  $Ta \gg 1$ ) JKR theory applies while for hard materials with low surface energy and small radius (i.e.  $Ta \ll 1$ ) DMT model would be more appropriate. The main features of contact mechanics theories are summarized in Figure 1.1.

### 1.3.5 Effect of environmental conditions on adhesion

All of the adhesion and contact models discussed above assume contact between perfectly smooth surfaces. In reality many factors can impact the contact of two surfaces including contamination, load, surface roughness and liquid films. Dust contamination can severely reduce the adhesion of metallic surfaces by preventing direct metallic contact.<sup>37, 38</sup> In an early study on gold surfaces, Williamson *et al.* found that if surface roughness is larger than the size of dust particles then dust had little effect in preventing metallic contact. On the other hand, if the dust particle stands proud of the surface it prevents intimate metallic contact and thus decreases the adhesion.<sup>37</sup>

The presence of small amount of condensable vapours in the atmosphere is another parameter which can affect adhesion. The phenomenon of condensation of vapour molecules around the contact joints between the surfaces is known as *capillary condensation* and can have profound effect on adhesive properties of surfaces. The condensed vapour forms a liquid meniscus between the two surfaces. As a result of the surface tension of liquid and curvature effect a pressure difference occurs between the inside and outside of the meniscus known as Laplace pressure. The Laplace pressure of the meniscus pulls the two surfaces together and contributes to the adhesion force. The resulting adhesion force between a sphere of radius  $R$  on a flat surface in the presence of the liquid meniscus is given by:

$$F_{adhesion} = 4\pi R(\gamma_L \cos \theta + \gamma_{SL}) = 4\pi R\gamma_{SV}, \quad (1.31)$$

where  $\theta$  is the contact angle of liquid on solid surface,  $\gamma_L$  is the surface energy of the liquid, and  $\gamma_{SL}$  and  $\gamma_{SV}$  are interfacial tensions of solid-liquid and solid-vapour interfaces respectively. Usually  $\gamma_L \cos \theta$  exceeds  $\gamma_{SL}$  and Equation 1.31 reduces to:<sup>6</sup>

$$F_{adhesion} = 4\pi R\gamma_L \cos \theta. \quad (1.32)$$

Thus adhesion force in the presence of the liquid meniscus is mainly determined by the surface energy of the liquid. Adhesion experiments that were done in an atmosphere of different vapours corroborate Equation 1.32.<sup>39</sup> Recent experiments on the effects of relative humidity on adhesion have shown that adhesion regimes changes with humidity. Below a threshold relative humidity, adhesion is mainly determined by van der Waals forces and above that by

capillary condensation.<sup>40, 41</sup> However, it should be noted that when the condensation continues and the Kelvin radius exceeds the sphere radius  $R$  (i.e., the particle becomes effectively immersed in excess liquid), the adhesion often turns to be very low due to the disappearance of the capillary term in Equation 1.31.

### 1.3.6 Adhesion of rough surfaces

Surface roughness is another critical parameter on adhesion. Generally adhesion is conversely related to roughness for elastic surfaces.<sup>42-46</sup> The probability of intimate contact between two surfaces decrease with surface roughness which therefore decreases the adhesion. Greenwood and Williamson<sup>47</sup> modeled a rough surface on which the asperities are assumed to have the same radius  $\beta$  and a Gaussian distribution of asperity heights  $z$  with mean height  $\omega$  and standard deviation  $\sigma$  as shown in Equation 1.33. It was assumed that the contact of each asperity follows the Hertzian model:

$$f(z) = \frac{1}{\sqrt{2\pi}\sigma} e^{-(z-\omega)^2/2\sigma^2}. \quad (1.33)$$

In 1975, Fuller and Tabor analyzed the adhesion between elastic solids and the effect of roughness. The asperities on the rough surfaces were assumed to follow the Gaussian distribution (similar to the Greenwood-Williamson model) and the contact of each asperity followed the JKR model.<sup>43</sup> Fuller and Tabor showed that the adhesion decreases with the ‘adhesion parameter’ ( $1/\Delta_c$ ), defined as:

$$\frac{1}{\Delta_c} = 3\sigma \left( \frac{2K}{9\pi\beta^{1/2}\Delta\gamma} \right)^{2/3}, \quad (1.34)$$

where  $\Delta\gamma = \gamma_1 + \gamma_2 - \gamma_{12}$ . Fuller and Tabor's model is valid only when the real contact area is much lower than the apparent contact area and that contact breaks uniformly across the apparent contact area, but in real situations separation of surfaces from contact could be accompanied by crack propagation.<sup>48</sup> Other researchers applied different approaches such as using single-parameter characterization,<sup>43</sup> double-parameter characterization<sup>49</sup> and fractals<sup>50, 51</sup> to model the surface roughness and the corresponding adhesion force. Nevertheless there is no general mathematical model for defining the surface roughness. Recent experimental measurement and theoretical modeling on adhesion of rough surfaces<sup>51-54</sup> showed an exponential relation between load  $F_\perp$  and intersurface separation  $u$  as Equation 1.35, where  $u_0$  is a constant:

$$F_\perp \propto e^{-u/u_0}. \quad (1.35)$$

According to recent experiments and theoretical modelings the adhesion force decays exponentially with RMS surface roughness  $\varsigma$  as:<sup>6</sup>

$$F_{ad}(\varsigma) = F_{JKR} e^{-\varsigma/\varsigma_0}, \quad (1.36)$$

where  $\varsigma_0$  is a constant and  $F_{JKR}$  is the JKR adhesion force for smooth surfaces ( $\varsigma=0$ ).

### 1.3.7 Adhesion hysteresis

Another important aspect of adhesion process is hysteresis effects. Adhesion hysteresis is the difference between contact properties (e.g., contact

area) during loading and unloading cycles. Adhesion hysteresis is usually defined as:<sup>55</sup>

$$\Delta\gamma = (\gamma_R - \gamma_A) \geq 0, \quad (1.37)$$

where  $\gamma_A$  is the advancing surface energy during loading and  $\gamma_R$  is the receding surface energy on unloading.  $\Delta\gamma$  is a measure of energy dissipation during a complete loading-unloading cycle. Thus the adhesion energy hysteresis per unit area is given by:

$$W_{\text{hysteresis}} = 2(\gamma_R - \gamma_A) = 2\Delta\gamma. \quad (1.38)$$

For purely elastic material with no adhesion hysteresis, contact radius vs. load curve would be essentially reversible for loading and unloading processes (see for example Equation 1.24). However, for viscoelastic materials the loading and unloading (contact radius vs. load) curves deviate as a result of hysteresis. The origin of hysteresis effects can be the inherent instabilities and irreversibilities associated with loading-unloading cycles or molecular rearrangements and interdigitations at the interface.<sup>56</sup> Recent experiments on polymer surfaces have revealed that polymers of lower molecular weight show higher adhesion and adhesion hysteresis due to the higher degrees of dynamic molecular rearrangements and interdigitation at the interface.<sup>57-59</sup>

## 1.4 Experimental techniques

Various techniques have been developed for the chemical, physical and topographical characterization of material surfaces. A brief overview of some of



the most widely used techniques for surface analysis and tribological studies are discussed below.

#### **1.4.1 X-ray Photoelectron Spectroscopy (XPS)**

X-ray photoelectron spectroscopy (XPS) is also known as electron spectroscopy for chemical analysis (ESCA). XPS has been used extensively for chemical analysis of material surfaces which gives quantitative information on elemental composition of the surfaces. Following the early experiments by P.D. Innes, Moseley, Rawlinson and Robinson on photoelectric effects, Kai Siegbahn and his group at University of Uppsala in Sweden made significant progress in developing the XPS techniques in 1950s and 1960s.<sup>60</sup> XPS measurements require ultra-high vacuum (UHV) conditions. In a typical XPS measurement, a source of X-ray generates and impinges X-ray photoelectrons on the material surface, which excite the electrons of atoms on the surface and cause them to leave the surface. The kinetic energy and number of the excited electrons are measured by a detector. The kinetic energy of the excited electron is directly related to its binding energy – the energy of an electron bounded to a particular atom, which also depends on the chemical group which the atom is attached to. Thus by measuring the binding energy of the excited electrons, information about chemical nature of the surface can be obtained, which is important for understanding many tribological phenomena. The probing depth of XPS ranges from 1 to 12 nm, which makes it suitable for chemical analysis of solid films and surfaces.

### 1.4.2 Atomic Force Microscope (AFM)

The first atomic force microscope (AFM) was developed by Binnig, Quate and Gerber in 1986 as a modified combination of the scanning tunnelling microscope (STM) and the stylus profilometer which was usually used for the study of surface roughness.<sup>61</sup> AFM has been extensively used to measure interfacial forces, surface adhesion and friction, as well as to characterize surface topography at the nano- and atomic scale. The basic key components of a typical AFM include laser diode, photodiode, cantilever and tip, piezoactuator or piezoelectric tube (PZT) scanner and feedback control circuit. A schematic drawing of the working principal of AFM is shown in Figure 1.2a.

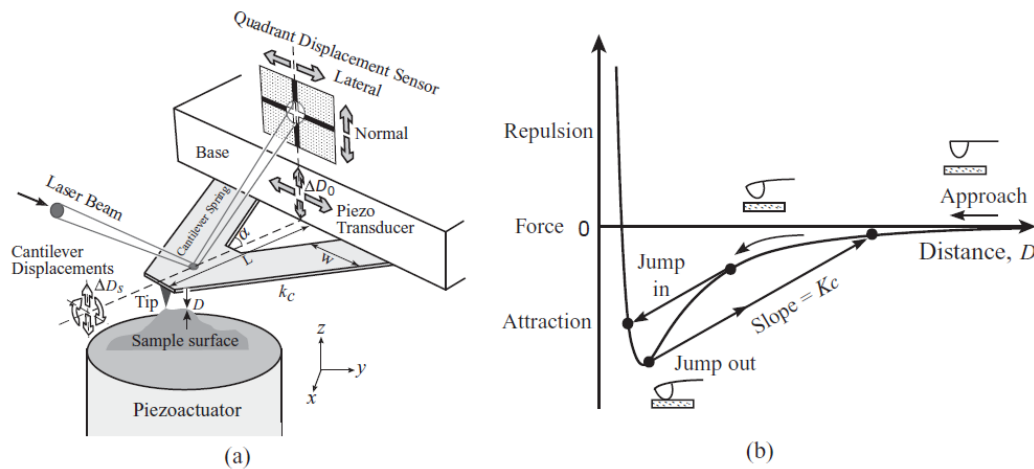


**Figure 1.2** (a) Schematic of the working principle of an AFM, and (b) typical normal force versus distance curve obtained using an AFM.

As shown in Figure 1.2, AFM consists of a flexible cantilever beam with a sharp tip at one end. The AFM cantilever is usually made of silicon or silicon nitride with typical spring constant of 0.01-100 N/m, and the radius of curvature of the tip is in the range 5-100 nm.

Forces as small as  $10^{-11}$  N between an AFM tip and a sample surface can be detected by monitoring the deflection of the cantilever beam. Different techniques have been used for measuring the deflection of the cantilever beam including optical deflection, optical interference, capacitance and tunnelling current.<sup>62</sup> Among these techniques, laser beam deflection technique is one of the most common methods used in commercial AFMs. As shown in Figure 1.2, a laser beam is directed toward the top surface of the cantilever near the tip, and the reflected laser beam is detected by a photodetector. The differential signal detected by the four quadrants of the photodetector provides a direct measurement of the cantilever deflection. The piezoelectric tube used in AFM scanner is a piezoelectric material that can expand or contract when an electric voltage is applied, which has two main designs in an AFM system. In a small-sample AFM, a sample surface is mounted on a PZT scanner which can move the sample in x, y and z directions. In a large-sample AFM, the cantilever is mounted on a PZT scanner for the measurement of large samples, which normally has relatively lower lateral resolution than the design of small-sample AFM due to the vibrations added by the cantilever movement.<sup>62</sup>

AFM is widely used for the study of surface topography with two different imaging modes: contact mode and tapping mode. In contact mode, a feedback control mechanism is employed to adjust the distance between the tip and sample surface by regulating the voltage applied to PZT scanner while keeping the cantilever deflection (or the force) constant. The movement of PZT scanner in the z direction is thus a direct measure of the roughness of the sample

surface. In tapping mode imaging, the cantilever tip does not contact the sample surface but taps it. In this mode the cantilever/tip assembly is vibrated sinusoidally by another piezo mounted above it, at a frequency slightly higher than its resonance frequency (350-400 kHz). A feedback control system is used to maintain a constant oscillating amplitude of the cantilever/tip by adjusting the distance between the tip and the sample surface in the z-direction. Thus in tapping mode, set point is the constant oscillating amplitude of the cantilever. The feedback signal sent to the z-direction piezo to keep the set point constant provides a measure of the sample roughness. Imaging in the tapping mode generally causes less damage to the sample surface than in the contact mode, thus tapping mode is preferable for measuring topography of soft surfaces. The cantilever specifications for the tapping and contact modes are normally different. Contact mode imaging is based on controlling the force between the tip and sample surface thus a relatively soft and sensitive cantilever (0.06-0.6 N/m) with low resonance frequency (13-40 kHz) is preferred. Tapping mode is based upon adjusting the oscillating amplitude of the cantilever/tip assembly, therefore a relatively stiffer cantilever (15-60 N/m) with higher resonance frequency (250-400 kHz) is more commonly used.<sup>62</sup>

One of the major applications of AFM is to monitor the interfacial and adhesion forces. A typical force-distance curve obtained using AFM is shown in the illustration of Figure 1.2b. During the force measurement, the sample surface is moved towards the tip by the z-direction piezo at a constant velocity. When the sample and the tip are far away from each other there is no force between

them. As the cantilever tip is close to the sample surface (1 to >10 nm), the intermolecular and surface forces between the tip and sample result in the deflection of the cantilever. It should be noted that force-distance curves are usually normalized by dividing the force  $F$  by the radius of curvature of the surface  $R$ , as the absolute forces exerted between two surfaces are proportional to the interacting area (or number of molecules involved). As a result the normalized forces  $F/R$  (with a unit of N/m or J/m<sup>2</sup>) obtained in one experiment can be compared with theoretical values or other experiments.

There are two limitations or challenges which should be noted in AFM force measurements. First, the radius of curvature of the AFM tip is usually not well defined in AFM experiments as a result of difficulties during the manufacturing process.<sup>63</sup> Moreover, tip wear, which is change in shape and/or size of the tip during force measurements, is one of major problems with AFM force measurement that further complicates the determination of radius of curvature. To overcome this issue, SEM has been commonly used to characterize the size and shape of AFM tips before and after experiments. However it should be noted that the tip surfaces need to be conductive for SEM imaging and the typical space resolution of SEM is of the order of 10 nm (although 1 nm resolution can be achieved in some cases).<sup>64</sup> Second, the zero separation normally cannot be determined directly in AFM force measurements, and usually the linear part of the force curve in the contact regime is assumed to be the zero separation. In most applications this will not cause any problem; but for highly deformable

surfaces, soft materials, or for situations where strong repulsive forces are present, the interpretation of the results can become rather complicated.

### **1.4.3 Surface Forces Apparatus (SFA)**

Surface forces apparatus (SFA) was originally developed by Tabor, Winterton and Israelachvili.<sup>65-67</sup> Since then significant advances have been made on the SFA design and technique such as SFA Mk I, II, III and SFA 2000, which have been widely used to measure both normal and lateral forces between surfaces in vapors and liquids in many engineering and biological systems, e.g., van der Waals forces, electrostatic forces, adhesion forces, friction and lubrication forces, hydrophobic interactions, specific and non-specific biological interactions.<sup>68-72</sup> SFA is in principle similar to AFM except that SFA measures interactions between two large surfaces while AFM measures interactions between a fine tip and a surface. It should be noted that the distances measured in SFA are absolute distances, as different from in AFM. The distance resolution in SFA is  $\sim 0.1$  nm and force sensitivity is  $\sim 1$  nN.

A section view through the center of SFA 2000 chamber is shown in Figure 1.3a. The basic components of SFA 2000 are micrometers, upper disk holder, lower disk holder attached to force springs and the main stage which contains single-cantilever spring. To manipulate the distance between the interacting surfaces, there are four levels of control which cover the angstrom to the millimeter range and their specifications are shown in Table 1.3.

**Table 1.3** Distance controls and their specifications in SFA.<sup>68</sup>

Level of control	Type of control	Positional accuracy ( $\text{\AA}$ )	Range of movement ( $\mu\text{m}$ )
Coarse	Differential micrometer	2000	2000
Medium	Differential micrometer	500	200
Fine	Differential spring mechanism	2	10
Extra fine	Piezoelectric tube	<1	1

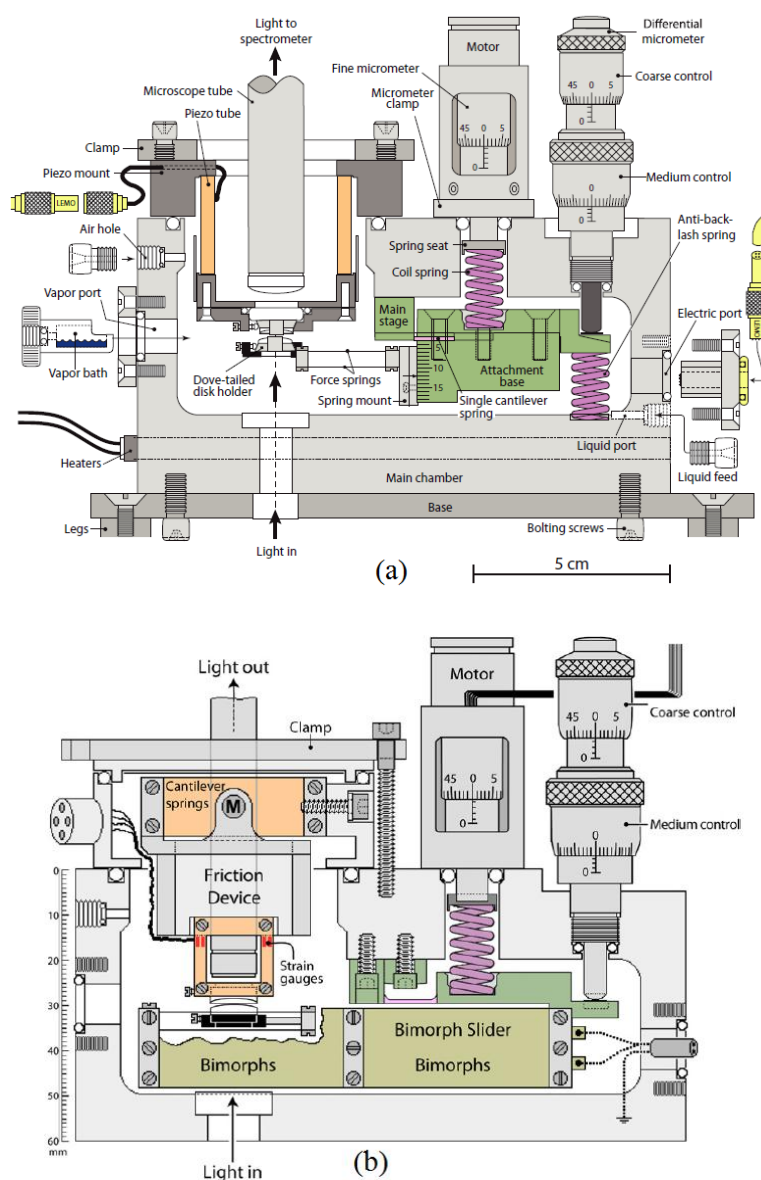


**Figure 1.3** (a) A section view through the center of SFA 2000. (b) Side view of SFA 2000 with piezoelectric bimorph slider and friction device attachment. (Reprinted from Israelachvili, et al. (2010) Recent advances in the surface forces

apparatus (SFA) technique. *Reports on progress in physics*, 73, 036601. © IOP Publishing.)

SFA measures the interactions between two curved surfaces in a crossed-cylinder configuration, which is locally corresponds to a sphere (of the same radius  $R$ ) against a flat plane based on the Derjaguin approximation,<sup>6</sup> which correlates the force  $F(D)$  between the two curved surfaces and  $E(D)$  the interaction energy per unit area between two flat surfaces:

$$E(D) = \frac{F(D)}{2\pi R}. \quad (1.39)$$

The distance is measured in SFA using an optical technique called multiple-beam interferometry (MBI) by employing fringes of equal chromatic order (FECO). Mica has commonly used as a supporting substrate in SFA experiments due to its transparent and molecularly smooth nature (for basal plane). Other materials such as sapphire, silica sheets, and polymers have also been used as supporting substrates for SFA experiments.<sup>6</sup>

SFA have also been widely used in fundamental studies of various friction and lubrication processes. A section view of SFA 2000 with the attachments for friction and lubrication experiments is shown in Figure 1.3b. The motor on the friction device is able to move the upper surface at constant or variable speed with respect to the lower surface. There are two double-cantilever springs with appropriate strain gauges attached. When a lateral force is applied to the upper surface, the springs will deflect and forces can be monitored through the voltage signals from the strain gauges. A piezoelectric bimorph slider device as shown in Figure 1.3b can be also used in SFA to measure the friction or



lubrication forces. During the experiments, a triangular input signal is input to the biomorph slider device which allows the lower surface to move at a constant speed laterally in both directions, while the friction force is still monitored through the top friction device.

### **1.5 Role of hydrophobic effect and hydrogen bonding in surface interactions of polymers**

Much progress has been made in understanding the fundamental interaction mechanisms (e.g., adhesion, friction and lubrication) of polymer surfaces and brushes in both air and liquid media.<sup>59, 73-78</sup> Nevertheless, the effect of hydrophobic interaction and hydrogen bonding on the surface interactions of polymers has not been systematically studied. The hydrophobic interaction is responsible for many interfacial and colloidal phenomena such as protein folding, micelle formation and rapid coalescence of hydrophobic droplets in colloid or emulsion systems and is extensively used in industrial processes such as mineral floatation and emulsion polymerization.<sup>1, 79</sup> Nevertheless, only limited attention has been given to the understanding and direct probing of hydrophobic interactions between polymer surfaces.<sup>1, 80, 81</sup> Moreover, the role of electrolytes and surface deformations associated with hydrophobic interaction are not well studied. Using polystyrene (PS) as a model polymer, the interaction forces between two PS surfaces were measured by SFA in different electrolyte solutions (i.e. NaCl, CaCl<sub>2</sub>, HCl, CH<sub>3</sub>COOH) of concentrations of 0.001 M to 1.0 M, and the results are discussed in chapter 2. The surface deformation

patterns associated with separation of two PS surfaces in aqueous solutions were examined and discussed based on contact mechanics theory.

In chapter 3, the role of surface hydrophobicity in polymer surface interaction was investigated by measuring the interaction forces between (1) PS and mica and (2) PS and UV-ozone treated PS in different electrolyte solutions (i.e. NaCl, CaCl<sub>2</sub>, HCl, CH<sub>3</sub>COOH, NaOH) of concentrations of 0.001 M and 1.0 M. The effect of electrolyte type and concentration and degassing of the solutions on PS-mica interactions was studied and the results were discussed in terms of ion specificity effects. A modified DLVO model was proposed to take into account the presence of microscopic and sub-microscopic bubbles on PS surfaces and the predictions of the model matched well with the experimental results.

Hydrogen bonding is another intermolecular interaction which is widely used for the development of new polymers through supramolecular chemistry. Many polymers have been synthesized with unique properties using hydrogen bonding moieties,<sup>82-85</sup> nevertheless the surface interactions of these polymers are not well understood. In chapter 4, the surface properties and adhesion mechanism of functionalized poly(butyl acrylate) (PBA) containing a quadruple hydrogen bonding group called '2-ureido-4[1*H*]-pyrimidinone' (UPy) were investigated using several complementary techniques such as SFA coupled with a top-view optical microscope and AFM. The adhesion and mechanical properties of PBA-UPy were found to be significantly enhanced by the UPy groups and strongly depend on the temperature, relative humidity in air and

contact time. Other techniques such as XPS and contact angle measurements were used for surface characterization of PBA-UPy polymers.

The conclusions based on the current study of the role of hydrophobic effect and hydrogen bonding in surface interactions of polymers are shown in Chapter 5, and some suggestions on possible future directions are also provided.

## References

- (1) Karaman, M. E.; Meagher, L.; Pashley, R. M. Surface Chemistry of Emulsion Polymerization. *Langmuir* **1993**, *9*, 1220-1227.
- (2) Dillow, A. K.; Tirrell, M. Targeted Cellular Adhesion at Biomaterial Interfaces. *Curr. Opin. Solid State Mater. Sci.* **1998**, *3*, 252-259.
- (3) Razatos, A.; Ong, Y.; Sharma, M. M.; Georgiou, G. Molecular Determinants of Bacterial Adhesion Monitored by atomic Force Microscopy. *Proc. Natl. Acad. Sci. U. S. A.* **1998**, *95*, 11059-11064.
- (4) Ong, Y.; Razatos, A.; Georgiou, G.; Sharma, M. M. Adhesion Forces between E. Coli Bacteria and Biomaterial Surfaces. *Langmuir* **1999**, *15*, 2719-2725.
- (5) London, F. The General Theory of Molecular Forces. *Trans. Faraday Soc.* **1937**, *33*, 8-26.
- (6) Israelachvili, J. N. In *Intermolecular and Surface Forces*; Academic Press: 2011.

- (7) Derjaguin, B. V.; Landau, L. Theory of the Stability of Strongly Charged Lyophobic Sols and of the Adhesion of Strongly Charged Particles in Solution of Electrolytes. *Acta Physicochimica URSS* **1941**, *14*, 633-662.
- (8) Verwey, E. J. W.; Overbeek, J. T. G. In *Theory of Stability of Lyophobic Colloids*; Elsevier Publishing Co.: Amsterdam, 1948.
- (9) de Gennes, P. G. Polymers at an Interface; A Simplified View. *Adv. Colloid Interface Sci.* **1987**, *27*, 189-209.
- (10) Israelachvili, J.; Pashley, R. The Hydrophobic Interaction is Long Range, Decaying Exponentially with Distance. *Nature* **1982**, *300*, 341-342.
- (11) Christenson, H. K.; Claesson, P. M. Direct Measurements of the Force between Hydrophobic Surfaces in Water. *Adv. Colloid Interface Sci.* **2001**, *91*, 391-436.
- (12) Craig, V. S. J.; Ninham, B. W.; Pashley, R. M. Direct Measurement of Hydrophobic Forces: A Study of Dissolved Gas, Approach Rate, and Neutron Irradiation. *Langmuir* **1999**, *15*, 1562-1569.
- (13) Christenson, H. K.; Claesson, P. M. Cavitation and the Interaction between Macroscopic Hydrophobic Surfaces. *Science* **1988**, *239*, 390-392.
- (14) Tsao, Y.; Evans, D. F.; Wennerstrom, H. Long-Range Attraction between a Hydrophobic Surface and a Polar Surface is Stronger than that between Two Hydrophobic Surfaces. *Langmuir* **1993**, *9*, 779-785.
- (15) Israelachvili, J. N.; Pashley, R. M. Measurement of the Hydrophobic Interaction between Two Hydrophobic Surfaces in Aqueous Electrolyte Solutions. *J. Colloid Interface Sci.* **1984**, *98*, 500-514.

- (16) Craig, V. S. J.; Ninham, B. W.; Pashley, R. M. Effect of Electrolytes on Bubble Coalescence. *Nature* **1993**, *364*, 317-319.
- (17) Attard, P. Nanobubbles and the Hydrophobic Attraction. *Adv. Colloid Interface Sci.* **2003**, *104*, 75-91.
- (18) Langmuir, I. Surface Chemistry. *Chem. Rev.* **1933**, *13*, 147-191.
- (19) Buckley, D. H. In *Surface effects in adhesion, friction, wear, and lubrication*; Tribology series; Elsevier Scientific Pub. Co.; New York; 1981; Vol. 5, pp 631.
- (20) Fox, H. W.; Zisman, W. A. The Spreading of Liquids on Low-Energy Surfaces. II. Modified Tetrafluoroethylene Polymers. *J. Colloid Sci.* **1952**, *7*, 109.
- (21) Fox, H. W.; Zisman, W. A. The Spreading of Liquids on Low-Energy Surfaces. III. Hydrocarbon Surfaces. *J. Colloid Sci.* **1952**, *7*, 428-442.
- (22) van Oss, C. J.; Chaudhury, M. K.; Good, R. J. Monopolar Surfaces. *Adv. Colloid Interface Sci.* **1987**, *28*, 35-64.
- (23) Hertz, H. R. Miscellaneous Papers. **1896**, 340.
- (24) Griffith, A. A. The Phenomena of Rupture and Flow in Solids. *Philos. Trans. R. Soc., A* **1921**, *221*, 163-198.
- (25) Tabor, D. Surface Forces and Surface Interactions. *J. Colloid Interface Sci.* **1977**, *58*, 2-13.
- (26) Derjaguin, B. V.; Muller, V. M.; Toporov, Y. P. On the Role of Molecular Forces in Contact Deformations (Critical Remarks Concerning Dr. Tabor's Report). *J. Colloid Interface Sci.* **1978**, *67*, 378-379.

- (27) Tabor, D. On the Role of Molecular Forces in Contact Deformations (Critical Remarks Concerning Dr. Tabor's Report). *J. Colloid Interface Sci.* **1978**, 67, 380.
- (28) Derjaguin, B. V.; Muller, V. M.; Toporov, Y. P. On Different Approaches to the Contact Mechanics. *J. Colloid Interface Sci.* **1980**, 73, 293-294.
- (29) Hughes, B. D.; White, L. R. Analytic Approximations for the Elastic Contact of Rough Spheres. *ASME J. Appl. Mech.* **1980**, 47, 194-196.
- (30) Muller, V. M.; Yushchenko, V. S.; Derjaguin, B. V. On the Influence of Molecular Forces on the Deformation of an Elastic Sphere and its Sticking to a Rigid Plane. *J. Colloid Interface Sci.* **1980**, 77, 91-101.
- (31) Maugis, D. Adhesion of Spheres: The JKR-DMT Transition using a Dugdale Model. *J. Colloid Interface Sci.* **1992**, 150, 243-269.
- (32) Johnson, K. L.; Kendall, K.; Roberts, A. D. Surface Energy and the Contact of Elastic Solids. *Proc. R. Soc. London, Ser. A* **1971**, 324, 301-313.
- (33) Derjaguin, B. V.; Muller, V. M.; Toporov, Y. P. Effect of Contact Deformations on the Adhesion of Particles. *J. Colloid Interface Sci.* **1975**, 53, 314-326.
- (34) Muller, V. M.; Yushchenko, V. S.; Derjaguin, B. V. General Theoretical Consideration of the Influence of Surface Forces on Contact Deformations and the Reciprocal Adhesion of Elastic Spherical Particles. *J. Colloid Interface Sci.* **1983**, 92, 92-101.

- (35) Hughes, B. D.; White, L. R. Implications of Elastic Deformation on the Direct Measurement of Surface Forces. *J. Chem. Soc., Faraday Trans. 1* **1980**, 76, 963-978.
- (36) Zhao, Y.; Wang, L. S.; Yu, T. X. Mechanics of Adhesion in MEMS — a Review. *J. Adhes. Sci. Technol.* **2003**, 17, 519-546.
- (37) Williamson, J. B. P.; Greenwood, J. A.; Harris, J. The Influence of Dust Particles on the Contact of Solids. *Proc. R. Soc. London, Ser. A* **1956**, 237, 560-573.
- (38) Bowden, F. P.; Tabor, D. In *The friction and lubrication of solids*; International series of monographs on physics (Oxford, England); Clarendon Press: Oxford, 1964; Vol. Part II.
- (39) McFarlane, J. S.; Tabor, D. Adhesion of Solids and the Effect of Surface Films. *Proc. R. Soc. London, Ser. A* **1950**, 202, 224-243.
- (40) DelRio, F. W.; Dunn, M. L.; Phinney, L. M.; Bourdon, C. J.; de Boer, M. P. Rough Surface Adhesion in the Presence of Capillary Condensation. *Appl. Phys. Lett.* **2007**, 90, 163104.
- (41) Wang, J.; Qian, J.; Gao, H. Effects of Capillary Condensation in Adhesion between Rough Surfaces. *Langmuir* **2009**, 25, 11727-11731.
- (42) F. P. Bowden, D. Tabor In *The Friction and Lubrication of Solids. Part I*; Clarendon Press: 1950.
- (43) Fuller, K. N. G.; Tabor, D. The Effect of Surface Roughness on the Adhesion of Elastic Solids. *Proc. R. Soc. London, Ser. A* **1975**, 345, 327-342.

- (44) Persson, B. N. J. On the Theory of Rubber Friction. *Surf. Sci.* **1998**, *401*, 445-454.
- (45) Cyprien, G. Stickiness: Some Fundamentals of Adhesion. *Integr. Comp. Biol.* **2002**, *42*, 1123-1126.
- (46) Krupp, H. Particle Adhesion Theory and Experiment. *Adv. Colloid Interface Sci.* **1967**, *1*, 111-239.
- (47) Greenwood, J. A.; Williamson, J. B. P. Contact of Nominally Flat Surfaces. *Proc. R. Soc. London, Ser. A* **1966**, *295*, 300-319.
- (48) Butt, H. J.; Kappl, M. In *Surface and Interfacial Forces*; Wiley-VCH: 2010.
- (49) Rabinovich, Y. I.; Adler, J. J.; Ata, A.; Singh, R. K.; Moudgil, B. M. Adhesion between Nanoscale Rough Surfaces I. Role of Asperity Geometry. *J. Colloid Interface Sci.* **2000**, *232*, 10-16.
- (50) Hyun, S.; Pei, L.; Molinari, J.; Robbins, M. O. Finite-Element Analysis of Contact between Elastic Self-affine Surfaces. *Phys. Rev. E* **2004**, *70*, 026117.
- (51) Persson, B. N. J. Relation between Interfacial Separation and Load: A General Theory of Contact Mechanics. *Phys. Rev. Lett.* **2007**, *99*, 125502.
- (52) Yang, C.; Persson, B. N. J. Molecular Dynamics Study of Contact Mechanics: Contact Area and Interfacial Separation from Small to Full Contact. *Phys. Rev. Lett.* **2008**, *100*, 024303.
- (53) Lorenz, B.; Persson, B. N. J. Interfacial Separation between Elastic Solids with Randomly Rough Surfaces: Comparison of Experiment with Theory. *J. Phys.: Condens. Matter* **2009**, *21*, 015003.



- (54) Benz, M.; Rosenberg, K. J.; Kramer, E. J.; Israelachvili, J. N. The Deformation and Adhesion of Randomly Rough and Patterned Surfaces. *J. Phys. Chem. B* **2006**, *110*, 11884-11893.
- (55) Bhushan, B. In *Springer Handbook of Nanotechnology*; Springer- Verlag: Berlin, 2003.
- (56) Landman, U.; Luedtke, W. D.; Burnham, N. A.; Colton, R. J. Atomistic Mechanisms and Dynamics of Adhesion, Nanoindentation, and Fracture. *Science* **1990**, *248*, 454-461.
- (57) Maeda, N.; Chen, N.; Tirrell, M.; Israelachvili, J. N. Adhesion and Friction Mechanisms of Polymer-on-Polymer Surfaces. *Science* **2002**, *297*, 379-382.
- (58) Chen, N.; Maeda, N.; Tirrell, M.; Israelachvili, J. Adhesion and Friction of Polymer Surfaces: The Effect of Chain Ends. *Macromolecules* **2005**, *38*, 3491-3503.
- (59) Zeng, H.; Maeda, N.; Chen, N.; Tirrell, M.; Israelachvili, J. Adhesion and Friction of Polystyrene Surfaces Around T<sub>g</sub>. *Macromolecules* **2006**, *39*, 2350-2363.
- (60) Siegbahn, K.; Vetenskaps-societeten i Upsala In *ESCA; atomic, molecular and solid state structure studied by means of electron spectroscopy*; Nova acta regiae societatis scientiarum Upsaliensis; Almqvist & Wiksells: Uppsala, 1967; Vol. ser. 4:20, pp 282.
- (61) Binnig, G.; Quate, C. F.; Gerber, C. Atomic Force Microscope. *Phys. Rev. Lett.* **1986**, *56*, 930-934.
- (62) Bhushan, B. Nanotribology and Nanomechanics. **2008**, 1516.

- (63) Bhushan, B. Modern Tribology Handbook. **2001**.
- (64) Butt, H.; Cappella, B.; Kappl, M. Force Measurements with the Atomic Force Microscope: Technique, Interpretation and Applications. *Surf. Sci. Rep.* **2005**, *59*, 1-152.
- (65) Tabor, D.; Winterton, R. H. S. The Direct Measurement of Normal and Retarded Van Der Waals Forces. *Proc. R. Soc. London, Ser. A* **1969**, *312*, pp. 435-450.
- (66) Israelachvili, J. N.; Tabor, D. Measurement of Van Der Waals Dispersion Forces in the Range 1.4 to 130 nm. *Nature Phys. Sci.* **1972**, *236*, 106.
- (67) Israelachvili, J. N.; Tabor, D. The Measurement of Van Der Waals Dispersion Forces in the Range 1.5 to 130 Nm. *Proc. R. Soc. London, Ser. A* **1972**, *331*, 19-38.
- (68) Israelachvili, J.; Min, Y.; Akbulut, M.; Alig, A.; Carver, G.; Greene, W.; Kristiansen, K.; Meyer, E.; Pesika, N.; Rosenberg, K.; Zeng, H. Recent Advances in the Surface Forces Apparatus (SFA) Technique. *Rep. Prog. Phys.* **2010**, *73*, 036601.
- (69) Israelachvili, J. N.; Adams, G. E. Measurement of Forces between Two Mica Surfaces in Aqueous Electrolyte Solutions in the Range 0-100 nm. *J. Chem. Soc. , Faraday Trans. 1* **1978**, *74*, 975-1001.
- (70) Israelachvili, J. N.; McGuiggan, P. M. Adhesion and Short-Range Forces between Surfaces. Part I New Apparatus for Surface Force Measurements. *J. Mater. Res.* **1990**, *5*, 2223-2231.

- (71) Israelachvili, J. Direct Measurements of Forces between Surfaces in Liquids at the Molecular Level. *Proc. Natl. Acad. Sci. U. S. A.* **1987**, *84*, 4722-4724.
- (72) Israelachvili, J. N.; Adams, G. E. Direct Measurement of Long Range Forces between Two Mica Surfaces in Aqueous KNO<sub>3</sub> Solutions. *Nature* **1976**, *262*, 774-776.
- (73) Taunton, H. J.; Toprakcioglu, C.; Fetters, L. J.; Klein, J. Forces between Surfaces Bearing Terminally Anchored Polymer Chains in Good Solvents. *Nature* **1988**, *332*, 712-714.
- (74) Klein, J. Shear, Friction and Lubrication Forces between Polymer-Bearing Surfaces. *Annu. Rev. Mater. Sci.* **1996**, *26*, 581-612.
- (75) Leger, L.; Raphael, E.; Hervet, H. Surface-Anchored Polymer Chains: Their Role in Adhesion and Friction. *Adv. Polym. Sci.* **1999**, *138*, 185-225.
- (76) Creton, C.; Kramer, E. J.; Brown, H. R.; Hui, C. Adhesion and Fracture of Interfaces between Immiscible Polymers: From the Molecular to the Continuum Scale. *Adv. Polym. Sci.* **2002**, *156*, 53-136.
- (77) Maeda, N.; Chen, N.; Tirrell, M.; Israelachvili, J. N. Adhesion and Friction Mechanisms of Polymer-on-Polymer Surfaces. *Science* **2002**, *297*, 379-382.
- (78) Zeng, H.; Zhao, B.; Israelachvili, J. N.; Tirrell, M. Liquid- to Solid-Like Failure Mechanism of Thin Polymer Films at Micro- and Nanoscales. *Macromolecules* **2010**, *43*, 538-542.
- (79) Meyer, E. E.; Rosenberg, K. J.; Israelachvili, J. Recent Progress in Understanding Hydrophobic Interactions. *Proc. Natl. Acad. Sci. U. S. A.* **2006**, *103*, 15739-15746.

- (80) Schmitt, F. -.; Ederth, T.; Weidenhammer, P.; Claesson, P.; Jacobasch, H. -. Direct Force Measurements on Bulk Polystyrene using the Bimorph Surface Forces Apparatus. *J. Adhes. Sci. Technol.* **1999**, *13*, 79-96.
- (81) Meagher, L.; Craig, V. S. J. Effect of Dissolved Gas and Salt on the Hydrophobic Force between Polypropylene Surfaces. *Langmuir* **1994**, *10*, 2736-2742.
- (82) Sijbesma, R. P.; Beijer, F. H.; Brunsveld, L.; Folmer, B. J. B.; Hirschberg, J. J. K. K.; Lange, R. F. M.; Lowe, J. K. L.; Meijer, E. W. Reversible Polymers Formed from Self-Complementary Monomers using Quadruple Hydrogen Bonding. *Science* **1997**, *278*, 1601-1604.
- (83) Sivakova, S.; Bohnsack, D. A.; Mackay, M. E.; Suwanmala, P.; Rowan, S. J. Utilization of a Combination of Weak Hydrogen-Bonding Interactions and Phase Segregation to Yield Highly Thermosensitive Supramolecular Polymers. *J. Am. Chem. Soc.* **2005**, *127*, 18202-18211.
- (84) Cordier, P.; Tournilhac, F.; Soulie-Ziakovic, C.; Leibler, L. Self-Healing and Thermoreversible Rubber from Supramolecular Assembly. *Nature* **2008**, *451*, 977-980.
- (85) Montarnal, D.; Tournilhac, F.; Hidalgo, M.; Couturier, J.; Leibler, L. Versatile One-Pot Synthesis of Supramolecular Plastics and Self-Healing Rubbers. *J. Am. Chem. Soc.* **2009**, *131*, 7966-7967.

## Chapter 2. Hydrophobic Interactions between Polymer Surfaces: Using Polystyrene as a Model System<sup>2</sup>

### 2.1 Introduction

The hydrophobic effect plays a critical role for a wide range of phenomena such as low solubility of nonpolar solutes in water,<sup>1,2</sup> strong adhesion between solid hydrophobic surfaces in water,<sup>1</sup> micelle formation,<sup>1,3</sup> protein folding,<sup>1,4</sup> slip boundary layer for flow of water through hydrophobic channels<sup>1,5</sup> and rapid coalescence of hydrophobic liquid droplets in colloid or emulsion systems.<sup>1,3</sup> The above mentioned phenomena are all manifestations of the hydrophobic interaction either between hydrophobic molecules or surfaces in water and aqueous solutions. Hydrophobic force for macroscopic surfaces is generally defined as the long range attractive force exhibited by hydrophobic surfaces in aqueous solutions.<sup>4,6,7</sup> The first direct force measurement between two hydrophobic surfaces was reported by Israelachvili and Pashley in 1982 which showed that the magnitude of the force is greater than van der Waals force.<sup>4</sup> Over the past three decades there has been much work on hydrophobic interaction but no single explanation or model could describe all the experimental results available. The range and magnitude of the hydrophobic force differs a lot in the published data. One of the possible reasons that could lead to such large differences among previous experimental results was

---

<sup>2</sup> A version of this chapter has been published. A. Faghihnejad, H. Zeng *Soft Matter*, 8, 2746-59 (2012).

considered to be surface preparation methods. The methods most commonly used include Langmuir-Blodgett (LB) deposition of surfactants,<sup>8,9</sup> in situ adsorption of surfactants<sup>4,9,10</sup> and silanated surfaces (on silica or mica).<sup>11,12</sup> In some cases the produced hydrophobic surface was found to be not very stable. For example it was reported that hydrophobic surfactant surfaces could be sensitive to high electrolyte concentration<sup>9,13</sup> or change of temperature.<sup>14,15</sup> The surfactant concentration in the bulk solution could also affect the resulting force-distance curves.<sup>13</sup> It was reported that surfactants in hydrophobic self-assembled monolayer could overturn and rearrange into charged bilayer patches leading to a long-range attractive electrostatic force, which should not be considered as the genuine hydrophobic force.<sup>1,16,17</sup>

In spite of the enormous amount of experimental and theoretical work reported, the actual mechanisms behind the hydrophobic force are still not fully understood. Some of the mechanisms and models proposed for hydrophobic interaction include: cavitation due to the metastability of a thin aqueous film separating the hydrophobic surfaces,<sup>6,8</sup> correlated dipole interactions,<sup>18</sup> entropic effects due to molecular rearrangements of water molecules near hydrophobic surfaces<sup>19-21</sup> and bridging of submicroscopic bubbles.<sup>7,11,22-24</sup>

To better understand the hydrophobic interactions in various environmental conditions and systems, it is critical to study the impact of different environmental parameters. Several studies have considered the dependence of hydrophobic force on several factors such as electrolyte types and their concentration, temperature and dissolved gas. While some studies reported

that electrolytes had no effect on the measured hydrophobic force between surfactant monolayers<sup>10</sup>, silanated glass<sup>11</sup> and polymer surfaces,<sup>25,26</sup> others showed that the hydrophobic interaction of surfactant monolayer,<sup>9,18</sup> LB deposited surfactant and silanated mica decreased with increasing concentration of electrolytes.<sup>27,28</sup> The effect of temperature on the hydrophobic force has not been studied thoroughly and the previous results were not very consistent.<sup>11,14,15</sup> Several studies on the effect of dissolved gas have revealed that removal of the dissolved gas in water could decrease the range and magnitude of the hydrophobic force.<sup>5,6,12,25,26,29,30</sup> This observation supports the model of presence of submicroscopic bubbles on hydrophobic surfaces as the origin of long-range hydrophobic force.

Significant progress has been made in understanding the fundamental interaction mechanisms (e.g., adhesion, friction and lubrication) of polymer surfaces and brushes in both air and liquid media over the past three decades.<sup>31-42</sup> However, as summarized above, most of the previous experimental studies on the hydrophobic interactions focused on chemically bonded or self-assembled surfactant surfaces. Only few studies have focused on the hydrophobic interactions in polymer materials, which play critical roles in numerous engineering applications and biological systems.<sup>3,25,26,43</sup> Polymer surfaces are easy to prepare and are generally stable under different aqueous solution conditions (i.e., ionic strength, pH) and do not have problems associated with the surface preparation method, monolayer overturning or susceptibility to high salt concentrations as that in the case of surfactant coatings.<sup>25</sup>

In this study, the surface forces between two polystyrene thin films were measured by a Surface Forces Apparatus (SFA) in four different electrolyte solutions (HCl, NaCl, CaCl<sub>2</sub> and CH<sub>3</sub>COOH) of concentration ranging from 0.001 to 1.0 M. The effects of electrolyte type and concentration, as well as dissolved gases on the hydrophobic interaction between polystyrene surfaces were examined. Our results provide an insight into the basic hydrophobic interactions of polymer materials, and may also shed light on certain characteristics of the hydrophobic interactions in biological systems.

## **2.2 Materials and experimental methods**

Polystyrene (PS) of Mw=1,000,000 g/mol and Mw/Mn~1.10 (Polysciences Inc., USA) was used as received. PS solution was prepared by dissolving the PS in toluene (Fisher Scientific, Canada, high-performance liquid chromatography (HPLC) grade, 99.9%) which was filtered using 0.2 µm filter before use. Thin PS films were prepared by spin-coating two droplets of PS solution on a mica substrate glued on a silica disk and drying under reduced pressure overnight (>12 h) to remove the solvent and leave a film of uniform thickness, and then were mounted into the SFA chamber. Film thickness was measured in situ using an optical technique employing fringes of equal chromatic order (FECO) in the SFA, and the thicknesses of all the polymer films used in this study were 100±5 nm. Milli-Q water with a resistance of ≥ 18.2 MΩ cm was used for preparing the aqueous solutions needed. Acetic acid (Fisher Scientific, Canada, >99%) and hydrochloric acid (Fisher Scientific, Canada, ACS Grade) were used as received. High-purity anhydrous sodium chloride



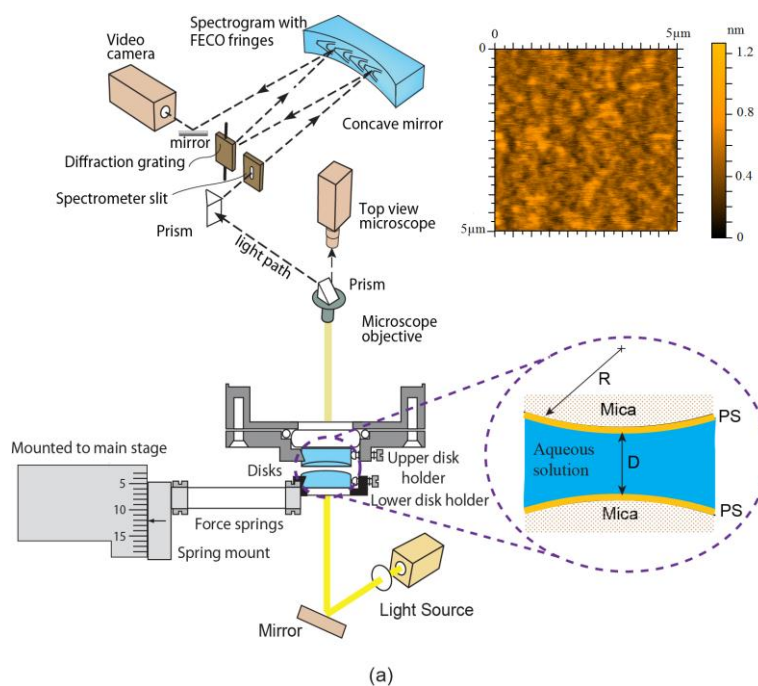
(Sigma-Aldrich, 99.999+%) and anhydrous calcium chloride (Sigma-Aldrich 99.99+%, and Fisher Scientific Canada >99.9%) were used as received (sealed in glass or quartz ampules) or calcined in an oven at 600 °C for >5 hr following the same method reported by Pashley, Ninham, et al. to remove the possible trace organic impurity<sup>10,25,27</sup> before use. Both calcined and uncalcined salts were used in the surface forces measurements, to test the effect of possible trace organic impurities in the salts, and no difference was observed, indicating trace organic impurity was not an issue in this study. All the operations were conducted in a dust-free laminar flow cabinet.

Surface roughness and topography of the polymer surfaces was characterized using an atomic force microscope (AFM) (Agilent Technologies 5500, Agilent, Santa Barbara, CA, USA). A scanning electron microscope (SEM) (Hitachi S2500, Japan) and an optical microscope (Axioskop 40, Carl Zeiss, Germany) were also employed to examine the surface topography of PS films after the force measurements.

An SFA (Surforce LLC, Santa Barbara, CA, USA) was used to investigate the interaction forces between two PS surfaces in different electrolyte solutions. Detailed setup for SFA experiments has been reported previously.<sup>44-46</sup> Briefly, a thin mica sheet of 1-5  $\mu\text{m}$  was glued onto a cylindrical silica disk (radius  $R=2$  cm). The back surfaces of mica substrates were coated with  $\sim 50$  nm thick semi-reflective layer of silver, required to obtain multiple-beam interference fringes of equal chromatic order (FECO), which were used to monitor the surface separation, shape, deformations and the contact area in real

time and in situ. The two curved mica surfaces were then mounted into the SFA chamber in a crossed-cylinder geometry, which roughly corresponded to a sphere of radius  $R$  approaching a flat surface based on the Derjaguin approximation.<sup>2</sup> A schematic drawing of the SFA experimental setup for measuring hydrophobic interactions between two PS surfaces is shown in Figure 2.1. The distance  $D=0$  was set as the adhesive contact between two PS surfaces in air. The normal forces between the PS surfaces in aqueous solutions were measured by moving the lower PS surface supported by a double-cantilever ‘force springs’ by a distance  $\Delta D_{\text{applied}}$ . The actual distance that the surfaces move relative to each other  $\Delta D_{\text{meas}}$  was measured by multiple beam interferometry (MBI). The changed force  $\Delta F$  between the surfaces at a separation  $D$  was therefore calculated based on the Hooke’s Law  $\Delta F(D) = k (\Delta D_{\text{applied}} - \Delta D_{\text{meas}})$ , where  $k$  was the spring constant and  $k=883$  N/m in this study. When  $\partial F(D)/\partial D > k$ , there was a mechanical instability and the lower surface jumped either toward or away from the upper surface during approach or separation processes, respectively. During the experiments, FECO fringes and top-view microscope images were recorded simultaneously to monitor and visualize the surface separation, deformations in real time, which were later analyzed and compared to obtain the full picture at the nano- and micro-scales. In this study, at least three different positions were tested for the same set of PS surfaces, and the experiments were reproduced for at least three times for each solution condition. All the experiments were conducted at room temperature.

Degassing of the solutions was carried out following the same method reported by Meyer et al.<sup>47</sup> by using a 50 mL filtering flask attached to an oil-free vacuum pump under pressure of 50 mmHg. A Teflon-coated stir bar and several small pieces of Teflon tubing were put in the bottom of the flask placed on a stir plate. The stir bar was set to rotate at 500 rpm when the vacuum pump pumped out the air. Although bubbles were no longer visible after 30 min, the process was carried out over 10 hours before the start of SFA experiments.



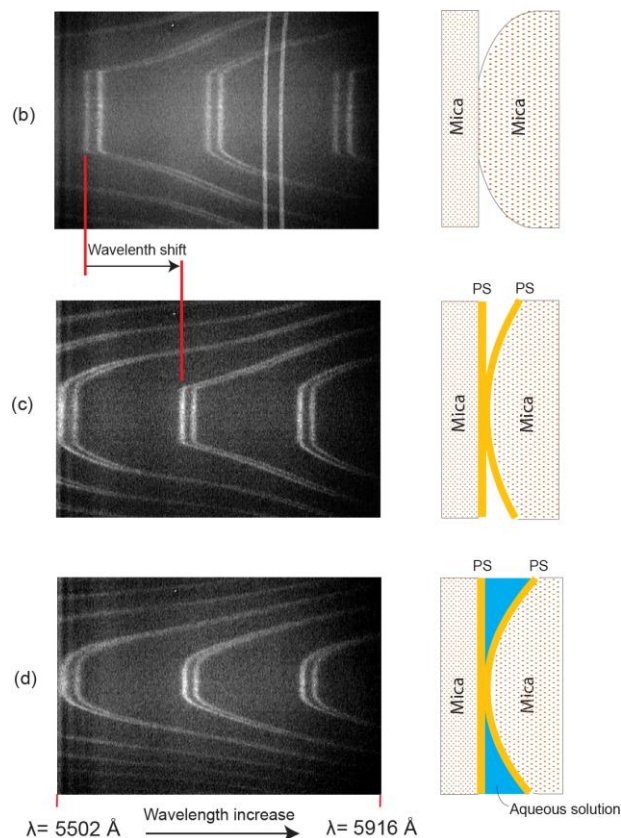


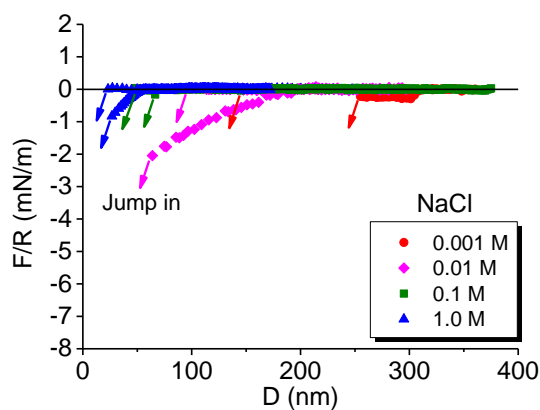
**Figure 2.1** (a) Schematic of SFA experiment setup for studying the surface interactions between two polystyrene (PS) films in various aqueous solutions. AFM image of spin-coated PS in the top right shows the surface topography of PS with root-mean-square (RMS) roughness of 0.3 nm. Multiple-beam interference fringes of equal chromatic order (FECO) for (b) two mica surfaces and (c) two PS surfaces in contact in air, and (d) the same pair of PS surfaces in aqueous solution. Note the shift in the wavelength of FECO and change in the shape (contact area) of the fringes. FECO can be used to measure the deformation and separation of surfaces and refractive index of the medium.

## 2.3 Results and discussion

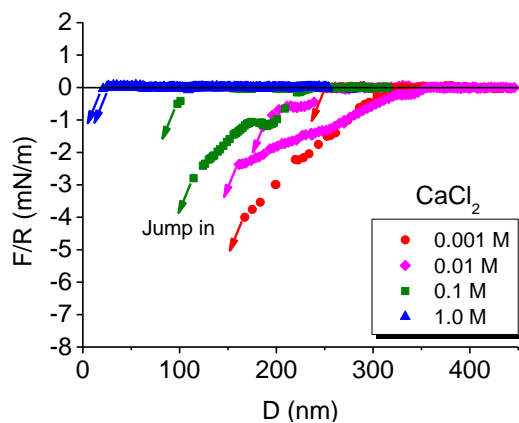
### 2.3.1 Effects of electrolyte type and concentration on PS-PS hydrophobic interaction

A typical AFM image of spin-coated PS surface is shown in Figure 2.1a with RMS roughness of 0.3 nm. The force-distance profiles between two PS

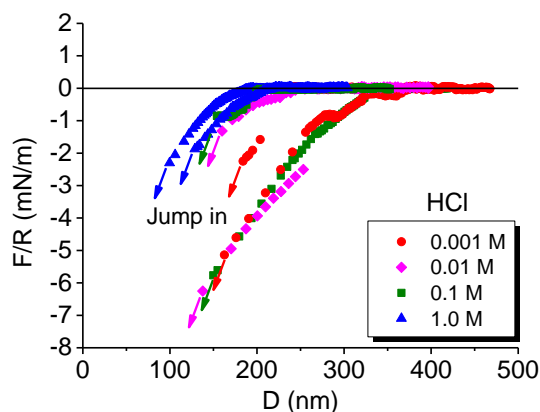
surfaces in NaCl,  $\text{CaCl}_2$ , HCl and  $\text{CH}_3\text{COOH}$  solutions of different concentrations ranging from 0.001 to 1.0 M measured by SFA are shown in Figure 2.2a, 2.2b, 2.2c and 2.2d respectively. For each solution condition, two representative force-distance curves from two independent experiments are shown in the figure.



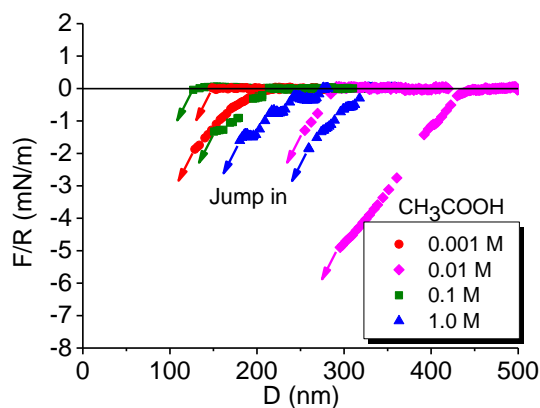
(a)



(b)



(c)



(d)

**Figure 2.2** Force-distance profiles measured during the approaching of two PS surfaces in four different electrolytes with concentrations ranging from 0.001 to 1.0 M: (a) NaCl, (b) CaCl<sub>2</sub>, (c) HCl, and (d) CH<sub>3</sub>COOH.

As shown in Figure 2.2a, the range of the hydrophobic force between PS surfaces decreases from  $\geq 150$  nm in 0.001 M to  $<25$  nm in 1.0 M NaCl solution. It should be noted that the “hydrophobic” force between the PS surfaces mentioned here and hereafter refers the long-range force measured by SFA. In 0.001 M and 0.01 M NaCl solution, the jump-in distance was observed to be 150–250 nm and 100–200 nm respectively with no significant difference. However, as the concentration increases to 0.1 M and then further to 1.0 M, the

jump-in distance decreases to 40–60 nm and 20–40 nm respectively. It was noted that the jump-in distance was not a constant value for a fixed electrolyte concentration. Especially for the lowest concentration 0.001 M, the jump-in distances varied by tens of nanometres from one measurement to another. The possible mechanism for such variation is discussed later in the paper.

As shown in Figure 2.2b, similar force-distance profiles and trend were observed in  $\text{CaCl}_2$  solution of different concentrations as that in NaCl solutions, e.g., the jump-in distances decreases from over 300 nm in 0.001 M to ~20 nm in 1.0 M  $\text{CaCl}_2$  solution. Interestingly, step-like force-distance profiles were observed during the approaching of the two PS surfaces at relatively lower  $\text{CaCl}_2$  concentrations (0.001–0.1 M). Such step-like force curves were similar to the ones previously reported by Parker et al. on the interactions between two silanated glass surfaces in aqueous solutions measured by SFA, which was suggested to be the indication of bridging of nanobubbles on hydrophobized glass.<sup>11</sup> The force-distance profiles measured in different concentrations of HCl and  $\text{CH}_3\text{COOH}$  solutions are shown in Figure 2.2c and 2.2d respectively. For HCl and  $\text{CH}_3\text{COOH}$  solutions, there is no considerable difference in the jump-in distances, which are all over 100 nm, as the concentration increases from 0.001 to 1.0 M. Steps and discontinuity in the force-distance profiles can be also observed for some of the experiments in Figure 2.2c and 2.2d. The above results show that NaCl and  $\text{CaCl}_2$  solutions decrease the range of the hydrophobic force between PS surfaces as the concentration increases from 0.001 to 1.0 M, while

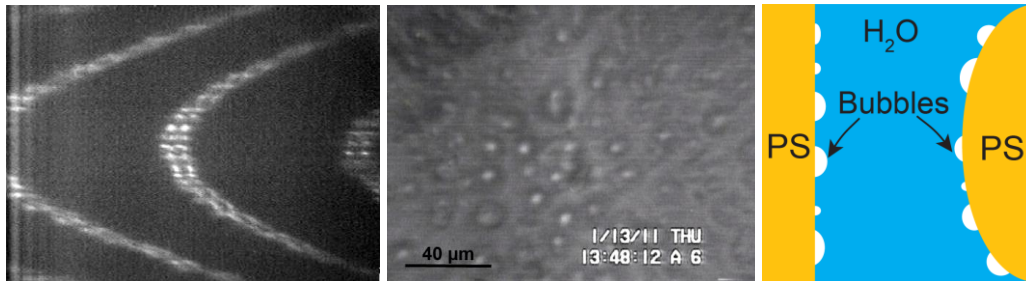
HCl and CH<sub>3</sub>COOH solutions do not significantly diminish the hydrophobic force within the same concentration range.

Two interesting features should be noted among Figures 2.2a to 2.2d. (1) Steps and discontinuity were observed in the measured force-distance profiles for almost all the electrolyte solutions examined, which have been previously observed by other researchers<sup>7,11,12,23,48</sup> and were attributed to the bridging of nanobubbles as an origin of the hydrophobic force. (2) For a specific solution concentration, it is common that the jump-in distance differs within a tens-of-nanometer range from one measurement to another. For example, the jump-in distance of PS surfaces in 1.0 M acetic acid solution varies from 180 nm to 260 nm in two individual measurements shown in Figure 2.2d. Meanwhile, the jump-in distances are more repeatable in 1.0 M concentration of the electrolyte solutions that diminish the hydrophobic force (i.e. NaCl and CaCl<sub>2</sub>). For instance, the jump-in distance varies within a 4-nm range for 1.0 M NaCl as opposed to a 100-nm range for 0.001 M NaCl solution. The observed difference in jump-in distances is due to the difference in the size of bubbles from one interacting position to another.<sup>23</sup>

To directly visualize the different stages of the hydrophobic interaction, a top-view optical microscope was used to observe the interacting PS surfaces simultaneously with measuring the forces. Figure 2.3 shows different stages of the hydrophobic interaction between two PS surfaces in 1.0 M acetic acid solution. It should be noted that different stages shown in Figure 2.3 were also observed for all other solutions that showed a large jump-in distance (>100 nm).



The three panels from left to right in Figure 2.3 are FECO fringes, corresponding top-view microscope images and illustration of interacting PS surfaces in each stage respectively. Microscopic and submicroscopic bubbles on PS surfaces were visible in the top-view microscope images which were also evident from the discontinuity on FECO fringes due to the refractive index difference between air and water, shown in Figure 2.3a and 2.3b. When the two PS surfaces were getting closer, the air bubbles in the vicinity of the interacting point started to coalesce (Figure 2.3b) as a result of reducing the total air-water interfacial energy. The PS surfaces then jumped into adhesive contact following the coalescence of the bubbles and an air meniscus was formed around the contact area as visualized in the FECO and microscopic image in Figure 2.3c. In the next stage, the air meniscus continued to coalesce with the small bubbles nearby and propagated quickly (less than 1 second as shown in the timer embedded) into the solution by outward fingering patterns (Figure 2.3d). The two PS surfaces were kept in contact for ~1 min and then started to separate. Before the surfaces jumped apart from adhesive contact, the air meniscus moved inward as fingering patterns (Figure 2.3e). Finally, the two PS surfaces jumped apart from contact and a few bubbles remained on the surfaces. As a result of strong adhesion force and large tensile stress at the rim of contact area of two PS films, the surfaces were normally observed to be damaged associated with detachment (Figure 2.3f).



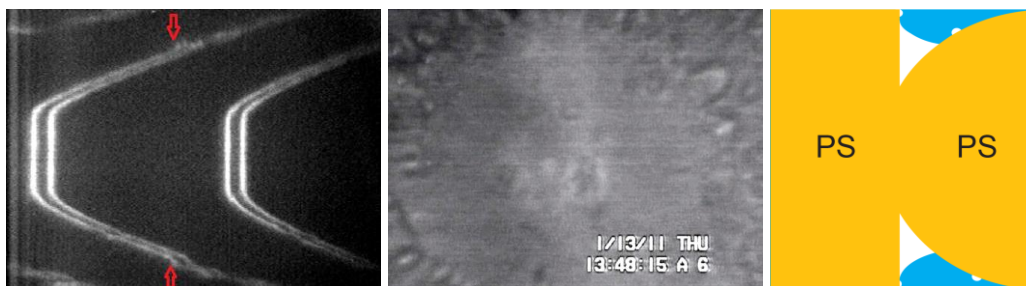
(a) Two PS surfaces were far from each other, and air bubbles were present on the PS surfaces.



(b) Air bubbles started to coalesce which led the two PS surfaces to get closer.



(c) Two PS surfaces jumped into adhesive contact, air meniscus was formed at the contact edge and propagated outward as fingering patterns (at air-water interface).



(d) Propagation of the air-water interface as outward fingering patterns.



(e) Associated with the detachment of PS surfaces, inward fingering patterns occurred at the air-water interface.



(f) After the surfaces were detached from contact, air bubbles and surface damage occurred.

**Figure 2.3** FECO fringes (left), top-view optical microscope image (middle) and illustration of the interaction between two PS surfaces (right) in 1.0 M  $\text{CH}_3\text{COOH}$  solution. (a) PS Surfaces were far from each other, and air bubbles were present on the PS surfaces as directly visualized by top-view optical microscope and evident by discontinuity in FECO fringes due to refractive index difference of air and water. (b) Air bubbles started to coalesce which led the two PS surfaces to get closer. (c) The PS surfaces jumped into adhesive contact and air meniscus was formed at the contact edge and propagated outward as fingering patterns (at air-water interface). The adhesive contact area was indicated by the flattened region of the FECO fringes. (d) Propagation of the air-water interface as outward fingering patterns, pointed out by the arrows in (c) and (d). (e) Associated with the detachment of PS surfaces, inward fingering patterns occurred at the air-water interface. (f) After the PS surfaces jumped apart from contact, air bubbles were normally left on the PS surfaces which were commonly damaged upon separation.

Upon jumping into adhesive contact, the two PS surface formed a finite contact area and the FECO fringes became flattened simultaneously which indicated the size of the contact region.<sup>40,49</sup> Meanwhile, the coalesced air bubbles formed a meniscus around the contact area. The high negative Laplace pressure

generated in the air meniscus due to the highly curved concave geometry at the rim led the air-water interface to propagate outward, similar to the coalescence case for two viscous polymer films reported recently.<sup>41,42,50</sup> In a confined channel (so-called Hele-Shaw flow cell), as a low viscosity fluid displaces a high viscosity fluid, fingers would occur at the fluid-fluid interface which is known as the Saffman-Taylor instability.<sup>51</sup> Similar fingering patterns have been observed previously during liquid-solid spreading and liquid-liquid coalescence of thin polymer films in SFA experiments.<sup>40-42</sup> In the Saffman-Taylor problem, the minimum wavelength (periodicity of the fingers)  $\lambda_c$  for a Hele-Shaw parallel plate geometry is given by Equation 2.1, where  $\gamma$  is the interfacial tension,  $b$  is the distance between the two parallel plates,  $\eta_1$  and  $\eta_2$  are the viscosities of the two fluids,  $V$  is the speed normal to the interface where fluid 2 pushes fluid 1:

$$\lambda_c = 2\pi\sqrt{\gamma b^2/12V(\eta_1 - \eta_2)} \quad (2.1)$$

In our case here, aqueous solution and air can be considered as fluids 1 and 2. The SFA geometry can be also approximated as a horizontal Hele-Shaw cell in which the width is much greater than the channel thickness (gap distance between two surfaces). Using the following values  $\gamma \approx 72$  mN/m for air-water interfacial tension,  $b \approx 5-20$  nm,  $V \approx 45$   $\mu\text{m/s}$  (estimated from the experimental measurement) and  $\eta_1 = 10^{-3}$  Pa·s for water, Equation 2.1 yields  $\lambda_c = 12-45$   $\mu\text{m}$ . The calculated  $\lambda_c$  values reasonably agree with the observed wavelength of the fingers shown in the top-view microscopic images of figure 2.3 (c)-(e). However as reported previously the lifetime of the fingers is roughly proportional to the viscosity of the displacing fluids<sup>40-42</sup> and for low viscosity fluids ( $\eta_{\text{water}} = 10^{-3}$

Pa•s,  $\eta_{\text{air}}=10^{-5}$  Pa•s) in current experiments, it was difficult to observe all the stages of finger growth by the conventional camera used here. More rigorous analysis of fingering patterns at the air-water interface needs the use of high-speed camera that can capture at least thousands of frames per second.

Figure 2.4 shows the FECO fringes and corresponding top-view microscope images of the two interacting PS surfaces in 0.001 and 1.0 M NaCl solutions before and after PS surfaces jumped into contact. Microscopic and sub-microscopic bubbles were observed on PS surfaces in 0.001 M NaCl which were evident by the microscope image and discontinuities in FECO fringes due to refractive index difference of air and water. However, no visible microscopic and sub-microscopic air bubbles could be detected on PS surface in 1.0 M NaCl although nanoscopic air bubbles might be still present. The corresponding jump-in distance measured was  $\sim 150$  nm and  $\sim 25$  nm in 0.001 M and 1.0 M NaCl respectively (also see Figure 2.2a). The jump-in distance is an indication of the height of the air bubbles. The microscopic images and the FECO fringes indicate that the air bubbles formed on the PS surfaces typically have a width of several micrometers or lower and a height of tens of nm, consistent with previous AFM measurement on other hydrophobic surfaces.<sup>52-56</sup> It should be noted that these bubbles on PS can coalesce not only across the films but also merge/coalesce on the same surface.<sup>56</sup> Figure 2.4 shows that more and bigger air bubbles were formed on PS surfaces in 0.001 M NaCl, compared to in 1.0 M solution, resulting in longer jump-in distance and larger air meniscus as consistent with Figure 2.2a where the range of the hydrophobic force decreased with NaCl

concentration increasing from 0.001 to 1.0 M. Similar trend was also observed for  $\text{CaCl}_2$  solution when the concentration increased from 0.001 to 1.0 M. In contrast, microscopic and sub-microscopic air bubbles were still present on PS surface even in high concentration 1.0 M of HCl and  $\text{CH}_3\text{COOH}$  solutions as shown in Figure 2.3.

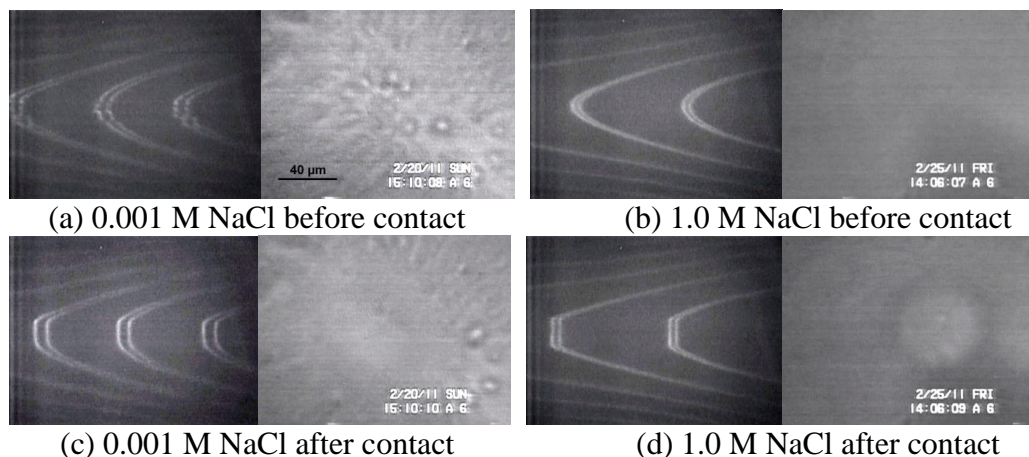


**Figure 2.4** FECO fringes and top-view optical microscope images of the interaction of two PS surfaces in (a)&(c) 0.001 M and (b)&(d) 1.0 M NaCl solution before and after contact respectively.

The range of the hydrophobic force was greatly reduced for NaCl and  $\text{CaCl}_2$  from 50–100 nm in 0.1 M to ~25 nm in 1.0 M concentration (see Figure 2.2a,b). It has also been reported that the concentration at which bubble coalescence inhibition takes place is more than 0.1 M for the electrolytes that inhibit bubble coalescence.<sup>22,57,58</sup> The reported results<sup>22,57,58</sup> are very similar to our observation of the effect of electrolyte concentration on the range of the hydrophobic force measured. However, the hydrophobic force was still present in 1.0 M of NaCl and  $\text{CaCl}_2$  and discontinuity in FECO fringes around contact area which is indicative of presence of air meniscus, was still observed at 1.0 M

concentration for these electrolytes. Therefore it is likely that while NaCl and  $\text{CaCl}_2$  suppress bubble formation in 1.0 M concentration, but still few smaller bubbles can form on the PS surface. The effect of NaCl and  $\text{CaCl}_2$  could be on the size of the bubbles that are formed on the PS surface. NaCl and  $\text{CaCl}_2$  at high concentrations ( $>0.1$  M) reduce bubble adsorption on the hydrophobic surface and thus reduce bubble size from few micrometers (as observed through top view microscope) to few nanometers which leads to decrease in the range of the hydrophobic force (i.e. jump-in distance).

### **2.3.2 Effect of degassing**

The interaction between two PS surfaces in degassed NaCl and  $\text{CH}_3\text{COOH}$  solutions of 0.001–1.0 M were also measured by SFA, and the force-distance profiles obtained are shown in Figure 2.5. Upon degassing the solutions, the jump-in distance reduces to 10–20 nm in both NaCl and  $\text{CH}_3\text{COOH}$  solutions, as opposed to the much longer range forces shown in Figure 2.2a and 2.2d. Thus, it is evident that the very long-range force (20 to  $>300$  nm) measured in Figure 2.2 are due to the bridging of bubbles on the hydrophobic PS surfaces.

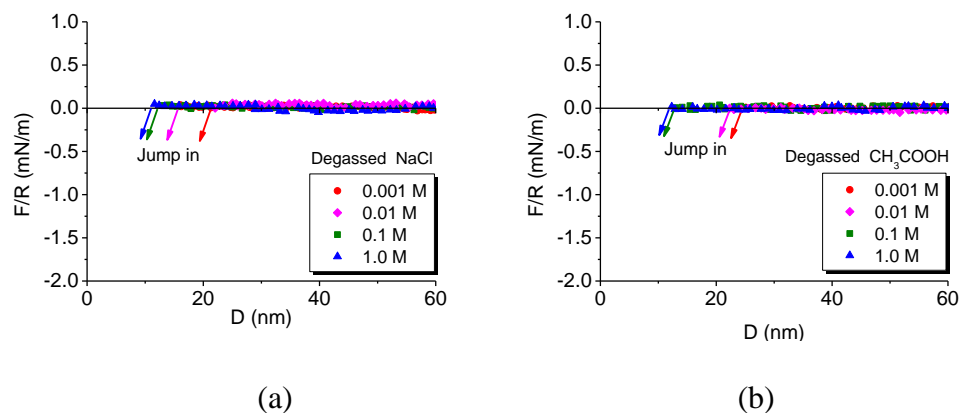


**Figure 2.5** Force-distance profiles measured between two PS surfaces interacting in different concentrations of degassed (a) NaCl and (b) CH<sub>3</sub>COOH solutions.

Different stages of the hydrophobic interaction between PS surfaces in degassed 0.001 M NaCl is shown in Figure 2.6. Initially no bubble could be detected on the PS surfaces (Figure 2.6a). As the surfaces came closer to  $D \leq 20$  nm, discontinuity on FECO was observed (Figure 2.6b) as an indication of appearance of cavities, and then PS surfaces jumped into contact instantaneously (Figure 2.6c). After the jump into contact, formation and propagation of small cavity meniscus outside of the contact regime, similar as shown in Figure 2.3, was normally observed.



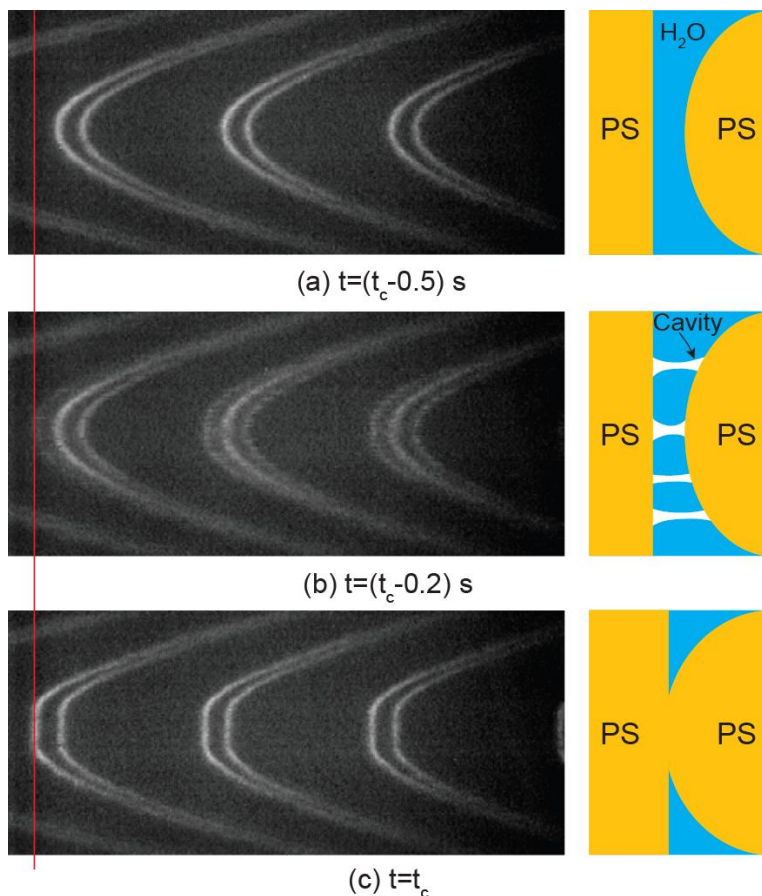


**Figure 2.6** FECO (left) and illustration (right) of two interacting PS surfaces in degassed 0.001 M NaCl: (a) 0.5 s before jump into contact, (b) 0.2 s before jump into contact, (c) at the instant of contact ( $t=t_c$ ). The discontinuity on FECO fringes observed before the PS surfaces jumped in contact could be due to: (1) spontaneous cavitation of water between hydrophobic surfaces, and/or (2) bridging of nanoscopic bubbles.

There could be two possible mechanisms for the observed discontinuity on FECO fringes before the PS surfaces jumped into contact: (1) spontaneous cavitation of water between hydrophobic surfaces, and (2) bridging of nanoscopic bubbles. In previous experimental studies, cavity formation was reported only after hydrophobic surfaces jumped into contact<sup>1</sup> or during separation of the surfaces,<sup>8,59</sup> as also observed in this study (see Figure 2.3 and SI Figure 1 in Supporting Information). Theoretical and molecular simulation

studies predict the formation of vapour cavities when intersurface distance is below a critical value  $D_c$ .<sup>60-63</sup> According to the coarse-grained description, for two parallel flat hydrophobic surfaces,  $D_c$  can be approximately given by the Kelvin equation

$$D_c \approx 2(\gamma_{sw} - \gamma_{sv}) / \rho \Delta\mu , \quad (2.2)$$

where  $\rho$  is the molecular number density of bulk water (average number of molecules per unit volume),  $\Delta\mu$  is the chemical potential different between the bulk water and water/vapour coexistence state,  $\gamma_{sw}$  and  $\gamma_{sv}$  are the interfacial energies of solid hydrophobic surface-water and solid hydrophobic surface-vapour respectively.<sup>60-63</sup> For very hydrophobic surfaces and under ambient conditions (at room temperature and the bulk pressure of 1 atm),  $\rho\Delta\mu \sim 1$  atm, and the critical distance  $D_c$  below which the vapour phase is more favoured is of the order of 100 nm. Based on the above analysis, the discontinuity on the FECO fringes right before the polystyrene surfaces jumped into contact in degassed solution could be the direct experimental evidence of appearance of such cavities induced by “true” hydrophobic effect, which is the first observation of its kind to attempt to capture the cavitation between two interacting closed (but not contacted) hydrophobic surfaces.

However, it should be noted that electrolyte solution might not be “completely” degassed in this study as the vacuum pressure was 50 mmHg which corresponds to partial degassing, and nanoscopic air bubbles could be still formed on PS surface. When the intersurface distance was in the order of bubble heights, bridging and coalescence of these nanoscopic bubbles could initiate,

which might also lead to the discontinuity on the FECO fringes observed (Figure 2.6b).

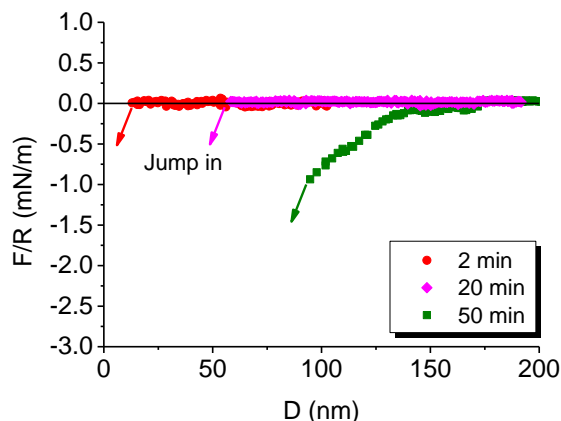


**Figure 2.7** Force-distance profiles between two PS surfaces in 0.1 M degassed  $\text{CH}_3\text{COOH}$  after re-exposing to air for different times.

In order to further investigate the effect of dissolved gases, the interaction forces between PS surfaces were measured in 0.1 M degassed  $\text{CH}_3\text{COOH}$  solution re-exposed to air for different times (2, 30 and 50 min) allowing air to re-dissolve in the aqueous solutions, as shown in Figure 2.7. Interestingly, the range of the hydrophobic force increases with the exposure time, and after 50 min the force-distance profiles finally recovered to the original ones obtained in solutions saturated with air shown in Figure 2.2d. The above results indicate that air was gradually dissolved back into the aqueous solution and thus air bubbles preferentially re-adsorbed or formed on the hydrophobic PS surfaces with time. The increased jump-in distances shown in Figure 2.7, from ~10 nm for 2 min, to ~50 nm for 20 min, and finally to >100 nm for 50 min, indicate that the size of the bubbles on PS surfaces grew substantially with time. The time scale observed

here is comparable to the adsorption kinetics of CO<sub>2</sub> on a hydrophobic surface reported by Yang et. al. recently.<sup>64</sup>

### 2.3.3 Formation of bubbles on hydrophobic polymer surfaces

It is evident from the above results and discussion that the long-ranged hydrophobic forces measured between two PS surfaces in various electrolyte solutions are mainly due to the bridging of bubbles on the polymer surfaces. There has been some debate in the literature whether such mechanism, e.g., bridging of bubbles or cavities, could be the origin of the long-range hydrophobic force.<sup>11,65-69</sup> One main argument for rejecting such mechanism was about the formation and stability of bubbles on hydrophobic surfaces, which was considered to be energy unfavourable and unstable due to large Laplace pressure.<sup>23,66</sup> Several experimental studies using tapping-mode AFM imaging confirmed the presence of bubbles on various hydrophobic surfaces.<sup>7,52,53,56,70,71</sup> However, the morphology and curvature of the bubbles were estimated by AFM to be in a form that only leads to moderate pressure difference, and thus the bubbles could be stable on hydrophobic substrates for at least several hours.<sup>52-55</sup> Adsorption of sub-microscopic bubbles from bulk water to hydrophobic surface<sup>11,64,65</sup> and supersaturation of the solution with gas<sup>52,53</sup> are among the common mechanisms proposed previously for bubble formation. Other methods including solvent exchange<sup>52,53,72,73</sup> or temperature change<sup>73-75</sup> techniques have also been applied to produce bubbles on a hydrophobic surface, which should not be the causes of bubble formation on PS in this study.

Our results clearly indicate that different ions have different impact on the hydrophobic forces measured between the PS surfaces, which provide an insight into the mechanism of bubble formation and their subsequent stability on hydrophobic polymer surfaces, as discussed below. However, the advancing and receding contact angles of all the electrolyte solutions of 0.001 to 1.0 M on PS surface were measured to be  $90\pm 1^\circ$  and  $82\pm 1^\circ$  respectively. The fact that different ions have their own specific effects on many colloidal and biological phenomena is normally referred to as ion specificity. The question of ion specificity was first considered by Hofmeister in 1888,<sup>76</sup> who studied the solubility of proteins in different electrolyte solutions and ranked ions based on their ability to salt out a given protein from aqueous solution (note “salting out” refers that solubility decreases in a salt solution compared with in pure water, and vice versa known as “salting in”<sup>77</sup>). Despite its long history, the role of ion specificity in colloid and surface science has only received considerable attention since 1990s.<sup>78,79</sup> Previous studies on electrolyte dependence of bubble coalescence,<sup>22,58,80</sup> association of small hydrophobic solutes in water,<sup>81,82</sup> and optical (laser-induced) cavitation near hydrophobic surfaces<sup>83</sup> are all examples of ion specificity and its impact on the hydrophobic interactions. Therefore, it is believed that the observed ion specificity on the formation and stability of bubbles on PS surfaces and the resulted hydrophobic forces in the present study are closely related to the impact of specific ions on the surface tension of aqueous solution, air solubility in water, and hydrogen bond (H-bond) network of water molecules.

The change in surface tension of water upon addition of electrolytes is related to the adsorption/depletion of ions at gas/water interface according to the Gibbs adsorption isotherm

$$\Gamma_{\text{ion}}^{\text{H}_2\text{O}} = -\frac{1}{RT} \left( \frac{\partial \gamma}{\partial \ln(a_{\text{ion}})} \right)_T, \quad (2.3)$$

where  $\Gamma_{\text{ion}}^{\text{H}_2\text{O}}$ , referred to as the relative surface excess, is the excess amount of ion adsorbed at the particular surface where the excess amount of water is zero<sup>78</sup>,  $R$  is the gas constant,  $T$  is temperature and  $a_{\text{ion}}$  is the electrolyte activity. Equation 2.3 shows that for electrolytes that increase surface tension (e.g., NaCl and  $\text{CaCl}_2$ ),  $\Gamma_{\text{ion}}^{\text{H}_2\text{O}} < 0$ , therefore ions are depleted from the interface, while for the electrolytes that decrease surface tension (e.g., HCl and  $\text{CH}_3\text{COOH}$ ),  $\Gamma_{\text{ion}}^{\text{H}_2\text{O}} > 0$ , ions are adsorbed at the air-water interface. Recent molecular simulations and spectroscopic studies of electrolyte solutions showed ion partitioning at the air-water interface,<sup>78</sup> and the ions used in this study are ordered as  $\text{H}^+ > \text{CH}_3\text{COO}^- > \text{Cl}^- > \text{Na}^+$  based on their affinity to the air-water interface (note, no data was reported for  $\text{Ca}^{2+}$ ).<sup>57,78,84</sup> It should be noted that  $\text{H}^+$  can be readily solvated by water and form hydronium ion ( $\text{H}_3\text{O}^+$ ) in an aqueous solution. Thus  $\text{H}_3\text{O}^+$  has the highest affinity to the interface while  $\text{Na}^+$  has the lowest.

The ion specificity on the solubility of oxygen and nitrogen (where available) in water, change of water surface tension ( $\Delta\gamma = \gamma - \gamma_w$ , where  $\gamma$ ,  $\gamma_w$  are the surface tensions of electrolyte solution and water respectively), nitrogen bubble coalescence and the hydrophobic forces between PS surfaces (in 1 M electrolyte solutions) are summarized in Table 2.1. Note, oxygen and nitrogen

solubility are given as the Bunsen coefficient ( $\alpha$ ) which is defined as the volume of gas, reduced to 273.15 K and 1 atm, which is absorbed by unit volume of solvent at the temperature of measurement, when the partial pressure of the gas is 1 atm.<sup>85</sup> From Table 2.1, it is clear that oxygen solubility is more than nitrogen. Unfortunately the nitrogen solubility in HCl, CH<sub>3</sub>COOH and CaCl<sub>2</sub> solutions around the room temperature and pressure were not found, but it is expected that the change of nitrogen solubility follows a similar trend as oxygen. Therefore, we used the trend in the change of oxygen solubility at 37°C to approximate the trend for air solubility at room temperature.<sup>85</sup>

**Table 2.1** Effect of electrolytes on air solubility and air-water interfacial properties

Solution	Oxygen solubility at 37°C ( $\alpha \times 10^4$ ) <sup>a</sup>	Nitrogen solubility at 37°C ( $\alpha \times 10^4$ ) <sup>a</sup>	Oxygen solubility at 25°C ( $\alpha \times 10^4$ )	Nitrogen solubility at 25°C ( $\alpha \times 10^4$ )	$\gamma - \gamma_w$ (mN/m)	Bubble coale- scence <sup>b</sup>	Hydro- phobic force <sup>c</sup>
Water	238	128	286	144	0	×	×
NaCl	177	96	205	107	2.08	✓	✓
CaCl <sub>2</sub>	143	N/A	179	N/A	4.02	✓	✓
CH <sub>3</sub> COOH	440 <sup>d</sup>	N/A	N/A	N/A	-38	✓	×
HCl	225	N/A	266	N/A	-0.27	×	×

All data presented here are for electrolyte solutions of 1 M concentration.

<sup>a</sup>Interpolation and extrapolation was done to obtain values for 1.0 M concentration. Data compiled from Refs<sup>85-88</sup>.

<sup>b</sup>Bubble coalescence results are adapted from Craig et al.<sup>22, 58</sup>

<sup>c</sup>Hydrophobic force between PS surfaces as observed in this study.

<sup>d</sup>The solubility value given here is at 40°C.

✓ Suppressed.

×

As shown in Table 2.1, 1 M NaCl and CaCl<sub>2</sub> salt out air by -26% and -40% respectively while CH<sub>3</sub>COOH salts in by +85%, and HCl has little effect (-5%) on air solubility. The decreased air solubility due to the presence of 1 M NaCl and CaCl<sub>2</sub> is consistent with the less bubbles observed on PS surfaces and

much shorter ranged hydrophobic forces (see Figures 2.2a and 2.4). Our results (except for  $\text{CH}_3\text{COOH}$ ) are also consistent with the bubble coalescence experiments by Craig et al.<sup>22,58</sup> that some ion pairs (i.e.,  $\text{NaCl}$ ,  $\text{CaCl}_2$ ) inhibit bubble coalescence when present at high concentrations (typically above 0.1 M) whereas others (i.e.,  $\text{HCl}$ ) show no effect. Craig et al. also showed that  $\text{CH}_3\text{COOH}$  inhibits bubble coalescence, while our results showed  $\text{CH}_3\text{COOH}$  has no significant effect on the formation of bubbles on PS surface and the consequent hydrophobic force even at 1 M (see Figure 2.2d). The above discrepancy could be mainly due to the difference of the two kinds of experiments as follows. As shown in Table 2.1, 1 M  $\text{CH}_3\text{COOH}$  significantly reduces the surface tension of water ( $-38 \text{ mN/m}$ ) and increases oxygen solubility by 85%. It has been reported that both  $\text{H}_3\text{O}^+$  and  $\text{CH}_3\text{COO}^-$  show high affinity to air-water interface.<sup>57,78,84</sup> Therefore, it is expected that  $\text{CH}_3\text{COOH}$  does not suppress bubble formation on PS surfaces as observed. Nevertheless, there are some fundamental differences between our experiment and the bubble coalescence experiment by Craig et al.,<sup>22,58</sup> which could lead to the observed discrepancy: supersaturation condition in the process of generation of bubbles and hydrodynamic effects which played a critical role in the coalescence experiment<sup>89-91</sup> while such effects were totally ruled out in the present study.

The effect of electrolytes on bubble formation on PS surfaces and associated surface interactions can be also understood at the molecular level as follows.  $\text{H}_3\text{O}^+$  is able to donate three hydrogen bonds but is a very bad hydrogen bond acceptor due to the small partial charge on oxygen atom. Therefore  $\text{H}_3\text{O}^+$



tends to point toward gas phase from oxygen side to minimize disruption of hydrogen bonding network of water molecules.<sup>78</sup> Similarly  $\text{CH}_3\text{COO}^-$  has a relatively large hydrophobic site and one hydrogen bond acceptor. Thus  $\text{H}_3\text{O}^+$  and  $\text{CH}_3\text{COO}^-$  tend to adsorb on water-bubble interface and decrease surface tension and stabilize air bubbles on PS surfaces. On the other hand,  $\text{Na}^+$  and  $\text{Ca}^{2+}$  ions, which have less tendency toward the air-water interface, would increase the surface tension thus suppress the bubble formation and stability on PS surfaces.

The mechanism for air bubble formation on a hydrophobic polymer surface is considered to be mainly entropically driven. It has been reported that water molecules form “frozen patches”<sup>92</sup> or “clathrate cages”<sup>2,93</sup> around hydrophobic solutes due to the high propensity of water molecules for preserving their H-bond network. This reorientation of water molecules around hydrophobic solutes is entropically very unfavourable. In the presence of a hydrophobic surface, these water clathrate cages would “break”, therefore hydrophobic solutes (i.e. dissolved air) adsorb onto the hydrophobic surface to allow water molecules fully coordinated through H-bond network which is entropically more favourable. In the presence of ions, H-bond network of water molecules can be altered depending on the type of ions. Generally, high-charge-density ions (i.e.,  $\text{Na}^+$ ,  $\text{Ca}^{2+}$ ) affect orientation and H-bond network of water molecules more than low-charge-density ions (i.e.  $\text{CH}_3\text{COO}^-$ ,  $\text{Cl}^-$ ,  $\text{H}_3\text{O}^+$ ).<sup>2</sup> Recent advances that use ultrafast spectroscopy and polarization-selective 2D-IR spectroscopy<sup>94-96</sup> can help provide important insight into the role of specific ions on water structure.

Therefore the adsorption of air onto PS surface is more entropically favourable in HCl and CH<sub>3</sub>COOH solutions than in NaCl and CaCl<sub>2</sub>.

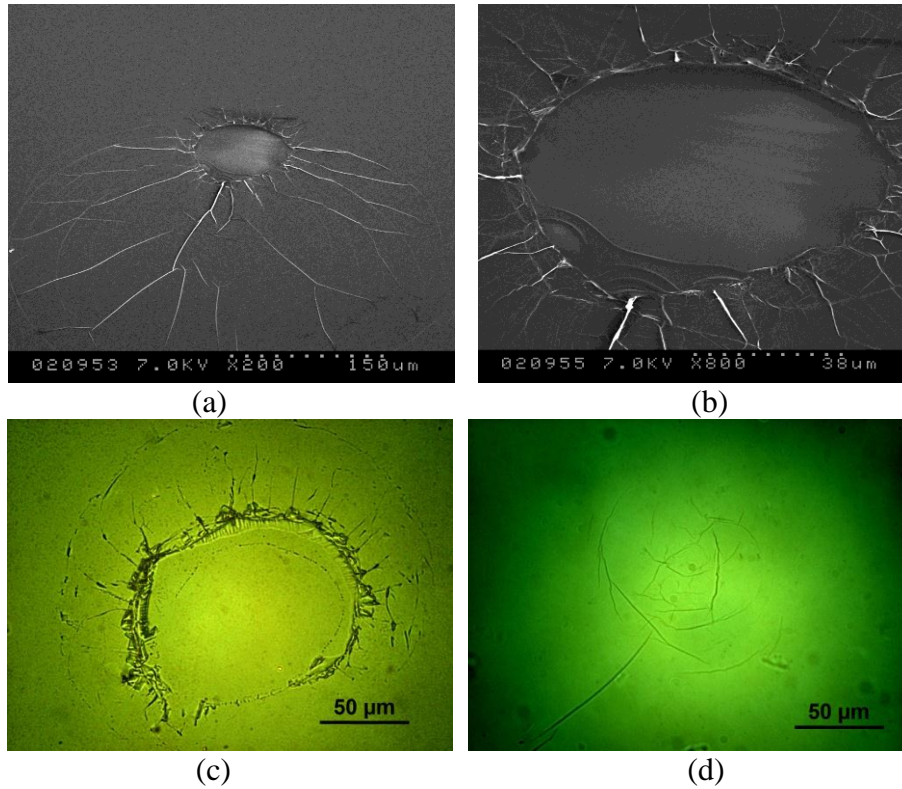
It should be noted that attachment of sub-microscopic bubbles present in the bulk electrolyte solution onto hydrophobic polymer surfaces is also directly related to the surface interaction between bubbles and hydrophobic polymer, which has not been discussed above. Very recently, using atomic force microscope and specially manufactured cantilever, D.Y.C. Chan, R.R. Dagastine and their colleagues directly measured the interaction forces between two microscopic bubbles (50-200  $\mu\text{m}$ ) or a bubble against a solid surface in various aqueous solution, which were found to depend on the electrolyte concentrations and pH.<sup>97,98</sup> For instance, at pH=7, repulsive force was detected between two argon bubbles at an approach speed of 0.2 mm/s, which turned into attractive force (“jump in” or coalescence occurred) at 0.1 M NaCl and 0.05 M MgSO<sub>4</sub>. Such transition was suggested to be due to the ion-pair complex adsorption at the bubble/solution interface which led to the change of interfacial hydrodynamic boundary condition.<sup>89,91,97,98</sup> The impact of salt concentrations on the surface forces between polystyrene and the formation of bubbles on polystyrene in this study agree with the above AFM measurement and analysis.

#### **2.3.4 Fracture of polymer surfaces due to the hydrophobic interactions**

The adhesion between the two PS surfaces in various electrolyte solutions was measured by separating the two surfaces in adhesive contact. The measured adhesion was  $F_{\text{ad}}/R=400\pm50$  mN/m. Based on the Johnson-Kendall-Roberts (JKR) contact theory as shown in Equation 2.4:<sup>99</sup>

$$F_{ad} = -1.5\pi RW = -3\pi R\gamma \quad (2.4)$$

where  $F_{ad}$  is the adhesion force,  $R$  is the radius of the curvature of interacting surfaces,  $W$  is the adhesion energy and  $\gamma$  is the interfacial energy ( $W=2\gamma$  here), the interfacial energy is estimated to be  $\gamma=42\pm5$  mJ/m<sup>2</sup>, which is interestingly very close to the values measured in air 35–43 mJ/m<sup>2</sup>.<sup>40,100</sup> The PS surfaces were normally observed to be damaged associated with the separation. Figure 2.8 shows the typical SEM and optical microscope images of different patterns of damaged PS surfaces after separation from adhesive contact. The damaged region is typically much bigger than the contact area with the cracks mostly extending radially outwards in the PS films although damages were also observed within the contact area.



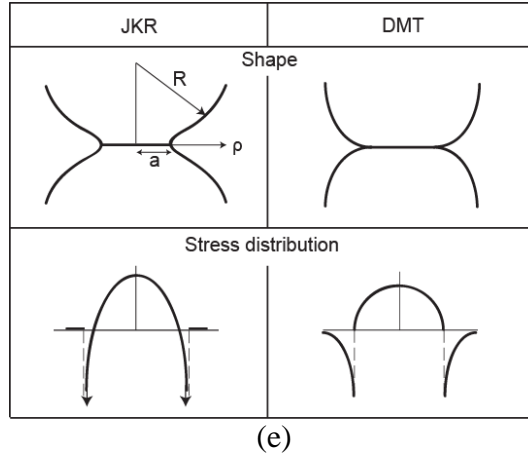


**Figure 2.8** (a) and (b) SEM images, and (c) and (d) optical microscope images of different topographic patterns of damaged PS surfaces after separation from adhesive contact; (e) illustration of the contact shape and stress distribution for two surfaces in contact predicted by JKR and DMT theories.

As clearly shown in Figure 2.8, cracks initiate and propagate from the boundary of the contact area which occurs as a result of the large tensile stress at the rim. Such observation can be related to the stress distribution around the contact region predicted by the classical contact mechanics theories. According to the JKR theory, stress distribution within the contact area is given by<sup>101</sup>

$$\sigma(x) = \frac{3Ka}{2\pi R} \sqrt{1-x^2} - \sqrt{\frac{3\gamma K}{\pi a(1-x^2)}} \quad (2.5)$$

where  $K = \frac{2}{3} \left( E / (1-\nu^2) \right)$  in which  $E$  is Young's modulus,  $\nu$  is Poisson's ratio of the contacting materials,  $a$  is the radius of contact area and  $x = \rho / a$  (see Figure 2.8e). According to Equation 2.5, at the rim of contact area ( $x=1$ ), there is an infinite tensile stress. The Derjaguin-Muller-Toporov (DMT) theory<sup>102,103</sup> resolves the unphysical infinite tensile stress at the boundary of contact area and still predicts a large tensile stress at the rim but with a stress discontinuity. The

stress distribution and contact geometry predicted by JKR and DMT theories are schematically shown in Figure 2.8e. The more recent unified Maugis model removes the singularity of the JKR theory, the stress discontinuity of the DMT theory, and also provides a transition from the JKR to the DMT models by introducing a dimensionless parameter so-called “Tabor Number” similar to the parameter introduced by Muller et al. previously.<sup>104,105</sup> The JKR theory is usually applicable to soft materials with large surface energies and radii (Tabor Number  $\gg 1$ ), and the DMT theory applies to small, rigid spheres (or asperities) with low surface energies (Tabor Number  $\ll 1$ ).<sup>105</sup> The polystyrene thin films in this study are soft polymer with large surface energies, and contact surfaces have large radii, therefore the JKR theory would be more applicable, leading to a large tensile stress at the contact edge which induced the fracture process.

It has been observed that fingering instability could be associated with the failure of glassy polymers,<sup>49,106</sup> and the critical fracture wavelength is given by

$$\lambda_c \propto b \sqrt{\frac{G_c}{\sigma b}} \approx 2\pi b \sqrt{\frac{\gamma}{12Eb}}, \quad (2.6)$$

where  $\sigma$  is the yield stress,  $G_c$  is the critical energy release rate and  $E$  is the elastic modulus of the polymer films. By inserting the typical values from our experiment:  $b \approx 100$  nm,  $\gamma \approx 42$  mJ/m<sup>2</sup>,  $E \approx 3$  GPa, the predicted minimum wavelength of fracture fingers would be  $\lambda_c \approx 2$  nm which could be a rough estimation of the initial crack tip size before crack propagation. This rough estimation agrees with the experimental measurement by A.M. Donald and E.J.

Kramer on the crack width around the crack tip in polystyrene thin films by using transmission electron microscopy in the range of 5-25 nm.<sup>106</sup>

It should be noted that the surface damage observed in Figure 2.8 is quite different from the surface damage observed previously for polymer-polymer adhesion in air, which normally occurs inside the contact area and is due to the interdigitation of polymer chain ends across the contacting interface especially for polymers with low molecular weight.<sup>38,40,49,100,107</sup> We have also noticed that no surface damage occurred for the contact mechanics tests for polystyrene surfaces with MW=1,000,000 in air due to the large molecular weight and few free chain ends on the surface available for interdigitation. The above results indicate that the surface damage associated with the separation of two hydrophobic polymer surfaces in aqueous solutions must be related to the complex interactions among hydrophobic surfaces, electrolyte solutions and the possible bubbles/cavities present. Such fracture should not be neglected which may cause damage in many engineering and biomedical processes where the contact and separation of hydrophobic surfaces and thin films are involved. A more rigorous theoretical analysis on the fracture mechanism will be done in future study.

### **2.3.5 Three-regime hydrophobic interaction model**

The SFA results in this study showed that degassing could affect the interaction between two hydrophobic polystyrene surfaces by reducing the jump-in distance from >50 nm in solutions with dissolved air to about 10–20 nm (see Figures 2.2 and 2.5). As van der Waals forces and electric double layer forces

generally exist between interacting surfaces in aqueous solutions, the Derjaguin-Landau-Verwey-Overbeek (DLVO) theory was applied to compare the ranges of DLVO forces and the hydrophobic forces between PS surfaces measured here, as shown in the insert in Figure 2.9. For two PS surfaces in crossed-cylinder configuration in an aqueous solution, the DLVO interaction forces include an electrostatic double layer component and van der Waals interaction component, given by Equation 2.7, where  $1/\kappa$  is the Debye length,  $Z = 9.22 \times 10^{-11} \tanh^2(\Psi_1/103)$  at room temperature in which  $\Psi_1$  is surface potential,<sup>2</sup> and  $A_{121}$  is the Hamaker constant in which 1 and 2 refer to PS and aqueous solution respectively.

$$\frac{F(D)}{R} = \kappa Z e^{-\kappa D} - \frac{A_{121}}{6D^2} \quad (2.7)$$

The Hamaker constant is given by<sup>2</sup>

$$A_{121} \approx \frac{3}{4} kT \left( \frac{\varepsilon_1 - \varepsilon_2}{\varepsilon_1 + \varepsilon_2} \right)^2 + \frac{3h\nu_e}{16\sqrt{2}} \frac{(n_1^2 - n_2^2)^2}{(n_1^2 + n_2^2)^{3/2}}, \quad (2.8a)$$

or

$$A_{121} \approx \left( \sqrt{A_1} - \sqrt{A_2} \right)^2, \quad (2.8b)$$

where  $\nu_e$  is the absorption frequency,  $\varepsilon$  is the dielectric constant,  $n$  is the refractive index, and  $A$  is the Hamaker constant in vacuum. Using the values  $\nu_e = 3 \times 10^{15} \text{ s}^{-1}$ ,  $\varepsilon_1 = 2.55$ ,  $\varepsilon_2 = 78.4$ ,  $n_1 = 1.58$ ,  $n_2 = 1.33$ ,  $A_1 \approx 9.1 \times 10^{-20} \text{ J}$ ,  $A_2 \approx 3.7 \times 10^{-20} \text{ J}$ ,<sup>2</sup> Equations 2.8a and 2.8b give  $A_{121} \approx 1.85 \times 10^{-20} \text{ J}$  and  $A_{121} \approx 1.19 \times 10^{-20} \text{ J}$  respectively. For 1:1 electrolytes in 0.1 M solution, the Debye length  $1/\kappa = 0.96 \text{ nm}$ ;<sup>2</sup> assuming  $\Psi_1 \approx -45 \text{ mV}$  for PS surfaces,<sup>108</sup> Equation 2.7 gives the calculated

DLVO force-distance profile shown in Figure 2.9 (insert), which shows the attractive DLVO force between two polystyrene surfaces becomes important only at separation of  $D < 1$  nm that is much shorter ranged than the attractive forces measured by the SFA in this study.

When the PS surfaces were partially covered by submicroscopic bubbles, the above DLVO force  $F(D)$  could be modified. Three distinct interactions can occur and dominate the surface interaction: (i) bubble-water-bubble (3-2-3), (ii) PS-water-PS (1-2-1), and (iii) PS-water-bubble (1-2-3), as shown in Figure 2.9. As the other interactions such as PS-bubble-water-PS (1-3-2-1) and PS-bubble-water-bubble-PS (1-3-2-3-1) are much weaker compared to above three interactions, the total interaction force  $F(D)$  can be approximated as:

$$F(D) \approx F_{121}^{vdw} + F_{123}^{vdw} + F_{323}^{vdw} + F_{121}^{dl} + F_{123}^{dl} + F_{323}^{dl} \quad (2.9)$$

where 1, 2, and 3 refer to PS, aqueous solution and bubble, respectively.<sup>30,109-112</sup>

$\alpha = S_{bubble} / S_{total}$  is defined as the ratio of bubble-covered polymer surface area  $S_{bubble}$  to the total area of the polymer surface  $S_{total}$ . Following a similar approach developed by S. Usui, E. Barouch, J. Ralston, et al.,<sup>30,109-112</sup> the modified van der Waals and double layer forces by including the impact of the adsorbed bubble layers can be given by Equations 2.10 and 2.11.

$$F_{121}^{vdw} = -\frac{(1-\alpha)^2 A_{121} R}{6D^2} \quad (2.10a)$$

$$F_{123}^{vdw} = -\frac{\alpha(1-\alpha) A_{123} R}{6(D-H)^2} \quad (2.10b)$$



$$F_{323}^{vdw} = -\frac{\alpha^2 A_{323} R}{6(D-2H)^2} \quad (2.10c)$$

$$F_{121}^{dl} = 4\pi(1-\alpha)^2 R \varepsilon_0 \varepsilon \kappa \Psi_1^2 e^{-\kappa D} \quad (2.11a)$$

$$F_{123}^{dl} = 4\pi\alpha(1-\alpha) R \varepsilon_0 \varepsilon \kappa \Psi_1 \Psi_3 e^{-\kappa(D-H)} \quad (2.11b)$$

$$F_{323}^{dl} = 4\pi\alpha^2 R \varepsilon_0 \varepsilon \kappa \Psi_3^2 e^{-\kappa(D-2H)} \quad (2.11c)$$

It should be noted that the above analysis assumes that  $G \gg H$  and  $L \gg H$ , where  $H$  is the average height and  $L$  is the average width of bubbles on PS, and  $G$  is the average distance between the bubbles on PS, which is a very reasonable assumption as  $G$  and  $L$  are on the order of micrometers and  $H$  is on the order of nanometers or tens of nanometer (see Figures 2.3 and 2.9). It should also be noted that Equations 2.10a, 2.10c, 2.11a, 2.11c consider the limit case of two symmetric interacting surfaces (bubbles facing opposing bubbles), while Equations 2.10b and 2.11b considered the limit case in which bubbles are all facing opposing PS surface. For the symmetric limit case, the total interaction forces is given by

$$F(D) \approx -\frac{(1-\alpha)^2 A_{121} R}{6D^2} - \frac{\alpha^2 A_{323} R}{6(D-2H)^2} + 4\pi(1-\alpha)^2 R \varepsilon_0 \varepsilon \kappa \Psi_1^2 e^{-\kappa D} + 4\pi\alpha^2 R \varepsilon_0 \varepsilon \kappa \Psi_3^2 e^{-\kappa(D-2H)}, \quad (2.12)$$

which leads to strong attraction and jump-in mainly due to the interactions between the opposing bubbles on the two PS surfaces. Using the values  $\alpha \approx 0.5$ ,  $\Psi_1 \approx -45$  mV and  $\Psi_3 \approx -40$  mV<sup>113</sup>, Equation 2.12 predicts the modified DLVO forces between two PS surfaces in the presence of nanobubbles in 0.1 M NaCl,

as shown in the insert of Figure 2.9. The calculation considered the impact of bubbles of two different heights  $H \approx 20$  and  $5$  nm, which agrees well with the experimental results shown in Figure 2.2a and 2.5a for normal and degassed solutions respectively. The above analysis indicates that the attractive forces measured around 10–20 nm between polystyrene surfaces after degassing could be due to bridging of nanobubbles, which was not completely degassed, or the direct “pure” hydrophobic attraction of the polystyrene surfaces.

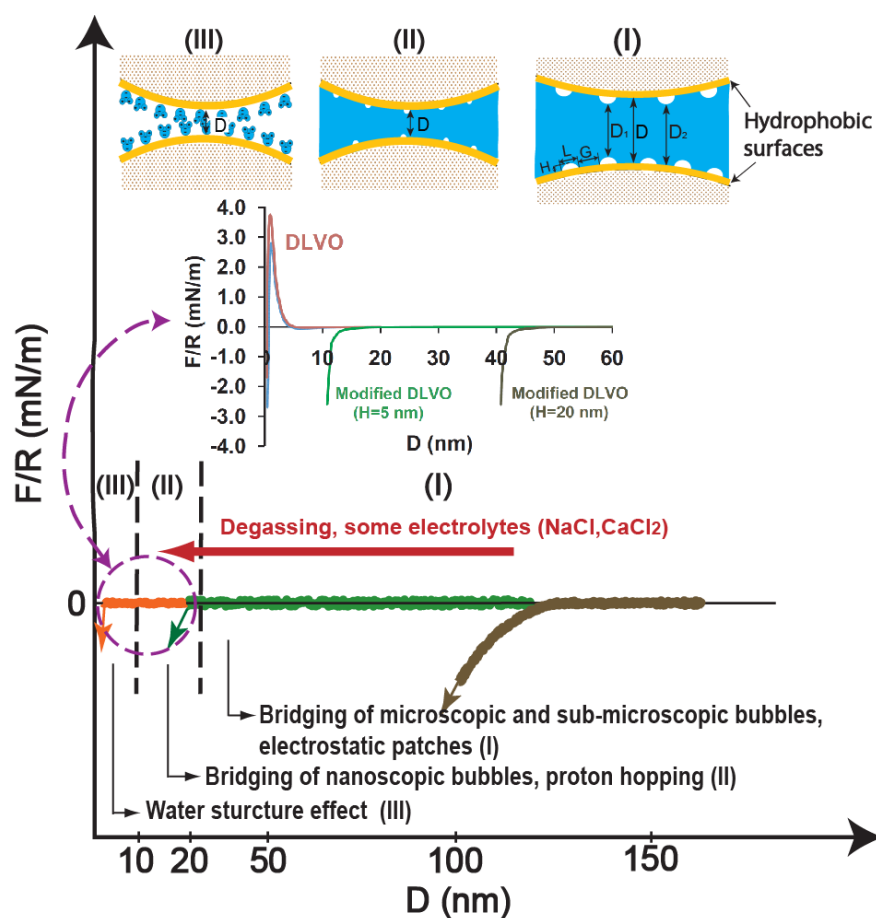


**Figure 2.9** A proposed three-regime hydrophobic interaction model: (I) a very long-range interaction regime from  $\sim 20$  nm to hundreds of nm, due to the bridging of microscopic and sub-microscopic bubbles or electrostatic

interactions; (II) an intermediate interaction regime around 10 nm (typically from several nm up to 10–20 nm), due to bridging of nanoscopic bubbles or enhanced Hamaker constant associated with enhanced proton hopping in water (so-called Grotthuss Effect); and (III) a short range interaction regime (from <1 nm to several nm), mainly due to the water structure changes (i.e., orientation, density and hydrogen bonding of water molecules) close to the hydrophobic surfaces. The insert shows the DLVO force-distance profiles for two polystyrene surfaces interacting in 0.1 M 1:1 electrolyte (e.g., NaCl) to illustrate the range of DLVO forces and modified DLVO forces in the presence of bubbles.

Our experimental results and the above analysis indicate that there are three regimes that could contribute to the hydrophobic interactions between polymer surfaces, i.e., (I) a very long-range interaction regime from tens of nm to hundreds of nm, (II) an intermediate interaction regime around 10 nm (typically from several nm up to 10–20 nm), and (III) a short range interaction regime (from <1 nm to several nm), which agrees with the abundant published experimental data for other hydrophobic systems (e.g., surfactant monolayers)<sup>1,13</sup> and a recent model proposed by Hammer et al.<sup>114</sup> The proposed three-regime hydrophobic interaction model is schematically shown in Figure 2.9. The very long range hydrophobic interaction regime (from 20 nm to hundreds of nm) is mainly due to the bridging of microscopic and sub-microscopic bubbles (and/or the possible electrostatic interaction present in certain systems because of the overturning of monolayers into charged bilayer patches or domains). The exact mechanisms for the intermediate range interaction regime (several nm to about 10–20 nm) and short range interaction regime (<1 nm to several nm) still remain unclear, which are generally considered to directly related to the hydrophobic effects or hydrophobic nature of the interacting surfaces and molecules. The

short range interaction regime is normally considered to be due to the water structure changes (i.e., orientation, density and hydrogen bonding of water molecules) close to the hydrophobic surfaces.

In search of the mechanism of the intermediate regime for the hydrophobic interactions, we noticed from FECO fringes that small air meniscus was formed sometimes after the polystyrene surfaces jumped into adhesive contact even in degassed solutions, which suggests that nanobubbles could still be present and possibly responsible for the interaction. It should be noted that degassing pressure applied in this study was only 50 mmHg which was probably not low enough to remove all the dissolved gas from the solution even after >10 hr of degassing. Recent studies have shown that hydrophobic liquids can be fully dispersed in water if the solution is fully (~99.999%) degassed.<sup>115-118</sup> Pashley and co-workers<sup>116</sup> have also found that degassing dramatically enhances electrical conductivity of water which is an indication of enhanced proton hopping mechanism (so-called Grotthuss Effect) in degassed water. Therefore, a systematic investigation of the impact of degassing pressure and *complete* (~99.999%) degassing of the solution on the surface forces between two hydrophobic polymer surfaces would help elucidate the real mechanism behind the intermediate regime of the hydrophobic interactions, i.e., bridging of nanoscopic bubbles or enhanced Hamaker constant associated with enhanced proton hopping in water.<sup>114</sup> Air also has limited solubility in PS, which could be a possible contributor to the nanobubbles on PS surfaces. Special care must also

be taken in future studies to remove the dissolved gas in polymer films and prevent the degassed solution from re-exposing to air.

## 2.4 Conclusion

Using a surface forces apparatus coupled with a top-view optical microscope, we have directly measured and visualized the interactions between two polystyrene surfaces. The impact of electrolytes (i.e., NaCl, CaCl<sub>2</sub>, HCl and CH<sub>3</sub>COOH) of different concentrations ranging from 0.001 to 1.0 M was investigated. It is evident that the long-range hydrophobic force measured (“jump-in” distances from tens of nm to several hundred nm) is due to bridging of microscopic and sub-microscopic bubbles on polystyrene surfaces. The range of the hydrophobic interaction between the polystyrene surfaces decreases with increasing the electrolyte concentration for NaCl and CaCl<sub>2</sub>, but shows no significant change for HCl and CH<sub>3</sub>COOH, which is related to the formation and stability of microscopic and sub-microscopic bubbles on hydrophobic surfaces under the different electrolyte conditions. Such electrolyte dependence is suggested to be due to the ion-pair complex adsorption at the bubble/solution interface. The electrolyte ions, which tend to deplete from the air-water interface (i.e. NaCl, CaCl<sub>2</sub>), are able to increase surface tension of water, decrease air solubility, suppress formation and/or stability of bubbles on PS surfaces and therefore shorten the range of the hydrophobic interaction under high concentrations. On the other hand, the ion pairs that have a tendency toward air-water interface (i.e. HCl, CH<sub>3</sub>COOH), can decrease surface tension of water, increase air solubility and have no detectable effect on the formation of bubbles

on polystyrene surfaces, and thus do not obviously affect the hydrophobic interactions.

The range of the hydrophobic interactions was reduced to about 10–20 nm by degassing the aqueous solutions, which was gradually recovered when re-exposing the degassed solution to air. Our results indicate that dissolved gasses in solutions play a crucial role in the hydrophobic interactions of polymer surfaces. Discontinuity on FECO fringes was observed between two close ( $\leq 20$  nm, but no contacted) PS surfaces in degassed aqueous solutions, which could be a direct experiment evidence of spontaneous cavitation of water between hydrophobic surfaces and/or bridging of nanoscopic bubbles. Our results support a three-regime hydrophobic interaction model: (1) a very long-range interaction regime from  $\sim 20$  nm to hundreds of nm, due to the bridging of microscopic and sub-microscopic bubbles (and/or electrostatic interaction present in certain systems because of the overturning of monolayers into charged bilayer patches or domains); (2) an intermediate interaction regime around 10 nm (typically from several nm up to 10–20 nm), due to bridging of nanoscopic bubbles or enhanced Hamaker constant associated with enhanced proton hopping in water (so-called Grotthuss Effect); and (3) a short range interaction regime (from  $< 1$  nm to several nm), mainly due to the water structure changes (i.e., orientation, density and hydrogen bonding of water molecules) close to the hydrophobic surfaces.

Strong adhesion was measured between two polystyrene surfaces in various electrolyte solutions, with the interfacial energy estimated to be  $\gamma = 42 \pm 5$

$\text{mJ/m}^2$ , very close to the values measured in air 35–43  $\text{mJ/m}^2$ . Interesting fracture patterns were observed associated with the separation of two hydrophobic surfaces in aqueous solution, but not in air, which indicates the hydrophobic forces play an important role in adhesion-induced fracture of polymer surfaces and thin films. A rigorous theoretical analysis in future study on the adhesion-induced fracture mechanism for hydrophobic polymer surfaces/thin films in aqueous solutions is of both practical and fundamental importance.

The ion specificity observed here for the hydrophobic interaction between two polymer surfaces provide implications for other systems in which the hydrophobic interaction plays important roles, e.g., mineral flotation, protein folding, self-assembly of amphiphilic molecules in aqueous solutions. Using polystyrene as a model system, our study provides new insight into the basic hydrophobic interaction mechanism of polymers and biomacromolecules.

## **2.5 Supporting information**

Fringes of equal chromatic order (FECO) and corresponding top view optical microscope images for two polystyrene surfaces separating in degassed 0.001 M NaCl are shown in Figure S2.1. Note the initiation of crack propagation in the polymer film associated with the separation was indicated by red arrows in Figure S2.1b. Further crack propagation within the polymer film during separation resulted from the jump out from adhesive contact and the fracture pattern were observed by top view optical microscope and corresponding discontinuity in FECO.

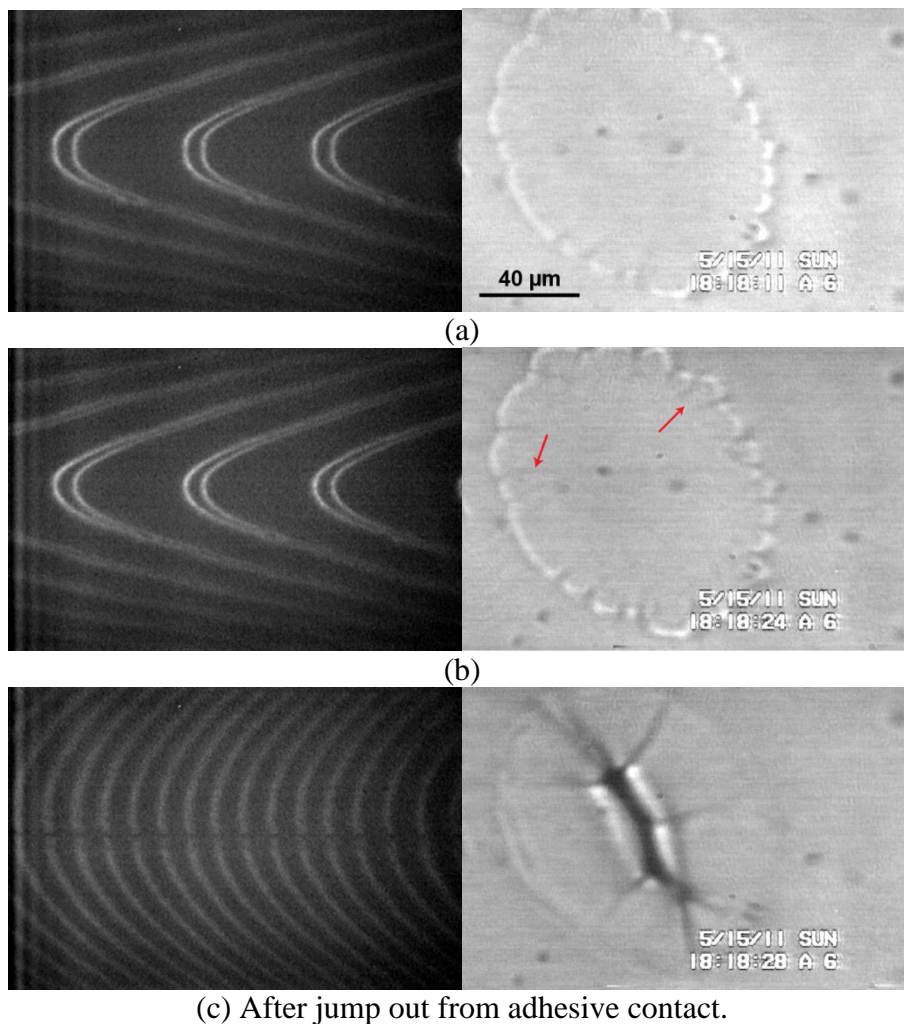


**Figure S2.1.** FECO (left) and corresponding top view optical microscope images (right) of two polystyrene surfaces in degassed 0.001 M NaCl (a) before separation (b) during separation (c) after jump out from adhesive contact.

Figures S2.2 and S2.3 show the top view optical microscope images for the air meniscus growth through outward fingering patterns outside the contact region of two polystyrene surfaces.



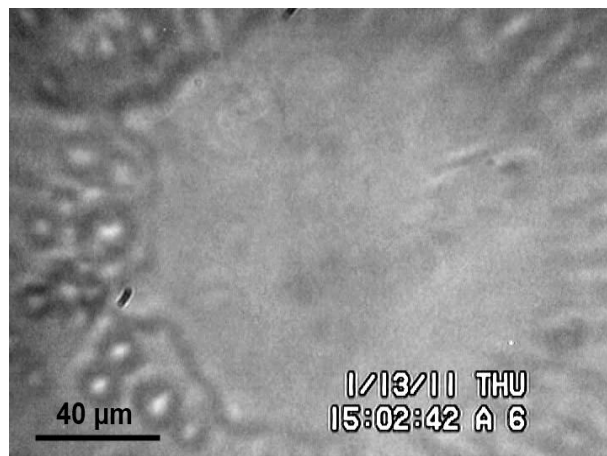


**Figure S2.2** Air meniscus growth through fingering patterns as observed by top view microscope after PS surfaces jumped into contact in 1.0 M CH<sub>3</sub>COOH.

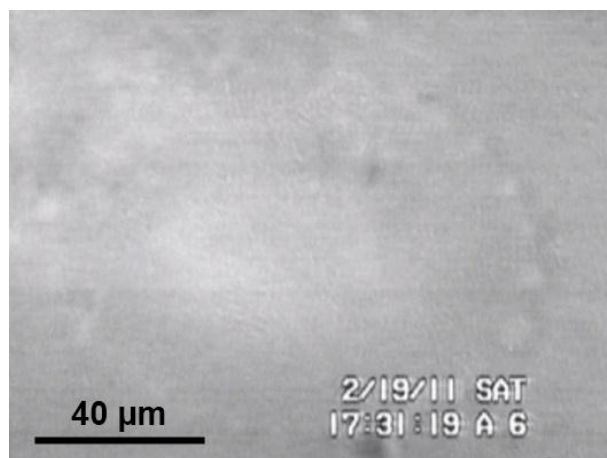


**Figure S2.3** Air meniscus growth through fingering patterns as observed by top view microscope after PS surfaces jumped into contact in 0.1 M NaCl.

## References

- (1) Meyer, E. E.; Rosenberg, K. J.; Israelachvili, J. Recent Progress in Understanding Hydrophobic Interactions. *Proc. Natl. Acad. Sci. U. S. A.* **2006**, *103*, 15739-15746.

- (2) Israelachvili, J. N. In *Intermolecular and Surface Forces*; Academic Press: 2011.
- (3) Karaman, M. E.; Meagher, L.; Pashley, R. M. Surface Chemistry of Emulsion Polymerization. *Langmuir* **1993**, *9*, 1220-1227.
- (4) Israelachvili, J.; Pashley, R. The Hydrophobic Interaction is Long Range, Decaying Exponentially with Distance. *Nature* **1982**, *300*, 341-342.
- (5) Doshi, D. A.; Watkins, E. B.; Israelachvili, J. N.; Majewski, J. Reduced Water Density at Hydrophobic Surfaces: Effect of Dissolved Gases. *Proc. Natl. Acad. Sci. U. S. A.* **2005**, *102*, 9458-9462.
- (6) Craig, V. S. J.; Ninham, B. W.; Pashley, R. M. Direct Measurement of Hydrophobic Forces: A Study of Dissolved Gas, Approach Rate, and Neutron Irradiation. *Langmuir* **1999**, *15*, 1562-1569.
- (7) Tyrrell, J. W. G.; Attard, P. Atomic Force Microscope Images of Nanobubbles on a Hydrophobic Surface and Corresponding Force-Separation Data. *Langmuir* **2002**, *18*, 160-167.
- (8) Christenson, H. K.; Claesson, P. M. Cavitation and the Interaction between Macroscopic Hydrophobic Surfaces. *Science* **1988**, *239*, 390-392.
- (9) Christenson, H. K.; Claesson, P. M.; Berg, J.; Herder, P. C. Forces between Fluorocarbon Surfactant Monolayers: Salt Effects on the Hydrophobic Interaction. *J. Phys. Chem.* **1989**, *93*, 1472-1478.
- (10) Craig, V. S. J.; Ninham, B. W.; Pashley, R. M. Study of the Long-Range Hydrophobic Attraction in Concentrated Salt Solutions and its Implications for Electrostatic Models. *Langmuir* **1998**, *14*, 3326-3332.

- (11) Parker, J. L.; Claesson, P. M.; Attard, P. Bubbles, Cavities, and the Long-Range Attraction between Hydrophobic Surfaces. *J. Phys. Chem.* **1994**, *98*, 8468-8480.
- (12) Ishida, N.; Sakamoto, M.; Miyahara, M.; Higashitani, K. Attraction between Hydrophobic Surfaces with and without Gas Phase. *Langmuir* **2000**, *16*, 5681-5687.
- (13) Christenson, H. K.; Claesson, P. M. Direct Measurements of the Force between Hydrophobic Surfaces in Water. *Adv. Colloid Interface Sci.* **2001**, *91*, 391-436.
- (14) Tsao, Y. H.; Yang, S. X.; Evans, D. F. Interactions between Hydrophobic Surfaces. Dependence on Temperature and Alkyl Chain Length. *Langmuir* **1991**, *7*, 3154-3159.
- (15) Christenson, H. K.; Parker, J. L.; Yaminsky, V. V. Comment on "Interactions between Hydrophobic Surfaces. Dependence on Temperature and Alkyl Chain Length". *Langmuir* **1992**, *8*, 2080.
- (16) Perkin, S.; Kampf, N.; Klein, J. Stability of Self-Assembled Hydrophobic Surfactant Layers in Water. *J. Phys. Chem. B* **2005**, *109*, 3832-3837.
- (17) Meyer, E. E.; Lin, Q.; Hassenkam, T.; Oroudjev, E.; Israelachvili, J. N. Origin of the Long-Range Attraction between Surfactant-Coated Surfaces. *Proc. Natl. Acad. Sci. U. S. A.* **2005**, *102*, 6839-6842.
- (18) Tsao, Y.; Evans, D. F.; Wennerstrom, H. Long-Range Attraction between a Hydrophobic Surface and a Polar Surface is Stronger than that between Two Hydrophobic Surfaces. *Langmuir* **1993**, *9*, 779-785.

- (19) Israelachvili, J. N.; Pashley, R. M. Measurement of the Hydrophobic Interaction between Two Hydrophobic Surfaces in Aqueous Electrolyte Solutions. *J. Colloid Interface Sci.* **1984**, *98*, 500-514.
- (20) Pratt, L. R.; Chandler, D. Theory of the Hydrophobic Effect. *J. Chem. Phys.* **1977**, *67*, 3683-3704.
- (21) Claesson, P. M.; Blom, C. E.; Herder, P. C.; Ninham, B. W. Interactions between Water-Stable Hydrophobic Langmuir-Blodgett Monolayers on Mica. *J. Colloid Interface Sci.* **1986**, *114*, 234-242.
- (22) Craig, V. S. J.; Ninham, B. W.; Pashley, R. M. Effect of Electrolytes on Bubble Coalescence. *Nature* **1993**, *364*, 317-319.
- (23) Attard, P. Nanobubbles and the Hydrophobic Attraction. *Adv. Colloid Interface Sci.* **2003**, *104*, 75-91.
- (24) Considine, R. F.; Drummond, C. J. Long-Range Force of Attraction between Solvophobic Surfaces in Water and Organic Liquids Containing Dissolved Air. *Langmuir* **2000**, *16*, 631-635.
- (25) Meagher, L.; Craig, V. S. J. Effect of Dissolved Gas and Salt on the Hydrophobic Force between Polypropylene Surfaces. *Langmuir* **1994**, *10*, 2736-2742.
- (26) Considine, R. F.; Hayes, R. A.; Horn, R. G. Forces Measured between Latex Spheres in Aqueous Electrolyte: Non-DLVO Behavior and Sensitivity to Dissolved Gas. *Langmuir* **1999**, *15*, 1657-1659.

- (27) Christenson, H. K.; Fang, J. F.; Ninham, B. W.; Parker, J. L. Effect of Divalent Electrolyte on the Hydrophobic Attraction. *J. Phys. Chem.* **1990**, *94*, 8004-8006.
- (28) Christenson, H. K.; Claesson, P. M.; Parker, J. L. Hydrophobic Attraction: A Reexamination of Electrolyte Effects. *J. Phys. Chem.* **1992**, *96*, 6725-6728.
- (29) Mahnke, J.; Stearnes, J.; Hayes, R. A.; Fornasiero, D.; Ralston, J. The Influence of Dissolved Gas on the Interactions between Surfaces of different Hydrophobicity in Aqueous Media. *Phys. Chem. Chem. Phys.* **1999**, *1*, 2793-2798.
- (30) Snoswell, D. R. E.; Duan, J.; Fornasiero, D.; Ralston, J. Colloid Stability and the Influence of Dissolved Gas. *J. Phys. Chem. B* **2003**, *107*, 2986-2994.
- (31) Taunton, H. J.; Toprakcioglu, C.; Fetters, L. J.; Klein, J. Forces between Surfaces Bearing Terminally Anchored Polymer Chains in Good Solvents. *Nature* **1988**, *332*, 712-714.
- (32) Klein, J. Shear, Friction and Lubrication Forces between Polymer-Bearing Surfaces. *Annu. Rev. Mater. Sci.* **1996**, *26*, 581-612.
- (33) Cretont, C.; Kramer, E. J. Failure Mechanisms of Polymer Interfaces Reinforced with Block Copolymers. *Macromolecules* **1992**, *25*, 3075-3088.
- (34) Leger, L.; Raphael, E.; Hervet, H. Surface-Anchored Polymer Chains: Their Role in Adhesion and Friction. *Adv. Polym. Sci.* **1999**, *138*, 185-225.

- (35) Crosby, A. J.; Shull, K. R.; Lakrout, H.; Creton, C. Deformation and Failure Modes of Adhesively Bonded Elastic Layers. *J. Appl. Phys.* **2000**, 88, 2956-2966.
- (36) Kramer, E. J. Microscopic and Molecular Fundamentals of Crazing. *Adv. Polym. Sci.* **1983**, 52-3, 1-56.
- (37) Creton, C.; Kramer, E. J.; Brown, H. R.; Hui, C. Adhesion and Fracture of Interfaces between Immiscible Polymers: From the Molecular to the Continuum Scale. *Adv. Polym. Sci.* **2002**, 156, 53-136.
- (38) Maeda, N.; Chen, N.; Tirrell, M.; Israelachvili, J. N. Adhesion and Friction Mechanisms of Polymer-on-Polymer Surfaces. *Science* **2002**, 297, 379-382.
- (39) Prager, S.; Tirrell, M. The Healing Process at polymer-polymer Interfaces. *J. Chem. Phys.* **1981**, 75, 5194-5198.
- (40) Zeng, H.; Maeda, N.; Chen, N.; Tirrell, M.; Israelachvili, J. Adhesion and Friction of Polystyrene Surfaces Around Tg. *Macromolecules* **2006**, 39, 2350-2363.
- (41) Zeng, H.; Zhao, B.; Tian, Y.; Tirrell, M.; Gary Leala, L.; Israelachvili, J. N. Transient Surface Patterns during Adhesion and Coalescence of Thin Liquid Films. *Soft Matter* **2007**, 3, 88-93.
- (42) Zeng, H.; Tian, Y.; Zhao, B.; Tirrell, M.; Israelachvili, J. Transient Interfacial Patterns and Instabilities Associated with Liquid Film Adhesion and Spreading. *Langmuir* **2007**, 23, 6126-6135.

- (43) Schmitt, F. -.; Ederth, T.; Weidenhammer, P.; Claesson, P.; Jacobasch, H. -. Direct Force Measurements on Bulk Polystyrene using the Bimorph Surface Forces Apparatus. *J. Adhes. Sci. Technol.* **1999**, *13*, 79-96.
- (44) Israelachvili, J.; Min, Y.; Akbulut, M.; Alig, A.; Carver, G.; Greene, W.; Kristiansen, K.; Meyer, E.; Pesika, N.; Rosenberg, K.; Zeng, H. Recent Advances in the Surface Forces Apparatus (SFA) Technique. *Rep. Prog. Phys.* **2010**, *73*, 1-16.
- (45) Israelachvili, J. N.; Adams, G. E. Measurement of Forces between Two Mica Surfaces in Aqueous Electrolyte Solutions in the Range 0-100 nm. *J. Chem. Soc., Faraday Trans. 1* **1978**, *74*, 975-1001.
- (46) Israelachvili, J. N.; McGuiggan, P. M. Adhesion and Short-Range Forces between Surfaces. Part I New Apparatus for Surface Force Measurements. *J. Mater. Res.* **1990**, *5*, 2223-2231.
- (47) Meyer, E. E.; Lin, Q.; Israelachvili, J. N. Effects of Dissolved Gas on the Hydrophobic Attraction between Surfactant-Coated Surfaces. *Langmuir* **2005**, *21*, 256-259.
- (48) Carambassis, A.; Jonker, L. C.; Attard, P.; Rutland, M. W. Forces Measured between Hydrophobic Surfaces due to a Submicroscopic Bridging Bubble. *Phys. Rev. Lett.* **1998**, *80*, 5357-5360.
- (49) Zeng, H.; Zhao, B.; Israelachvili, J. N.; Tirrell, M. Liquid- to Solid-Like Failure Mechanism of Thin Polymer Films at Micro- and Nanoscales. *Macromolecules* **2010**, *43*, 538-542.

- (50) Zeng, H.; Tian, Y.; Zhao, B.; Tirrell, M.; Israelachvili, J. Transient Surface Patterns and Instabilities at Adhesive Junctions of Viscoelastic Films. *Macromolecules* **2007**, *40*, 8409-8422.
- (51) Saffman, P. G.; Taylor, G. The Penetration of a Fluid into a Porous Medium Or Hele-Shaw Cell Containing a More Viscous Liquid. *Proc. R. Soc. London, Ser. A* **1958**, *245*, 312-329.
- (52) Zhang, X. H.; Quinn, A.; Ducker, W. A. Nanobubbles at the Interface between Water and a Hydrophobic Solid. *Langmuir* **2008**, *24*, 4756-4764.
- (53) Zhang, X. H.; Maeda, N.; Craig, V. S. J. Physical Properties of Nanobubbles on Hydrophobic Surfaces in Water and Aqueous Solutions. *Langmuir* **2006**, *22*, 5025-5035.
- (54) Zhang, X. H.; Khan, A.; Ducker, W. A. A Nanoscale Gas State. *Phys. Rev. Lett.* **2007**, *98*, 136101.
- (55) Ducker, W. A. Contact Angle and Stability of Interfacial Nanobubbles. *Langmuir* **2009**, *25*, 8907-8910.
- (56) Yang, J.; Duan, J.; Fornasiero, D.; Ralston, J. Very Small Bubble Formation at the Solid-Water Interface. *J. Phys. Chem. B* **2003**, *107*, 6139-6147.
- (57) Henry, C. L.; Craig, V. S. J. The Link between Ion Specific Bubble Coalescence and Hofmeister Effects is the Partitioning of Ions within the Interface. *Langmuir* **2010**, *26*, 6478-6483.
- (58) Craig, V. S. J.; Ninham, B. W.; Pashley, R. M. The Effect of Electrolytes on Bubble Coalescence in Water. *J. Phys. Chem.* **1993**, *97*, 10192-10197.



- (59) Pashley, R. M.; McGuiggan, P. M.; Ninham, B. W.; Evans, D. F. Attractive Forces between Uncharged Hydrophobic Surfaces: Direct Measurements in Aqueous Solution. *Science* **1985**, 229, 1088-1089.
- (60) Huang, X.; Margulis, C. J.; Berne, B. J. Dewetting-Induced Collapse of Hydrophobic Particles. *Proc. Natl. Acad. Sci. U. S. A.* **2003**, 100, 11953-11958.
- (61) Lum, K.; Chandler, D.; Weeks, J. D. Hydrophobicity at Small and Large Length Scales. *J. Phys. Chem. B* **1999**, 103, 4570-4577.
- (62) Giovambattista, N.; Rossky, P. J.; Debenedetti, P. G. Effect of Pressure on the Phase Behavior and Structure of Water Confined between Nanoscale Hydrophobic and Hydrophilic Plates. *Phys. Rev. E* **2006**, 73, 041604.
- (63) Leung, K.; Luzar, A.; Bratko, D. Dynamics of Capillary Drying in Water. *Phys. Rev. Lett.* **2003**, 90, 065502.
- (64) Yang, J.; Duan, J.; Fornasiero, D.; Ralston, J. Kinetics of CO<sub>2</sub> Nanobubble Formation at the solid/water Interface. *Phys. Chem. Chem. Phys.* **2007**, 9, 6327-6332.
- (65) Attard, P. Bridging Bubbles between Hydrophobic Surfaces. *Langmuir* **1996**, 12, 1693-1695.
- (66) Eriksson, J. C.; Ljunggren, S. Comments on the Alleged Formation of Bridging Cavities/Bubbles between Planar Hydrophobic Surfaces. *Langmuir* **1995**, 11, 2325-2328.

- (67) Attard, P. Thermodynamic Analysis of Bridging Bubbles and a Quantitative Comparison with the Measured Hydrophobic Attraction. *Langmuir* **2000**, *16*, 4455-4466.
- (68) Kralchevsky, P. A. Conditions for Stable Attachment of Fluid Particles to Solid Surfaces. *Langmuir* **1996**, *12*, 5951-5955.
- (69) Ball, P. How to Keep Dry in Water. *Nature* **2003**, *423*, 25-26.
- (70) Ishida, N.; Inoue, T.; Miyahara, M.; Higashitani, K. Nano Bubbles on a Hydrophobic Surface in Water Observed by Tapping-Mode Atomic Force Microscopy. *Langmuir* **2000**, *16*, 6377-6380.
- (71) Steitz, R.; Gutberlet, T.; Hauss, T.; Klosgen, B.; Krastev, R.; Schemmel, S.; Simonsen, A. C.; Findenegg, G. H. Nanobubbles and their Precursor Layer at the Interface of Water Against a Hydrophobic Substrate. *Langmuir* **2003**, *19*, 2409-2418.
- (72) Lou, S. T.; Ouyang, Z. Q.; Zhang, Y.; Li, X. J.; Hu, J.; Li, M. Q.; Yang, F. *J. J. Vac. Sci. Technol. B* **2000**, *18*, 2573-2575.
- (73) Craig, V. S. J. Very Small Bubbles at surfaces—the Nanobubble Puzzle. *Soft Matter* **2011**, *7*, 40-48.
- (74) Zhang, X. H.; Zhang, X.; Sun, J.; Zhang, Z.; Li, G.; Fang, H.; Xiao, X.; Zeng, X.; Hu, J. Detection of Novel Gaseous States at the Highly Oriented Pyrolytic Graphite-Water Interface. *Langmuir* **2007**, *23*, 1778-1783.
- (75) Yang, S. J.; Dammer, S. M.; Bremond, N.; Zandvliet, H. J. W.; Kooij, E. S.; Lohse, D. Characterization of Nanobubbles on Hydrophobic Surfaces in Water. *Langmuir* **2007**, *23*, 7072-7077.

- (76) Kunz, W.; Henle, J.; Ninham, B. W. 'Zur Lehre Von Der Wirkung Der Salze' (about the Science of the Effect of Salts): Franz Hofmeister's Historical Papers. *Curr. Opin. Colloid Interface Sci.* **2004**, *9*, 19-37.
- (77) Zangi, R.; Hagen, M.; Berne, B. J. Effect of Ions on the Hydrophobic Interaction between Two Plates. *J. Am. Chem. Soc.* **2007**, *129*, 4678-4686.
- (78) Jungwirth, P.; Tobias, D. J. Specific Ion Effects at the Air/Water Interface. *Chem. Rev.* **2006**, *106*, 1259-1281.
- (79) Kunz, W.; Nostro, P. L.; Ninham, B. W. The Present State of Affairs with Hofmeister Effects. *Curr. Opin. Colloid Interface Sci.* **2004**, *9*, 1-18.
- (80) Henry, C. L.; Craig, V. S. J. Ion-Specific Influence of Electrolytes on Bubble Coalescence in Nonaqueous Solvents. *Langmuir* **2008**, *24*, 7979-7985.
- (81) Holz, M.; Grunder, R.; Sacco, A.; Meleleo, A. Nuclear Magnetic Resonance Study of Self-Association of Small Hydrophobic Solutes in Water: Salt Effects and the Lyotropic Series. *J. Chem. Soc., Faraday Trans.* **1993**, *89*, 1215-1222.
- (82) Zangi, R.; Berne, B. J. Aggregation and Dispersion of Small Hydrophobic Particles in Aqueous Electrolyte Solutions. *J. Phys. Chem. B* **2006**, *110*, 22736-22741.
- (83) Bunkin, N. F.; Kiseleva, O. A.; Lobeyev, A. V.; Movchan, T. G.; Ninham, B. W.; Vinogradova, O. I. Effect of Salts and Dissolved Gas on Optical Cavitation Near Hydrophobic and Hydrophilic Surfaces. *Langmuir* **1997**, *13*, 3024-3028.

- (84) Pegram, L. M.; Record, M. T. J. Hofmeister Salt Effects on Surface Tension Arise from Partitioning of Anions and Cations between Bulk Water and the Air-Water Interface. *J. Phys. Chem. B* **2007**, *111*, 5411-5417.
- (85) Battino, R., Ed.; In *Solubility data series, Nitrogen and air*; Pergamon Press: 1982; Vol. 10.
- (86) Wenling, Y.; Peisheng, M.; Chunfang, W.; Yingxiang, L. Determination and Correlation of Equilibrium Stability Data of Oxygen(1) - Acetic Acid(2) - Water(3) System. *J. Chem. Ind. Eng. (China, Chin. Ed. )* **2005**, *56*, 1169-1174.
- (87) Lang, W.; Zander, R. Salting-Out of Oxygen from Aqueous Electrolyte Solutions: Prediction and Measurement. *Ind. Eng. Chem.* **1986**, *25*, 775-782.
- (88) Weissenborn, P. K.; Pugh, R. J. Surface Tension of Aqueous Solutions of Electrolytes: Relationship with Ion Hydration, Oxygen Solubility, and Bubble Coalescence. *J. Colloid Interface Sci.* **1996**, *184*, 550-563.
- (89) Vakarelski, I. U.; Manica, R.; Tang, X.; O'Shea, S. J.; Stevens, G. W.; Grieser, F.; Dagastine, R. R.; Chan, D. Y. C. Dynamic Interactions between Microbubbles in Water. *Proc. Natl. Acad. Sci. U. S. A.* **2010**, *107*, 11177-11182.
- (90) Chan, D. Y. C.; Klaseboer, E.; Manica, R. Theory of Non-Equilibrium Force Measurements Involving Deformable Drops and Bubbles. *Adv. Colloid Interface Sci.* **2011**, *165*, 70-90.
- (91) Chan, D. Y. C.; Klaseboer, E.; Manica, R. Film Drainage and Coalescence between Deformable Drops and Bubbles. *Soft Matter* **2011**, *7*, 2235-2264.

- (92) Frank, H. S.; Evans, M. W. Free Volume and Entropy in Condensed Systems III. Entropy in Binary Liquid Mixtures; Partial Molal Entropy in Dilute Solutions; Structure and Thermodynamics in Aqueous Electrolytes. *J. Chem. Phys.* **1945**, *13*, 507-532.
- (93) Head-Gordon, T. Is Water Structure Around Hydrophobic Groups Clathrate-Like? *Proc. Natl. Acad. Sci. U. S. A.* **1995**, *92*, 8308-8312.
- (94) Tielrooij, K. J.; Garcia-Araez, N.; Bonn, M.; Bakker, H. J. Cooperativity in Ion Hydration. *Science* **2010**, *328*, 1006-1009.
- (95) Skinner, J. L. Following the Motions of Water Molecules in Aqueous Solutions. *Science* **2010**, *328*, 985-986.
- (96) Ji, M.; Odelius, M.; Gaffney, K. J. Large Angular Jump Mechanism Observed for Hydrogen Bond Exchange in Aqueous Perchlorate Solution. *Science* **2010**, *328*, 1003-1005.
- (97) Tabor, R. F.; Chan, D. Y. C.; Grieser, F.; Dagastine, R. R. Anomalous Stability of Carbon Dioxide in pH-Controlled Bubble Coalescence. *Angew. Chem., Int. Ed.* **2011**, *50*, 3454-3456.
- (98) Browne, C.; Tabor, R. F.; Chan, D. Y. C.; Dagastine, R. R.; Ashokkumar, M.; Grieser, F. Bubble Coalescence during Acoustic Cavitation in Aqueous Electrolyte Solutions. *Langmuir* **2011**, *27*, 12025-12032.
- (99) Johnson, K. L.; Kendall, K.; Roberts, A. D. Surface Energy and the Contact of Elastic Solids. *Proc. R. Soc. London, Ser. A* **1971**, *324*, 301-313.

- (100) Chen, N.; Maeda, N.; Tirrell, M.; Israelachvili, J. Adhesion and Friction of Polymer Surfaces: The Effect of Chain Ends. *Macromolecules* **2005**, *38*, 3491-3503.
- (101) Horn, R. G.; Israelachvili, J. N.; Pribac, F. Measurement of the Deformation and Adhesion of Solids in Contact. *J. Colloid Interface Sci.* **1987**, *115*, 480-492.
- (102) Derjaguin, B. V.; Muller, V. M.; Toporov, Y. P. Effect of Contact Deformations on the Adhesion of Particles. *J. Colloid Interface Sci.* **1975**, *53*, 314-326.
- (103) Muller, V. M.; Yushchenko, V. S.; Derjaguin, B. V. General Theoretical Consideration of the Influence of Surface Forces on Contact Deformations and the Reciprocal Adhesion of Elastic Spherical Particles. *J. Colloid Interface Sci.* **1983**, *92*, 92-101.
- (104) Muller, V. M.; Yushchenko, V. S.; Derjaguin, B. V. On the Influence of Molecular Forces on the Deformation of an Elastic Sphere and its Sticking to a Rigid Plane. *J. Colloid Interface Sci.* **1980**, *77*, 91-101.
- (105) Maugis, D. Adhesion of Spheres: The JKR-DMT Transition using a Dugdale Model. *J. Colloid Interface Sci.* **1992**, *150*, 243-269.
- (106) Donald, A. M.; Kramer, E. J. The Mechanism for Craze-Tip Advance in Glassy Polymers. *Philos. Mag.* **1981**, *43*, 857-870.
- (107) Zeng, H.; Tirrell, M.; Israelachvili, J. Limit Cycles in Dynamic Adhesion and Friction Processes: A Discussion. *J. Adhes.* **2006**, *82*, 933-943.

- (108) Midmore, B. R.; Hunter, R. J. The Effect of Electrolyte Concentration and Co-Ion Type on the Zeta-Potential of Polystyrene Latices. *J. Colloid Interface Sci.* **1988**, *122*, 521-529.
- (109) Usui, S.; Barouch, E. Effect of Adsorbed Layers on the Van Der Waals Interaction between Particles and Bubbles in Aqueous Media. *J. Colloid Interface Sci.* **1990**, *137*, 281-288.
- (110) Mishchuk, N.; Ralston, J.; Fornasiero, D. Influence of Dissolved Gas on Van Der Waals Forces between Bubbles and Particles. *J. Phys. Chem. A* **2002**, *106*, 689-696.
- (111) Mishchuk, N. A. The Model of Hydrophobic Attraction in the Framework of Classical DLVO Forces. *Adv. Colloid Interface Sci.* **2011**, *168*, 149-166.
- (112) Mishchuk, N.; Ralston, J.; Fornasiero, D. Influence of very Small Bubbles on particle/bubble Heterocoagulation. *J. Colloid Interface Sci.* **2006**, *301*, 168-175.
- (113) Najafi, A. S.; Drelich, J.; Yeung, A.; Xu, Z.; Masliyah, J. A Novel Method of Measuring Electrophoretic Mobility of Gas Bubbles. *J. Colloid Interface Sci.* **2007**, *308*, 344-350.
- (114) Hammer, M. U.; Anderson, T. H.; Chaimovich, A.; Shell, M. S.; Israelachvili, J. The Search for the Hydrophobic Force Law. *Faraday Discuss.* **2010**, *146*, 299-308.
- (115) Pashley, R. M. Effect of Degassing on the Formation and Stability of Surfactant-Free Emulsions and Fine Teflon Dispersions. *J. Phys. Chem. B* **2003**, *107*, 1714-1720.

- (116) Pashley, R. M.; Rzechowicz, M.; Pashley, L. R.; Francis, M. J. De-Gassed Water is a Better Cleaning Agent. *J. Phys. Chem. B* **2005**, *109*, 1231-1238.
- (117) Francis, M. J.; Gulati, N.; Pashley, R. M. The Dispersion of Natural Oils in De-Gassed Water. *J. Colloid Interface Sci.* **2006**, *299*, 673-677.
- (118) Pashley, R. M.; Francis, M. J.; Rzechowicz, M. The Hydrophobicity of Non-Aqueous Liquids and their Dispersion in Water Under Degassed Conditions. *Curr. Opin. Colloid Interface Sci.* **2008**, *13*, 236-244.



## **Chapter 3. Interaction Mechanism between Hydrophobic and Hydrophilic Surfaces: using Polystyrene and Mica as a Model System<sup>3</sup>**

### **3.1 Introduction**

Hydrophobic interaction is generally referred to as long range attractive force between hydrophobic molecules or surfaces in aqueous solutions which is normally stronger than the interaction predicted by the classical Derjaguin–Landau–Verwey–Overbeek (DLVO) theory and has been widely studied over the past three decades.<sup>1-14</sup> Some of the proposed mechanisms for the hydrophobic interaction include water structural effects near hydrophobic surfaces, correlated dipole interactions and bridging of nanobubbles.<sup>3, 10, 14, 15</sup> Hydrophobic interactions play an important role in many biological and non-biological systems, and a wide range of phenomena involve interactions between molecules, particles or surfaces with dissimilar hydrophobicity.<sup>16, 17</sup> For example, many biological phenomena such as cell-cell and cell-surface interactions and industrial processes such as mineral floatation involve the interactions between hydrophobic and hydrophilic molecules, particles and surfaces. The interactions between hydrophobic and hydrophilic surfaces have been studied both theoretically and experimentally using different techniques such as surface forces apparatus (SFA) and atomic force microscopy (AFM).<sup>18-27</sup> Different systems have been investigated for the interactions between

---

<sup>3</sup> A version of this chapter has been submitted for publication, Langmuir (2013).

hydrophilic and hydrophobic surfaces, most of which involve surfactant monolayer or air bubble, such as mica vs. hydrophobized mica,<sup>18</sup> silica vs. silanated glass,<sup>20, 25</sup> silica vs. self assembled monolayers of hexadecanethiol on glass,<sup>21</sup> and silica vs. air bubble.<sup>24, 26, 27</sup> The interaction between hydrophilic silica particles and air bubbles was reported to be repulsive and the range and magnitude of the repulsion decreased with electrolyte concentration.<sup>24</sup> The impact of surfactants on interactions between hydrophilic silica particle and air bubble was investigated by AFM, and repulsive forces were measured in the surfactant-free solutions which changed with the introduction of different types of surfactants of various concentrations.<sup>26</sup> The interactions between mica and hydrophobized mica were measured by SFA, and attractive forces were reported that decreased with electrolyte concentration, which were suggested to be due to the electrostatic forces between negatively charged mica and positively charged modified mica surfaces.<sup>18</sup> Repulsive forces were measured between hydrophobic and hydrophilic self-assembled monolayers and decreased with electrolyte concentration, which could be well described by electric double layer forces while van der Waals attraction did not contribute to the overall interaction.<sup>21</sup> Long range attractive force was measured between a hydrophilic silica sphere and a hydrophobic silanated glass plate in pure water by AFM which was concluded to be due to nanobubbles bridging.<sup>25</sup> The previous studies suggest that the interactions between hydrophilic and hydrophobic surfaces depend on several factors such as type of interacting surfaces and the aqueous medium between the surfaces.

Most of the previous research on interactions between surfaces with asymmetrical hydrophobicity focuses on chemically bonded or self-assembled surfactant systems. Few studies have been reported on polymeric systems,<sup>22</sup> although much progress has been made in understanding the fundamental interaction mechanisms (e.g., adhesion, friction and lubrication) of polymer surfaces and brushes in both air and liquid media.<sup>17, 28-38</sup> Polymers of different hydrophobicities have a wide range of engineering and biomedical applications. Nevertheless the understanding of hydrophobic interactions of polymer surfaces still remains limited.<sup>13, 17</sup> In a previous report, we investigated the interaction mechanism between two hydrophobic polystyrene surfaces and explored the impact of various types of electrolytes and dissolved gas, and our results supported a three-regime hydrophobic interaction model.<sup>13</sup> In the present work, hydrophobic polystyrene (PS) and hydrophilic mica were chosen as a model system, and the interactions between PS and mica surfaces were directly probed using an SFA. The effects of electrolytes (i.e., NaCl, CaCl<sub>2</sub>, HCl, CH<sub>3</sub>COOH and NaOH), electrolyte concentration (ranging from 0.001 and 1.0 M), dissolved gas, and surface hydrophobicity (modulated through surface oxidation) on the surface interactions between PS and mica were investigated.

### 3.2 Materials and Methods

Polystyrene (Polysciences Inc., USA) of  $M_w=1,000,000$  g/mol and  $M_w/M_n \approx 1.10$  was used as received. Polystyrene solution was prepared by dissolving PS in toluene (Fisher Scientific, Canada, HPLC grade). Two droplets of PS solution was spin coated on freshly cleaved mica surface to obtain PS thin films. PS films

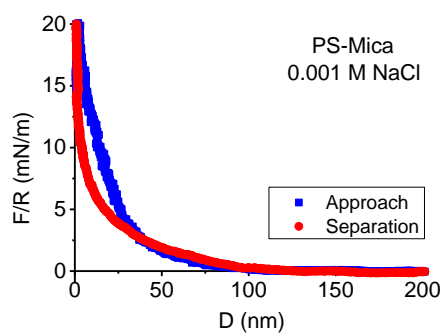
were stored under vacuum overnight (>12 h) to remove the solvent to obtain a film of uniform thickness. High-purity anhydrous sodium chloride (Sigma-Aldrich, 99.999+%), anhydrous calcium chloride (Sigma-Aldrich, 99.99+%) and sodium hydroxide (Sigma-Aldrich, 99.99%) were used as received (sealed in glass or quartz ampules) or calcined following the same method reported by Pashley and Ninham et al. to remove the possible trace organic impurities.<sup>5, 39</sup> Both calcined and uncalcined salts were used in the measurements of surface forces, and no difference was observed. Acetic acid (Fisher Scientific, Canada, >99%) and hydrochloric acid (Fisher Scientific, Canada, ACS Grade) were used as received. Milli-Q water (with resistance  $\geq 18.2 \text{ M}\Omega \text{ cm}$ ) was used to prepare the aqueous solutions. An SFA coupled with a top-view optical microscope was used to measure the interaction forces between PS and mica surfaces in different electrolyte solutions and visualize the interaction processes. Detailed setup for SFA experiments has been reported previously.<sup>40-42</sup> Briefly, a thin mica sheet of 1–5  $\mu\text{m}$  was glued onto a cylindrical silica disk (radius  $R=2 \text{ cm}$ ). The back surfaces of mica substrates were coated with  $\sim 50 \text{ nm}$  semi-reflective layer of silver, which were required to obtain multiple-beam interference fringes of equal chromatic order (FECO) to monitor the surface separation, shape and deformations in real time and in situ. The two surfaces were then mounted into the SFA chamber in a crossed-cylinder configuration, which was equivalent to a sphere of radius  $R$  approaching a flat surface based on the Derjaguin approximation. The normal forces between the two surfaces were determined by using the Hooke's Law through measuring the deflection of double-cantilever

‘force springs’. During the experiments, FECO fringes and top-view microscope images were recorded simultaneously to monitor and visualize the surface separation and deformations as reported previously.<sup>13, 33, 35, 40-42</sup> Degassing of the solutions was carried out following a method by stirring under vacuum as reported recently.<sup>13, 43</sup> In order to investigate the effect of surface hydrophobicity on the surface interactions, PS surfaces were treated in a UV-Ozone chamber (BioForce Nanosciences, USA) for different time prior to SFA experiments. The PS surfaces treated by UV-Ozone were further characterized by AFM, X-ray photoelectron spectroscopy (XPS) and contact angle measurements. For surface force measurements, at least three different interaction positions were tested for the same pair of surfaces and the experiments were reproduced for at least three times for each solution condition. All the experiments were conducted at room temperature. All the operations were carried out in a dust-free laminar flow cabinet at room temperature (23 °C).

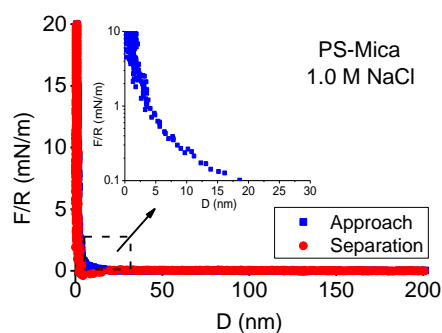
### 3.3 Results and Discussion

Figure 3.1 shows the typical force-distance profiles of PS vs. mica during approach and separation in five different electrolyte solutions namely NaCl, CaCl<sub>2</sub>, NaOH, HCl and CH<sub>3</sub>COOH of concentrations of 0.001 and 1.0 M as measured by SFA. As shown in Figure 3.1, long range repulsion was measured between PS and mica surfaces at low concentration of 0.001 M for all electrolyte solutions. At low concentration of 0.001 M, repulsion was found to initiate between the surfaces ranging from ~50 to ~100 nm for all the electrolytes tested, and it was also found that the range of repulsion could differ from one

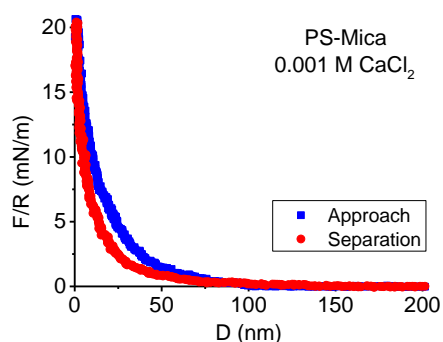
measurement to another for the same electrolyte solution, which was similar to the observations for the interaction between two PS surfaces reported recently.<sup>13</sup> Hysteresis was also often observed in the force-distance profiles during approach-separation cycles in 0.001 M electrolyte solutions. As the electrolyte concentration was increased to 1.0 M, the interaction forces between PS and mica surfaces became different from those in 0.001 M, while the change of the interaction forces varied in the different electrolyte solutions. As shown in Figure 3.1b, 3.1d, and 3.1f, the range of repulsion was dramatically reduced to less than 20 nm in NaCl, CaCl<sub>2</sub> and NaOH solutions as the electrolyte concentration increases to 1.0 M and the repulsion dramatically increased at the separation distances of  $D < 2$  nm which is mainly due to hydration and electrostatic double layer forces.<sup>16</sup> It should be noted that the Debye length  $1/\kappa$  of electrical double layer was  $< 1$  nm in Figure 3.1b, 3.1d and 3.1f and the relatively long range repulsion ( $\sim 20$  nm) measured was most likely due to the presence of nanobubbles on PS (also discussed later).<sup>14</sup> On the other hand, in HCl and CH<sub>3</sub>COOH solutions (see Figure 3.1h and 3.1j), the range of repulsion was not significantly decreased as observed in the other three electrolyte solutions. It is also interesting to note that the magnitude of the repulsion was reduced at the same separation distance as the concentration was increased from 0.001 to 1.0 M in HCl and CH<sub>3</sub>COOH solutions, as shown in Figure 3.1g, 3.1h, 3.1i and 3.1j.



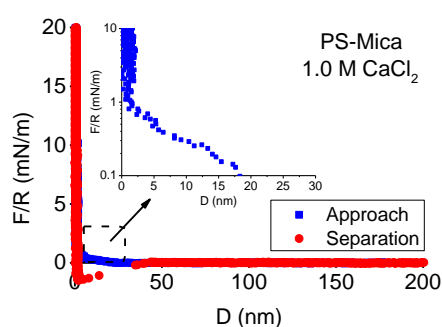
(a)



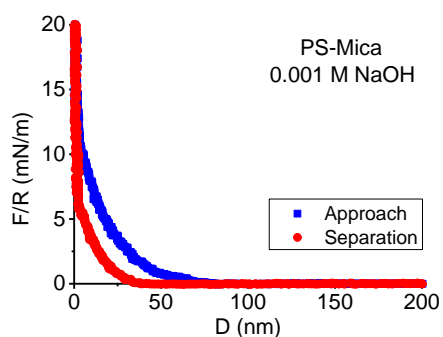
(b)



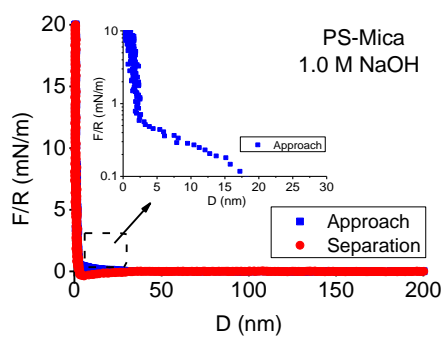
(c)



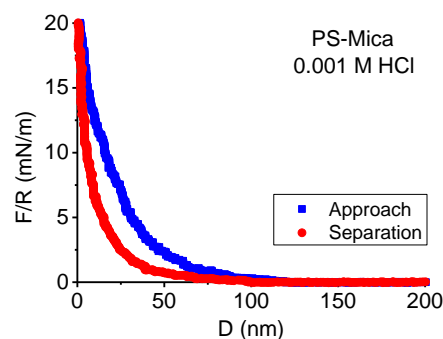
(d)



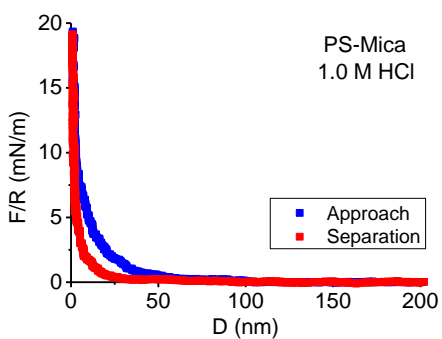
(e)



(f)



(g)



(h)

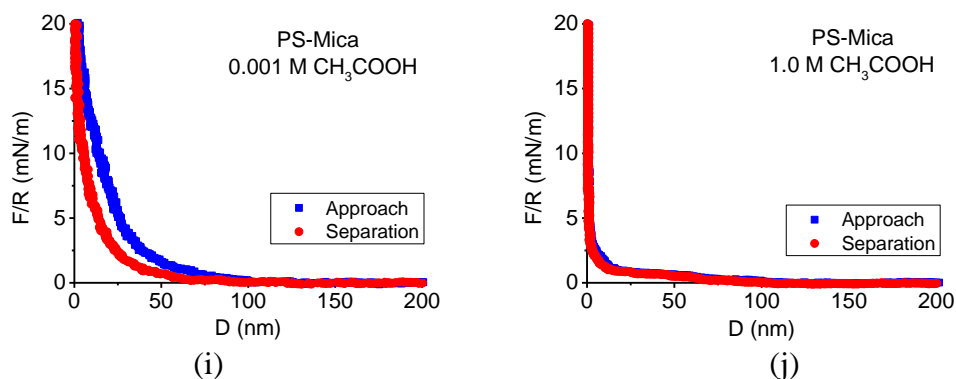
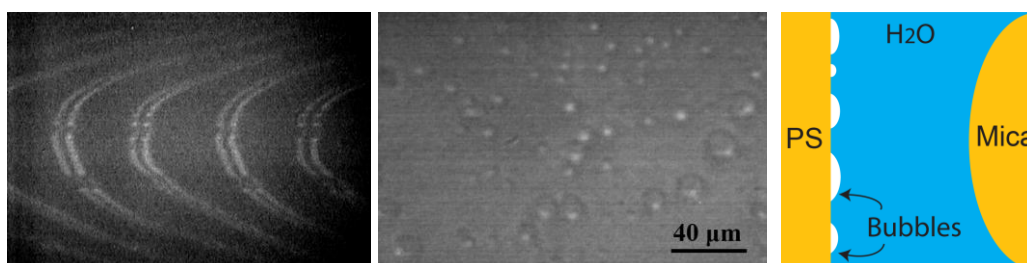


**Figure 3.1** Force-distance profiles of PS vs. mica during approach and separation as measured by SFA in (a and b) NaCl, (c and d) CaCl<sub>2</sub>, (e and f) NaOH, (g and h) HCl, (i and j) CH<sub>3</sub>COOH of concentration of 0.001 M and 1.0 M respectively.

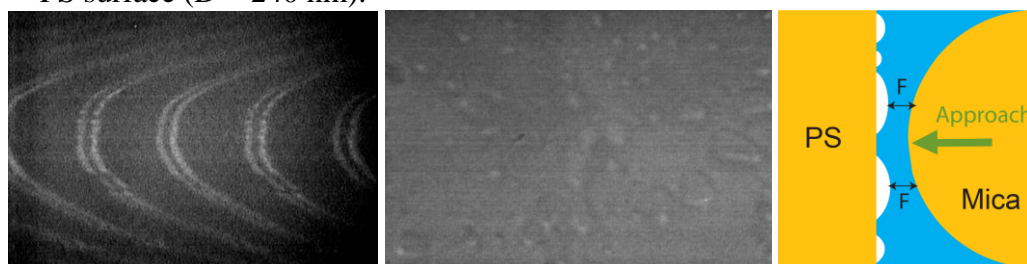
We recently reported the presence of microscopic and submicroscopic bubbles on PS surface and the effects of these bubbles on the interactions between two PS surfaces in different electrolyte solutions.<sup>13</sup> In order to directly visualize the interaction between PS and mica surfaces, a top-view optical microscope was coupled with SFA during the surface force measurements. Figure 3.2 shows typical FECO fringes and the corresponding top-view microscope images associated with the interaction of PS and mica surfaces in 0.001 M NaCl solution. It is evident from Figure 3.2 that small bubbles were initially present on the PS surface, as shown in both the optical microscope images and the discontinuities in FECO fringes due to the refractive index difference of water and air (Figure 3.2a). As the two surfaces approached each other the bubbles on the PS surface were deformed and confined between the two surfaces (Figure 3.2b). When the surfaces came into contact, the bubbles were displaced out to the periphery of the contact area (Figure 3.2c). The surfaces were then kept in contact for ~ 1 min before separation started. As the



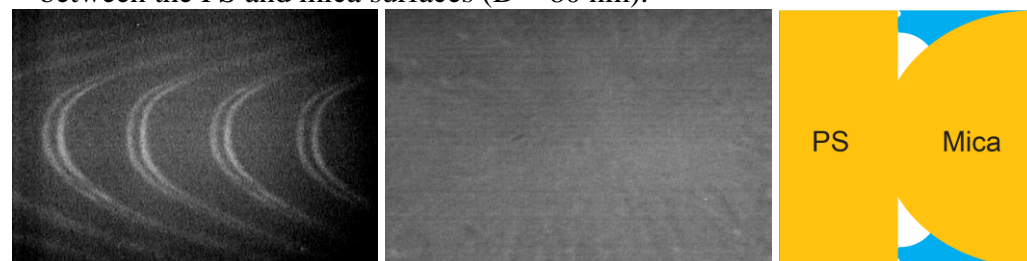
surfaces were separated from contact, small bubbles were observed again on the PS surface (Figure 3.2d). It was noted that the morphology/size of the bubbles formed on the PS surface during separation (Figure 3.2d) was slightly different from those before approach (Figure 3.2a).



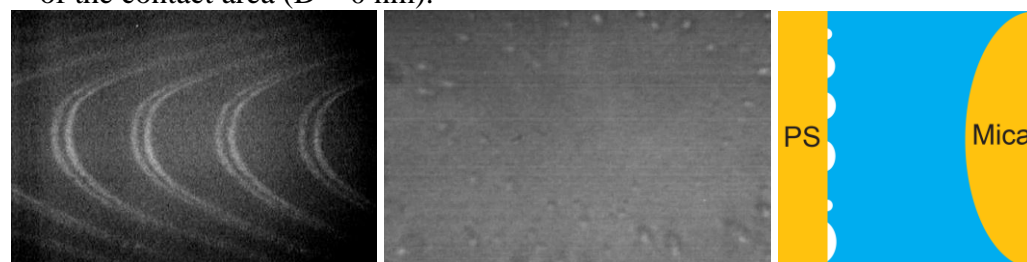
(a) PS and mica surfaces were far from each other and bubbles were present on PS surface ( $D \sim 240$  nm).



(b) As the surfaces approached each other, bubbles were deformed and confined between the PS and mica surfaces ( $D \sim 80$  nm).



(c) The two surfaces were in contact and bubbles were displaced to the periphery of the contact area ( $D \sim 0$  nm).



(e) As the two surfaces were separated, small bubbles appeared on the PS surface ( $D \sim 220$  nm).

**Figure 3.2** FECO (left), the corresponding top-view optical microscope images (middle) and illustration (right) associated with the interaction between PS and mica surfaces in 0.001 M NaCl solution. (a) PS and mica surfaces were far from each other, and microscopic and submicroscopic bubbles were present on the PS surface. (b) As the two surfaces approached each other, bubbles were deformed and confined between them. (c) Bubbles were displaced to the periphery of the contact area and two surfaces were in contact. (d) As the surfaces were separated bubbles appeared again on PS surface.

The results in Figures 3.1 and 3.2 indicate that the long range repulsion between PS and mica surfaces in different electrolyte solutions was mainly due to the surface forces associated with the presence of air bubbles on PS surface. As van der Waals forces and electric double layer forces generally exist between interacting surfaces in aqueous solutions, the Derjaguin–Landau–Verwey–Overbeek (DLVO) theory is applied here to compare with the experimental results. Therefore, the interaction forces between PS and mica surfaces in the presence of bubbles are comprised of van der Waals ( $F^{vdw}$ ) and electric double layer forces ( $F^{dl}$ ) between Mica-water-PS (1-2-4) and mica-water-bubble (1-2-3) as shown in Figure 3.3a. The modified DLVO forces can be given as<sup>9, 13, 44-46</sup>

$$F(D) = F_{124}^{vdw} + F_{123}^{vdw} + F_{124}^{dl} + F_{123}^{dl}, \quad (3.1)$$

where 1, 2, 3 and 4 refer to mica, aqueous solution, bubble and PS respectively. The modified van der Waals and double layer forces taking into account the effect of bubbles are given as

$$F_{124}^{vdw} = -\frac{(1-\alpha)A_{124}R}{6D^2}, \quad (3.2a)$$

$$F_{123}^{vdw} = -\frac{\alpha A_{123}R}{6(D-H)^2}, \quad (3.2b)$$

$$F_{124}^{dl} = 4\pi(1-\alpha)R\epsilon_0\epsilon\kappa\psi_1\psi_4\exp(-\kappa D), \quad (3.3a)$$

$$F_{123}^{dl} = 4\pi\alpha R\epsilon_0\epsilon\kappa\psi_1\psi_3 \exp(-\kappa(D-H)), \quad (3.3b)$$

where  $\alpha = S_{bubble}/S_{total}$  is the ratio of bubble-covered area to the total surface area of the PS surface,  $A$  is the Hamaker constant,  $R$  the radius of interacting surfaces,  $H$  the average height of bubbles,  $\epsilon$  the relative permittivity,  $1/\kappa$  the Debye length and  $\psi$  the surface potential. The Hamaker constant  $A_{123}$  for two materials 1 and 2 interacting in medium 3 is given by<sup>16</sup>

$$A_{132} \approx \frac{3}{4}k_B T \left( \frac{\epsilon_1 - \epsilon_3}{\epsilon_1 + \epsilon_3} \right) \left( \frac{\epsilon_2 - \epsilon_3}{\epsilon_2 + \epsilon_3} \right) + \frac{3h_p \nu_e}{8\sqrt{2}} \frac{(n_1^2 - n_3^2)(n_2^2 - n_3^2)}{(n_1^2 + n_3^2)^{1/2} (n_2^2 + n_3^2)^{1/2} \left\{ (n_1^2 + n_3^2)^{1/2} + (n_2^2 + n_3^2)^{1/2} \right\}} \quad (3.4)$$

where  $k_B$  is the Boltzmann constant,  $\epsilon$  is the dielectric permittivity,  $n$  is the refractive index,  $h_p$  is the Plank's constant and  $\nu_e$  is the main electronic absorption frequency. The Debye length  $1/\kappa$  is given by

$$1/\kappa = \left( \epsilon_0 \epsilon_s k_B T / \sum_i \rho_{\infty i} e_0^2 z_i^2 \right)^{1/2}, \quad (3.5)$$

where  $\epsilon_0$  is the dielectric permittivity of free space,  $\epsilon_s$  is the dielectric constant of solution,  $e_0$  is the elementary charge of a single electron,  $\rho_{\infty i}$  is the number density of  $i$ th ion in the bulk solution and  $z_i$  is the valancy of the  $i$ th ion.

It should be noted that in the above analysis it is assumed that the average width of the bubbles  $L$  and the average distance between the bubbles  $G$  are much bigger than the average height  $H$ , which is a very reasonable assumption as  $G$  and  $L$  are on the order of micrometres and  $H$  is on the order of nanometres or tens of nanometres (see Figure 3.2 and 3.3).<sup>13</sup> The pancake-shaped bubbles on hydrophobic surfaces have also been imaged directly using AFM by other

researchers.<sup>15, 47-49</sup> Using equations 3.1 to 3.3 and the typical values of  $\alpha \approx 0.5$ ,  $A_{123} \approx -2.2 \times 10^{-20}$  J,  $A_{124} \approx 2.0 \times 10^{-20}$  J and  $H \approx 50$  and  $7$  nm,  $1/\kappa \approx 9.6$  and  $0.3$  nm,  $\psi_1 \approx -75$  and  $-60$  mV,  $\psi_3 \approx -80$  and  $-40$  mV and  $\psi_4 \approx -60$  and  $-50$  mV,<sup>16, 50, 51</sup>, corresponding to  $0.001$  and  $1.0$  M NaCl, respectively, the interaction forces between PS and mica in  $0.001$  and  $1.0$  M NaCl are calculated and compared with typical experimental results as shown in Figure 3.3b. It should be noted that in the above calculation it is assumed that the bubble height  $H$  is considered to decrease as the separation distance  $D$  decreases due to the repulsive DLVO forces between mica and air bubbles which is consistent with bubble deformations observed during experiments (see Figure 3.2). As it is clear from Figure 3.3b, the theoretical calculations based on modified DLVO theory match well with the experimental forces measured.

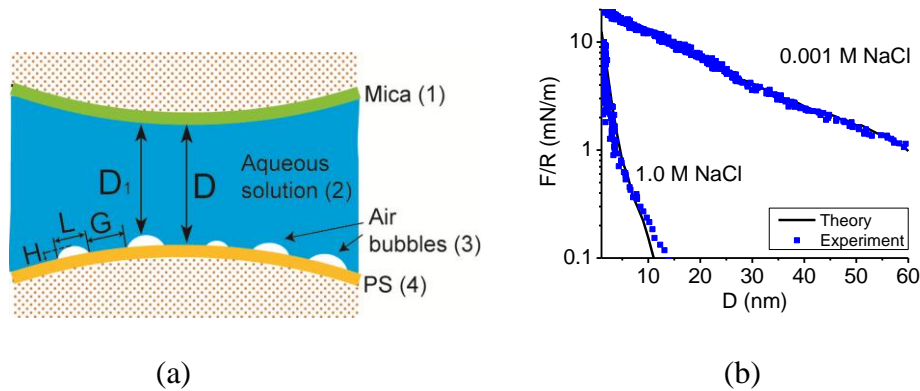


**Figure 3.3** (a) Schematic of the interactions between PS and mica surfaces in the presence of air bubbles. (b) Comparison between typical experimental force-distance profile of PS-mica in  $0.001$  and  $1.0$  M NaCl (in blue dots) and the theoretical prediction by a modified DLVO model (in black line).

Recent studies have shown the important role of solution pH in the coalescence of bubbles.<sup>52, 53</sup> The pH values of the solutions used in this study were 6.0–6.4 in NaCl and CaCl<sub>2</sub>, 2.4 and 0.2 in 0.001 and 1.0 M HCl, 4.0 and 2.3 in 0.001 and 1.0 M CH<sub>3</sub>COOH, 10.5 and 13.2 in 0.001 and 1.0 M NaOH solutions, respectively. The solution pH could affect the surface potential of PS, mica and air bubbles.<sup>16</sup> It is noted that the bubble size is another important factor that can affect the range of surface interactions. Therefore, both the size of bubbles adsorbed on PS and the surface potentials of PS, mica and bubbles can be affected by the solution conditions and contribute to the surface forces measured.

From Figures 3.1 to 3.3, it is evident that at low electrolyte concentration of 0.001 M, dissolved air and bubbles present on PS surface play an important role in the long range repulsion measured. However as the concentration of NaCl, CaCl<sub>2</sub> and NaOH solutions increase to 1.0 M, the range of the repulsion dramatically decreases from >50 nm to <20 nm, which is mainly due to the suppression of the formation of bubbles on hydrophobic PS surface by these electrolytes (see Figure 3.1b, 3.1d, 3.1f). In contrast, 1.0 M HCl and CH<sub>3</sub>COOH solutions have no significant effect on the range of repulsion between PS and mica surfaces (see Figure 3.1h and 3.1i), which suggests that high concentration of HCl and CH<sub>3</sub>COOH does not significantly affect the formation of bubbles on PS surface. The results about the effects of electrolytes on the formation of bubbles on hydrophobic surfaces are consistent with the recent report on the effect of electrolytes on the interactions between two PS surfaces.<sup>13</sup> The fact that

different ions show specific effects on various colloidal and biological phenomena is generally referred to as ion specificity. The ion specificity has been observed in many phenomena such as hydrophobic interactions, bubble coalescence and protein solubility in aqueous solutions.<sup>13, 54-57</sup> Each ion has its own specific effect on the surface tension of water, air solubility in aqueous solution and hydrogen bond network of water molecules which can eventually affect the bubble formation on hydrophobic surfaces. The surface tension of water can be changed due to the presence of specific ions and their tendency towards the air-water interface which is generally described by the Gibbs adsorption isotherm:

$$\Gamma_{\text{ion}}^{\text{H}_2\text{O}} = -\frac{1}{RT} \left( \frac{\partial \gamma}{\partial \ln(a_{\text{ion}})} \right)_T, \quad (3.6)$$

where  $\Gamma_{\text{ion}}^{\text{H}_2\text{O}}$  is the relative surface excess,  $R$  is the universal gas constant,  $T$  is temperature,  $\gamma$  is the surface tension of water and  $a_{\text{ion}}$  is activity of ion. The parameter relative surface excess  $\Gamma_{\text{ion}}^{\text{H}_2\text{O}}$  defines the affinity of ions for the interface.<sup>56</sup> Based on equation 3.6, for electrolytes that increase the surface tension of water (*e.g.*, NaCl, CaCl<sub>2</sub> and NaOH), the relative surface excess  $\Gamma_{\text{ion}}^{\text{H}_2\text{O}} < 0$ , and thus the ions tend to be depleted from the air-water interface.<sup>56, 58,</sup>

<sup>59</sup> As the concentration of NaCl, CaCl<sub>2</sub> and NaOH solutions increases to 1.0 M, the surface tension of water increases, air solubility decreases and ions are depleted from the air-water interface, which eventually suppress the formation and stability of air bubbles on PS surfaces. Therefore the shortened range and weakened repulsion between PS and mica surfaces in 1.0 M solutions of NaCl,

CaCl<sub>2</sub> and NaOH (as compared to that measured in 0.001 M solutions) directly resulted from the reduction of size and number of air bubbles formed on the PS surface. On the other hand, for electrolytes that decrease the surface tension of water (*e.g.*, HCl and CH<sub>3</sub>COOH), the relative surface excess  $\Gamma_{\text{ion}}^{\text{H}_2\text{O}} > 0$ , and the ions tend to be adsorbed at the air-water interface. As the concentration of HCl and CH<sub>3</sub>COOH increases to 1.0 M, the surface tension of water decreases, air solubility increases and ions are adsorbed at the air-water interface,<sup>13, 56, 58</sup> and these electrolytes do not significantly affect the formation and stability of bubble on PS surface. Therefore the long-range repulsion between PS and mica surfaces in HCl and CH<sub>3</sub>COOH solutions was not dramatically affected as the concentration of the electrolyte increased to 1.0 M. The hysteresis in the force-distance curves during approach and separation cycles shown in Figure 3.1 were most likely due to the change of morphology of the bubbles under confinement between PS and mica, as also observed in Figure 3.2.

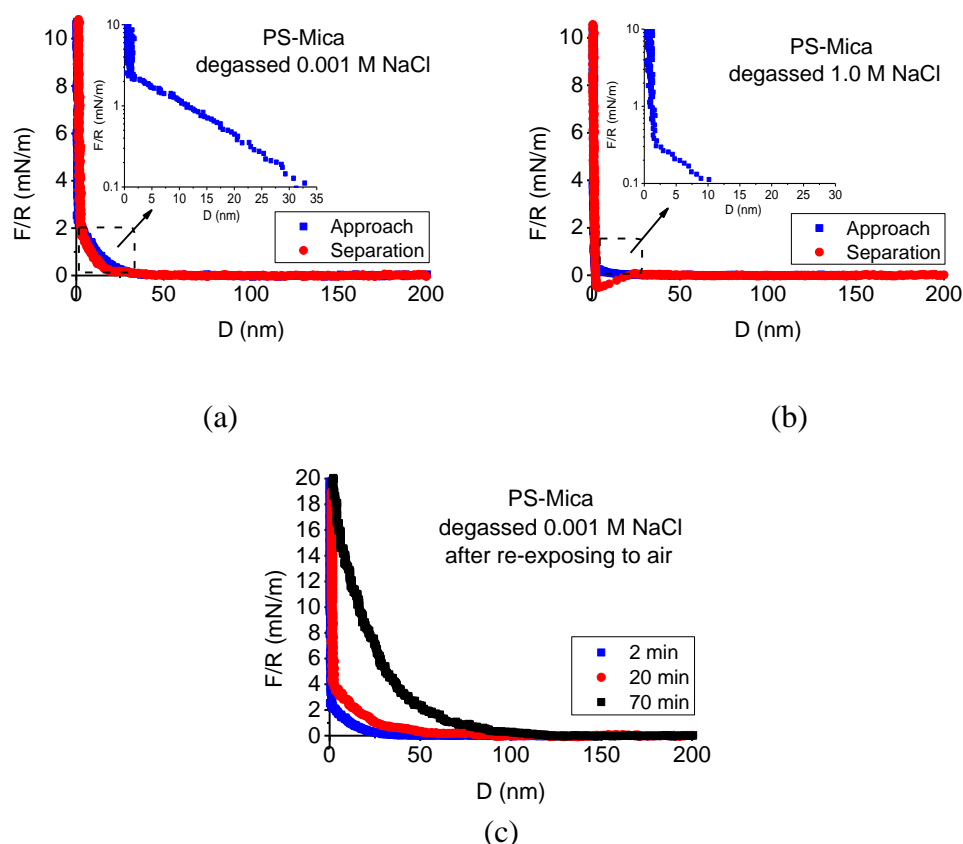
Adhesion of  $F_{\text{adh}}/R \sim 0.4, 1.5$  and  $0.4$  mN/m was measured during separation of mica and PS surfaces in 1.0 M solutions of NaCl, CaCl<sub>2</sub> and NaOH as shown in Figure 3.1b, 3.1d and 3.1f respectively, while no adhesion was measured for HCl and CH<sub>3</sub>COOH solutions. The observed adhesion between PS and mica in 1.0 M solutions of NaCl, CaCl<sub>2</sub> and NaOH could be mainly due to (1) van der Waals interaction between PS and mica and (2) cation- $\pi$  interactions between adsorbed cations on mica (*i.e.* Na<sup>+</sup> and Ca<sup>2+</sup>) and benzene rings of PS under confinement.<sup>60</sup> The measured difference in adhesion of the different electrolytes might be due to the ion selectivity of cation- $\pi$  interactions as

observed in previous studies.<sup>60, 61</sup> It should be noted that as the electrolyte concentration of NaCl, CaCl<sub>2</sub> and NaOH increases to 1.0 M, more cations are adsorbed as counter ions on the mica surface which can change the charge properties of the stern plane and shear plane of the electric double layer on mica.<sup>62, 63</sup> On the other hand, as HCl and CH<sub>3</sub>COOH do not significantly affect the formation of bubbles on PS surface, therefore intimate contact cannot be easily achieved between PS and mica surfaces and no adhesion was detected during separation.

In order to further investigate the role of dissolved gas and bubbles on the interaction between hydrophilic mica and hydrophobic PS surfaces, electrolyte solutions were degassed and the typical results for interaction in degassed NaCl solutions are shown in Figure 3.4. As shown in Figure 3.4a, the range of the repulsion dramatically reduces to <30 nm for degassed 0.001 M NaCl solution as compared to about 50–100 nm for non-degassed 0.001 M solution. The repulsion range during approach was <10 nm in degassed 1 M NaCl solution as shown in Figure 3.4b, slightly shorter than that in non-degassed 1 M solution. Adhesion of  $F_{adh}/R \sim 0.5$  mN/m was measured in degassed 1.0 M NaCl which was slightly higher than that in non-degassed solution, and no adhesion was observed for degassed 0.001 M NaCl. As shown in Figure 3.4c, the range of repulsion gradually increases from <30 nm to >100 nm after re-exposing the degassed solution to air for more than one hour. The results of degassed solutions further demonstrate the role of dissolved gas and adsorbed bubbles on PS surface on the interaction between mica and PS surfaces. Apparently, the effect of degassing



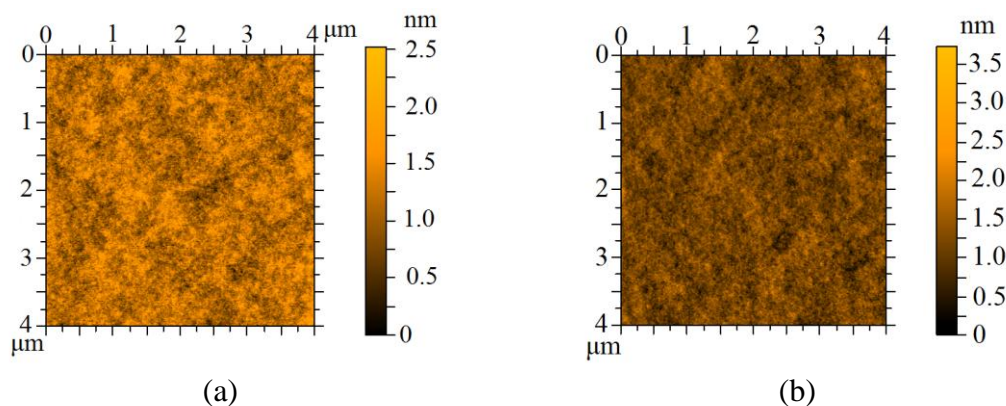
aqueous solution on reducing the absorbed bubbles on hydrophobic surface seems not to be as significant as increasing salt concentration (based on Figure 3.2a, 3.2b and Figure 3.4a, 3.4b), and one possible factor could be that the electrolyte solution might not be “completely” degassed as the degassing pressure was only 50 mmHg. There might be some nanobubbles still present on the hydrophobic PS surface in the degassed solution.



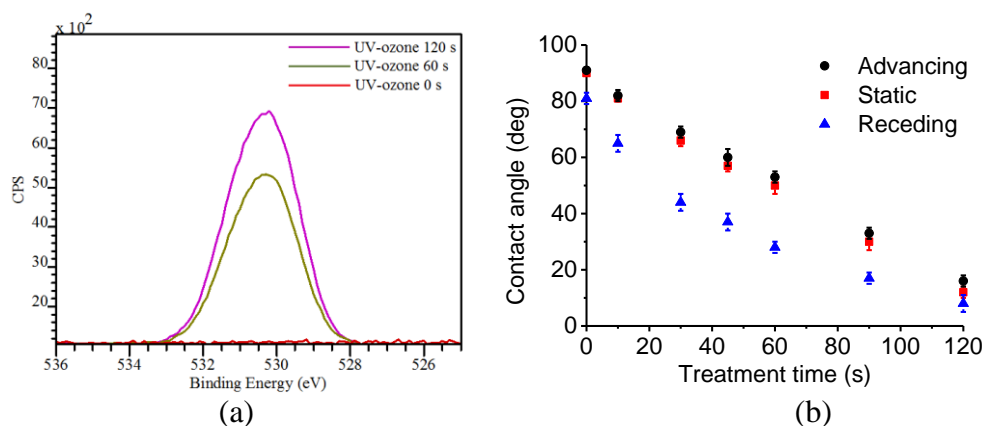
**Figure 3.4** Force-distance profiles of PS vs. mica in (a) degassed 0.001 M NaCl, (b) degassed 1.0 M NaCl, and (c) degassed 0.001 M NaCl after re-exposing to air for different times.

The effect of hydrophobicity of PS surface on the interaction of the hydrophobic-hydrophilic PS-mica system was also investigated. The PS surfaces were treated in a UV-ozone chamber before the force measurements in order to modify their hydrophobicity. Typical AFM images of untreated and UV-ozone

treated PS surfaces in air are shown in Figure 3.5, which shows that UV-ozone treatment has no significant effect on the roughness of the PS surface. UV-ozone treated PS surfaces were further characterized using XPS and contact angle measurements as shown in Figure 3.6. The normalized XPS spectra of oxygen (O1s) in Figure 3.6a shows that no oxygen was detected on untreated PS, while the oxygen peak increases with UV-ozone treatment time, which is indicative of the presence of polar groups such as C=O. The static, advancing and receding contact angles of water on UV-ozone treated PS surfaces is shown in Figure 3.6b. Figure 3.6b shows that the water contact angle on treated PS surfaces decreases with increasing UV-ozone treatment time, which is consistent with the XPS results and indicates that the PS surfaces became more hydrophilic with increase of hydrophilic groups on the surface as a result of UV-ozone treatment. Figure 3.6b shows that there is a hysteresis of  $10^{\circ}$  to  $25^{\circ}$  between the advancing and receding contact angles, which is more pronounced for the cases with shorter UV-ozone treatment time (i.e. 20–60 s). The contact angle hysteresis is most likely due to the chemical heterogeneity of the UV-ozone treated PS surfaces.<sup>16</sup> It is noted that the static water contact angle did not change within the time frame of measurements (i.e. ~5 min) which suggests that overturning of polar functional groups at the treated PS/water interface was negligible. The treated PS surfaces were normally transferred to SFA within 5 min after exposure to UV-ozone, which rules out any temporal effects (i.e. overturning of polar functional groups) on surface hydrophobicity of treated PS.



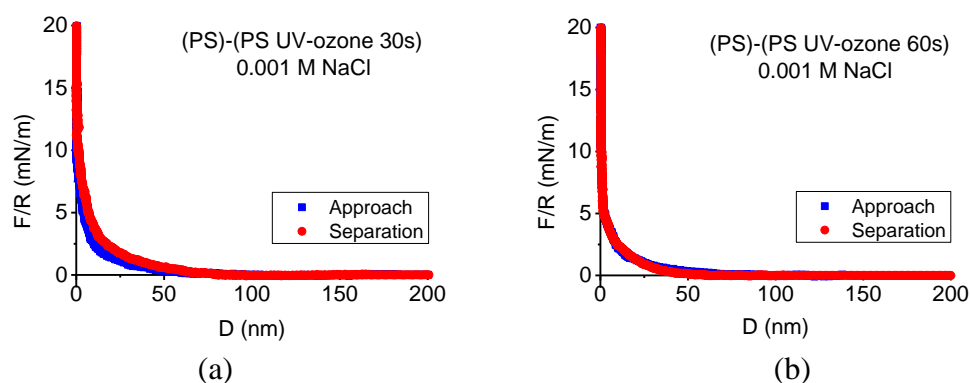
**Figure 3.5** Typical AFM images in air of (a) PS (rms=0.3 nm) and (b) PS treated with UV-ozone for 120 s (rms=0.3 nm).



**Figure 3.6** (a) Normalized XPS spectra of oxygen (O1s), and (b) contact angle of water on PS surface as a function of UV-Ozone treatment time.

The force-distance profiles measured between untreated PS and UV-ozone treated PS surfaces in 0.001 M NaCl solution are shown in Figure 3.7. It is evident from Figure 3.7 that introduction of hydrophilic groups on PS surface through UV-ozone treatment dramatically affects the PS-PS interactions in aqueous solutions in such a way that a long-range attraction between PS-PS surfaces in 0.001 M NaCl (see Figure 2.2) has changed to long-range repulsion. The range of the repulsion is <50 nm for UV-ozone treatment time of 30 s and 60 s (corresponding to static water contact angle of 65° and 50° on treated PS respectively) and increases to >70 nm as treatment time increases to 90 s and 120 s (corresponding to water contact angle of 30° and 15° on treated PS

respectively). Thus the interactions between PS and UV-ozone treated PS surfaces become very similar cases to PS-mica interactions in aqueous solutions (Figure 3.1) as the UV-ozone treated PS surfaces become much more hydrophilic with water contact angle lower than  $30^\circ$ . It is noted that the long-range attraction between PS-PS in Figure 2.2 was mainly due to the presence of air bubbles adsorbed on the opposing hydrophobic polymer surfaces.<sup>13</sup> The change of such long-range attraction in the PS-PS system to pure repulsion between PS and UV-ozone treated PS indicates that there were no significant bubbles on the UV-ozone treated PS. Although various factors can impact the bubble formation on hydrophobic surfaces and the associated mechanisms are still not clear, the results of Figure 3.7 show the important role of surface hydrophobicity on the formation and stability of bubbles on solid surfaces. It is clear from Figure 3.7a that even under UV-ozone treatment of 30s (water contact angle of  $65^\circ$ ), long-range repulsion was observed which suggests that no significant bubbles were formed on the UV-ozone treated PS (otherwise long-range attraction due to the bubble-bubble coalescence should be observed, as report recently).<sup>13</sup>



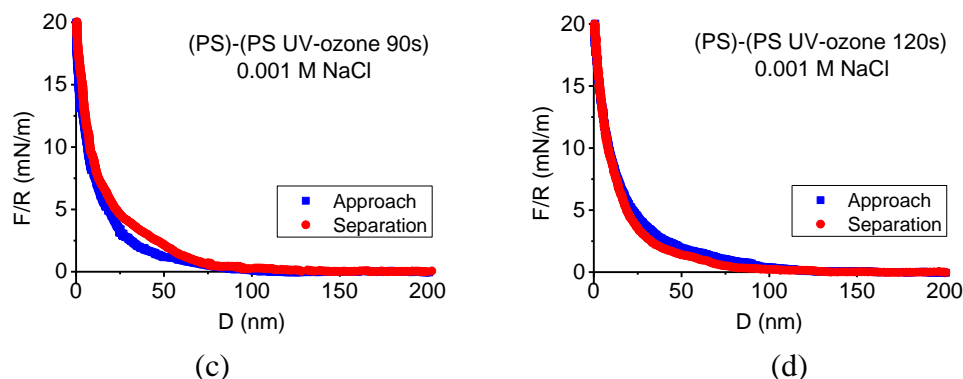


**Figure 3.7** Force-distance profiles of PS vs. UV-Ozone treated PS in 0.001 M NaCl for different UV-Ozone treatment time.

### 3.4 Conclusion

In this work, PS and mica were chosen as a model system to investigate the interaction between hydrophilic and hydrophobic surfaces. The interaction between mica and PS surfaces were directly measured using an SFA coupled with a top-view optical microscope in five different electrolytes (*i.e.*, NaCl, CaCl<sub>2</sub>, NaOH, HCl and CH<sub>3</sub>COOH) with concentration of 0.001 M and 1 M. A long-range repulsion of ~50 to ~100 nm was measured in all the electrolyte solutions at low concentration (*i.e.* 0.001 M) which was mainly due to the presence of microscopic and submicroscopic bubbles formed on the PS surfaces. The range of the repulsion was reduced to <20 nm in NaCl, CaCl<sub>2</sub> and NaOH and did not change significantly in HCl and CH<sub>3</sub>COOH solutions as the electrolyte concentration increased to 1 M, which was related to the formation and stability of bubbles on hydrophobic PS surface due to ion specificity. A modified DLVO theory which takes into account the effect of bubbles on PS surface well fits the experimental interaction force-distance profiles between PS and mica. The range of repulsion was reduced significantly to <20 nm upon

degassing the solution which indicates the important role of dissolved gases on the measured repulsion between PS and mica surfaces. It was also found that the range of repulsion between PS and UV-ozone treated PS gradually increased as the treated PS surface becomes more hydrophilic, which demonstrates the important role of surface hydrophobicity on the formation and stability of bubbles on solid surfaces. It has been shown that DLVO forces dominate the interaction between hydrophilic mica and hydrophobic polymer PS, while the types of electrolytes (ion specificity), concentration of electrolytes, degassing and surface hydrophobicity can all significantly affect the formation and stability of bubbles on the interacting surfaces, thus affecting the range and magnitude of the interaction forces. Our results shed light on the basic interaction mechanism between hydrophilic and hydrophobic surfaces, with implications for many biological and non-biological phenomena such as mineral flotation, protein adsorption, biofilm formation, and self-assembly.

## References

- (1) Israelachvili, J.; Pashley, R. The Hydrophobic Interaction is Long Range, Decaying Exponentially with Distance. *Nature* **1982**, *300*, 341-342.
- (2) Pashley, R. M.; McGuiggan, P. M.; Ninham, B. W.; Evans, D. F. Attractive Forces between Uncharged Hydrophobic Surfaces: Direct Measurements in Aqueous Solution. *Science* **1985**, *229*, 1088-1089.

- (3) Claesson, P. M.; Blom, C. E.; Herder, P. C.; Ninham, B. W. Interactions between Water-Stable Hydrophobic Langmuir -Blodgett Monolayers on Mica. *J. Colloid Interface Sci.* **1986**, *114*, 234-242.
- (4) Christenson, H. K.; Claesson, P. M. Cavitation and the Interaction between Macroscopic Hydrophobic Surfaces. *Science* **1988**, *239*, 390-392.
- (5) Meagher, L.; Craig, V. S. J. Effect of Dissolved Gas and Salt on the Hydrophobic Force between Polypropylene Surfaces. *Langmuir* **1994**, *10*, 2736-2742.
- (6) Parker, J. L.; Claesson, P. M.; Attard, P. Bubbles, Cavities, and the Long-Ranged Attraction between Hydrophobic Surfaces. *J. Phys. Chem.* **1994**, *98*, 8468-8480.
- (7) Considine, R. F.; Hayes, R. A.; Horn, R. G. Forces Measured between Latex Spheres in Aqueous Electrolyte: Non-DLVO Behavior and Sensitivity to Dissolved Gas. *Langmuir* **1999**, *15*, 1657-1659.
- (8) Christenson, H. K.; Claesson, P. M. Direct Measurements of the Force between Hydrophobic Surfaces in Water. *Adv. Colloid Interface Sci.* **2001**, *91*, 391-436.
- (9) Mishchuk, N.; Ralston, J.; Fornasiero, D. Influence of Dissolved Gas on Van Der Waals Forces between Bubbles and Particles. *J. Phys. Chem. A* **2002**, *106*, 689-696.
- (10) Attard, P. Nanobubbles and the Hydrophobic Attraction. *Adv. Colloid Interface Sci.* **2003**, *104*, 75-91.

- (11) Meyer, E. E.; Rosenberg, K. J.; Israelachvili, J. Recent Progress in Understanding Hydrophobic Interactions. *Proc. Natl. Acad. Sci. U. S. A.* **2006**, *103*, 15739-15746.
- (12) Hammer, M. U.; Anderson, T. H.; Chaimovich, A.; Shell, M. S.; Israelachvili, J. The Search for the Hydrophobic Force Law. *Faraday Discuss.* **2010**, *146*, 299-308.
- (13) Faghihnejad, A.; Zeng, H. Hydrophobic Interactions between Polymer Surfaces: Using Polystyrene as a Model System. *Soft Matter* **2012**, *8*, 2746-2759.
- (14) Zhang, X.; Kumar, A.; Scales, P. J. Effects of Solvency and Interfacial Nanobubbles on Surface Forces and Bubble Attachment at Solid Surfaces. *Langmuir* **2011**, *27*, 2484-2491.
- (15) Tyrrell, J. W. G.; Attard, P. Atomic Force Microscope Images of Nanobubbles on a Hydrophobic Surface and Corresponding Force-Separation Data. *Langmuir* **2002**, *18*, 160-167.
- (16) Israelachvili, J. N. In *Intermolecular and Surface Forces*; Academic Press: 2011.
- (17) Zeng, H., Ed.; In *Polymer adhesion, friction and lubrication*; Wiley: 2013.
- (18) Claesson, P. M.; Herder, P. C.; Blom, C. E.; Ninham, B. W. Interactions between a Positively Charged Hydrophobic Surface and a Negatively Charged Bare Mica Surface. *J. Colloid Interface Sci.* **1987**, *118*, 68-79.



- (19) Ducker, W. A.; Xu, Z.; Israelachvili, J. N. Measurements of Hydrophobic and DLVO Forces in Bubble-Surface Interactions in Aqueous Solutions. *Langmuir* **1994**, *10*, 3279-3289.
- (20) Yoon, R.; Flinn, D. H.; Rabinovich, Y. I. Hydrophobic Interactions between Dissimilar Surfaces. *J. Colloid Interface Sci.* **1997**, *185*, 363-370.
- (21) Kokkoli, E.; Zukoski, C. F. Interaction Forces between Hydrophobic and Hydrophilic Self-Assembled Monolayers. *J. Colloid Interface Sci.* **2000**, *230*, 176-180.
- (22) Hoy, O.; Zdyrko, B.; Lupitskyy, R.; Sheparovych, R.; Aulich, D.; Wang, J.; Bittrich, E.; Eichhorn, K.; Uhlmann, P.; Hinrichs, K.; Muller, M.; Stamm, M.; Minko, S.; Luzinov, I. Synthetic Hydrophilic Materials with Tunable Strength and a Range of Hydrophobic Interactions. *Adv. Funct. Mater.* **2010**, *20*, 2240-2247.
- (23) Eriksson, J. C.; Henriksson, U.; Kumpulainen, A. Hydrophobic Attraction Forces in Asymmetric Aqueous Films between Hydrophobized mica/bare Mica Surfaces. *Colloids Surf., A* **2006**, *282*, 79-83.
- (24) Fielden, M. L.; Hayes, R. A.; Ralston, J. Surface and Capillary Forces Affecting Air Bubble-Particle Interactions in Aqueous Electrolyte. *Langmuir* **1996**, *12*, 3721-3727.
- (25) Lee, J. H.; Meredith, J. C. Non-DLVO Silica Interaction Forces in NMP-Water Mixtures II. an Asymmetric System. *Langmuir* **2011**, *27*, 10000-10006.

- (26) Preuss, M.; Butt, H. J. Direct Measurement of Particle-Bubble Interactions in Aqueous Electrolyte: Dependence on Surfactant. *Langmuir* **1998**, *14*, 3164-3174.
- (27) Blake, T. D.; Kitchener, J. A. Stability of Aqueous Films on Hydrophobic Methylated Silica. *J. Chem. Soc., Faraday Trans. 1* **1972**, *68*, 1435-1442.
- (28) Klein, J. Shear, Friction and Lubrication Forces between Polymer-Bearing Surfaces. *Annu. Rev. Mater. Sci.* **1996**, *26*, 581-612.
- (29) Leger, L.; Raphael, E.; Hervet, H. Surface-Anchored Polymer Chains: Their Role in Adhesion and Friction. *Adv. Polym. Sci.* **1999**, *138*, 185-225.
- (30) Creton, C.; Kramer, E. J.; Brown, H. R.; Hui, C. Adhesion and Fracture of Interfaces between Immiscible Polymers: From the Molecular to the Continuum Scale. *Adv. Polym. Sci.* **2002**, *156*, 53-136.
- (31) Maeda, N.; Chen, N.; Tirrell, M.; Israelachvili, J. N. Adhesion and Friction Mechanisms of Polymer-on-Polymer Surfaces. *Science* **2002**, *297*, 379-382.
- (32) Prager, S.; Tirrell, M. The Healing Process at polymer-polymer Interfaces. *J. Chem. Phys.* **1981**, *75*, 5194-5198.
- (33) Zeng, H.; Maeda, N.; Chen, N.; Tirrell, M.; Israelachvili, J. Adhesion and Friction of Polystyrene Surfaces Around T<sub>g</sub>. *Macromolecules* **2006**, *39*, 2350-2363.
- (34) Zeng, H.; Zhao, B.; Tian, Y.; Tirrell, M.; Gary Leala, L.; Israelachvili, J. N. Transient Surface Patterns during Adhesion and Coalescence of Thin Liquid Films. *Soft Matter* **2007**, *3*, 88-93.

- (35) Zeng, H.; Tian, Y.; Zhao, B. X.; Tirrell, M.; Israelachvili, J. Friction at the Liquid/Liquid Interface of Two Immiscible Polymer Films. *Langmuir* **2009**, *25*, 4954-4964.
- (36) Zeng, H.; Zhao, B.; Israelachvili, J. N.; Tirrell, M. Liquid- to Solid-Like Failure Mechanism of Thin Polymer Films at Micro- and Nanoscales. *Macromolecules* **2010**, *43*, 538-542.
- (37) Stocco, A.; Chanana, M.; Su, G.; Cernoch, P.; Binks, B. P.; Wang, D. Bidirectional Nanoparticle Crossing of Oil–Water Interfaces Induced by Different Stimuli: Insight into Phase Transfer. *Angew. Chem. Int. Ed.* **2012**, *51*, 9647-9651.
- (38) Liu, J.; Gao, Y.; Cao, D.; Zhang L.; Guo, Z. Nanoparticle Dispersion and Aggregation in Polymer Nanocomposites: Insights from Molecular Dynamics Simulation. *Langmuir* **2011**, *27*, 7926-7933.
- (39) Craig, V. S. J.; Ninham, B. W.; Pashley, R. M. Study of the Long-Range Hydrophobic Attraction in Concentrated Salt Solutions and its Implications for Electrostatic Models. *Langmuir* **1998**, *14*, 3326-3332.
- (40) Israelachvili, J. N.; Adams, G. E. Measurement of Forces between Two Mica Surfaces in Aqueous Electrolyte Solutions in the Range 0-100 Nm. *J. Chem. Soc., Faraday Trans. 1* **1978**, *74*, 975-1001.
- (41) Israelachvili, J. N.; McGuiggan, P. M. Adhesion and Short-Range Forces between Surfaces. Part I New Apparatus for Surface Force Measurements. *J. Mater. Res.* **1990**, *5*, 2223-2231.

- (42) Israelachvili, J.; Min, Y.; Akbulut, M.; Alig, A.; Carver, G.; Greene, W.; Kristiansen, K.; Meyer, E.; Pesika, N.; Rosenberg, K.; Zeng, H. Recent Advances in the Surface Forces Apparatus (SFA) Technique. *Rep. Prog. Phys.* **2010**, *73*, 1-16.
- (43) Meyer, E. E.; Lin, Q.; Israelachvili, J. N. Effects of Dissolved Gas on the Hydrophobic Attraction between Surfactant-Coated Surfaces. *Langmuir* **2005**, *21*, 256-259.
- (44) Usui, S.; Barouch, E. Effect of Adsorbed Layers on the Van Der Waals Interaction between Particles and Bubbles in Aqueous Media. *J. Colloid Interface Sci.* **1990**, *137*, 281-288.
- (45) Mishchuk, N. A. The Model of Hydrophobic Attraction in the Framework of Classical DLVO Forces. *Adv. Colloid Interface Sci.* **2011**, *168*, 149-166.
- (46) Mishchuk, N.; Ralston, J.; Fornasiero, D. Influence of very Small Bubbles on particle/bubble Heterocoagulation. *J. Colloid Interface Sci.* **2006**, *301*, 168-175.
- (47) Zhang, X. H.; Maeda, N.; Craig, V. S. J. Physical Properties of Nanobubbles on Hydrophobic Surfaces in Water and Aqueous Solutions. *Langmuir* **2006**, *22*, 5025-5035.
- (48) Zhang, X. H.; Quinn, A.; Ducker, W. A. Nanobubbles at the Interface between Water and a Hydrophobic Solid. *Langmuir* **2008**, *24*, 4756-4764.
- (49) Yang, J.; Duan, J.; Fornasiero, D.; Ralston, J. Very Small Bubble Formation at the Solid-Water Interface. *J. Phys. Chem. B* **2003**, *107*, 6139-6147.

- (50) Najafi, A. S.; Drelich, J.; Yeung, A.; Xu, Z.; Masliyah, J. A Novel Method of Measuring Electrophoretic Mobility of Gas Bubbles. *J. Colloid Interface Sci.* **2007**, *308*, 344-350.
- (51) Nakao, A.; Suzuki, Y.; Iwaki, M. Water Wettability and Zeta-Potential of Polystyrene Surface Modified by Ne Or Na Implantation. *J. Colloid Interface Sci.* **1998**, *197*, 257-262.
- (52) Browne, C.; Tabor, R. F.; Chan, D. Y. C.; Dagastine, R. R.; Ashokkumar, M.; Grieser, F. Bubble Coalescence during Acoustic Cavitation in Aqueous Electrolyte Solutions. *Langmuir* **2011**, *27*, 12025-12032.
- (53) Tabor, R. F.; Chan, D. Y. C.; Grieser, F.; Dagastine, R. R. Anomalous Stability of Carbon Dioxide in pH-Controlled Bubble Coalescence. *Angew. Chem., Int. Ed.* **2011**, *50*, 3454-3456.
- (54) Kunz, W., Ed.; In *Specific ion effects*; World Scientific Pub. Co.: Singapore, 2010.
- (55) Craig, V. S. J.; Ninham, B. W.; Pashley, R. M. Effect of Electrolytes on Bubble Coalescence. *Nature* **1993**, *364*, 317-319.
- (56) Jungwirth, P.; Tobias, D. J. Specific Ion Effects at the Air/Water Interface. *Chem. Rev.* **2006**, *106*, 1259-1281.
- (57) Henry, C. L.; Craig, V. S. J. Ion-Specific Influence of Electrolytes on Bubble Coalescence in Nonaqueous Solvents. *Langmuir* **2008**, *24*, 7979-7985.

- (58) Weissenborn, P. K.; Pugh, R. J. Surface Tension of Aqueous Solutions of Electrolytes: Relationship with Ion Hydration, Oxygen Solubility, and Bubble Coalescence. *J. Colloid Interface Sci.* **1996**, *184*, 550-563.
- (59) Wick, C. D.; Dang, L. X. The Behavior of NaOH at the Air-Water Interface: A Computational Study. *J. Chem. Phys.* **2010**, *133*, 024705.
- (60) Lu, Q.; Oh, D. X.; Lee, Y.; Jho, Y.; Hwang, D. S.; Zeng, H. Nanomechanics of Cation- $\pi$  Interactions in Aqueous Solution. *Angew. Chem. Int. Ed.* **2013**, *52*, 3944-3948.
- (61) Mahadevi, A. S.; Sastry, G. N. Cation- $\pi$  Interaction: Its Role and Relevance in Chemistry, Biology, and Material Science. *Chem. Rev.* **2013**, *113*, 2100-2138.
- (62) Debacher, N.; Ottewill, R. H. An Electrokinetic Examination of Mica Surfaces in Aqueous Media. *Colloids Surf.* **1992**, *65*, 51-59.
- (63) Sides, P. J.; Faruqui, D.; Gellman, A. J. Dynamics of Charging of Muscovite Mica: Measurement and Modeling. *Langmuir* **2009**, *25*, 1475-1481.

## **Chapter 4. Adhesion and Surface Interactions of a Self-healing Polymer with Multiple Hydrogen-bonding Groups<sup>4</sup>**

### **4.1 Introduction**

The field of supramolecular chemistry utilizes multiple, reversible, and in certain cases, cooperative intermolecular interactions to create new materials with unique properties and functionalities. The non-covalent intermolecular interactions typically utilized in the design of supramolecular materials and polymers include hydrophobic,<sup>1, 2</sup> hydrogen bonding,<sup>3-8</sup> metal-ligand<sup>9-11</sup> and ionic interactions.<sup>12</sup> Over the last two decades many synthesis strategies have been developed to design new supramolecular polymers with unique characteristics such as enhanced bulk properties (i.e., plateau modulus, tensile modulus), self-healing capability, stimulus-responsiveness and the ability to assemble into well-defined nanostructures.<sup>5-7, 9, 13-19</sup> Self-healing polymer materials or composites have attracted considerable attention over the past decade due to their controllable and reversible molecular interactions, interesting mechanical properties and potential applications.<sup>5, 18</sup> Many conventional healing approaches used in thermoplastic polymers and thermoset composites such as microencapsulation and thermally reversible crosslinks (covalent bonds) require treatments at high temperature (i.e., high energy input). Another widely used method for developing self-healing polymers is by incorporating strong and

---

<sup>4</sup> A version of this chapter has been submitted for publication, *Advanced Functional Materials* (2013).

reversible non-covalent hydrogen bonding moieties into the polymer structure. For example, the 2-ureido-4[1*H*]-pyrimidinone (UPy) group is a strong quadruple-hydrogen-bonding dimer which was first used by Sijbesma et al.<sup>3</sup> to synthesize supramolecular polymers, and has been shown to be highly thermally responsive.<sup>20, 21</sup> In addition, the properties and applications of supramolecular materials are largely determined by the strength of the non-covalent (adhesion) interactions and the interaction kinetics. As a result, understanding the various factors governing the formation of non-covalent bonds and the effects of environment conditions is crucial for the development of advanced functional supramolecular materials. Despite the progress in the development and characterization of supramolecular polymers with various chemical structures, understanding their molecular and surface interaction mechanisms remains limited.

In the present work the surface properties and adhesion mechanisms of a supramolecular self-healing polymer, UPy-functionalized poly(*n*-butyl-acrylate) were investigated by using a surface forces apparatus (SFA) as well as the complementary techniques of atomic force microscopy (AFM), optical microscopy and contact angle goniometry. An SFA coupled with a top-view optical microscope, which has been previously used in the studies of adhesion and friction mechanisms of various polymer surfaces as well as molecular interactions of both biological and non-biological systems,<sup>22-30</sup> was employed to study the contact mechanics and adhesion between self-healing UPy-functionalized poly(*n*-butyl-acrylate) films. The surface deformations and



patterns associated with the adhesion and detachment of these supramolecular polymer films were monitored *in situ* in real time through multiple beam interferometry (MBI) in the SFA as well as the top-view optical microscope, followed by further examination with AFM. Since UPy groups are capable of forming multiple hydrogen bonds, we also investigated the effects of UPy monomer content of the polymers and different environmental conditions such as the relative humidity and temperature on the adhesion and contact behaviour of the polymer surfaces. The self-healing capability of UPy functionalized polymer during adhesion and detachment cycles was also investigated. The surface interaction mechanisms and potential applications of the self-healing polymer will be discussed.

## 4.2 Materials and Methods

Random copolymers of *n*-butyl acrylate backbones with quadruple hydrogen-bonding side chains of 2-ureido-4[1*H*]-pyrimidinone (UPy), Poly (*n*-butyl acrylate-*r*-UPy acrylate) or P(nBA-*r*-UPy), were synthesized and characterized as reported previously.<sup>7</sup> Schematics of the chemical structure of P(nBA-*r*-UPy) and hydrogen bonding between two UPy groups are shown in Figure 4.1.

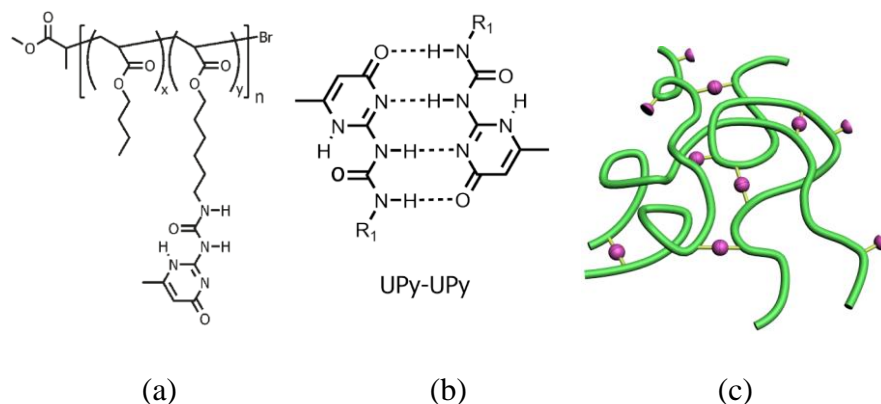


**Figure 4.1** Schematics of (a) the chemical structure of P(nBA-*r*-UPy) and (b) hydrogen bonds between two UPy groups and (c) polymer chains functionalized with UPy groups.

Copolymer solutions were prepared by dissolving the polymers in toluene (Fisher Scientific, Canada, high-performance liquid chromatography (HPLC) grade, 99.9%) that were filtered using 0.2  $\mu\text{m}$  filters before use. P(nBA-*r*-UPy) with repeat units functionalized with two different mole percentages of UPy were studied in this work: 4.0 % UPy and 7.2 % UPy, denoted by PBA-UPy4.0 and PBA-UPy7.2, respectively, with molecular weights  $M_n$  of 24.8 and 25.3  $\text{kg mol}^{-1}$ , and polydispersities of  $\sim 1.3$ .<sup>7</sup> Polymer films were prepared by spin coating of 0.5 wt % polymer solution on mica or silica substrates, and stored overnight ( $>12$  hr) in vacuum to remove the solvent and leave a uniform smooth film of thickness  $\sim 100$  nm. The polymer surfaces were then mounted into the SFA chamber in a crossed-cylinder geometry (each cylinder of radius  $R=2$  cm), which is equivalent to the interaction between a sphere of radius  $R$  and a flat surface, or between two spheres of radius  $2R$ , when the surface separation  $D$  is much smaller than  $R$  ( $R \gg D$ ). The polymer film thickness in each case was

measured using multiple beam interferometry (MBI) in the SFA by using fringes of equal chromatic order (FECO), and confirmed by ellipsometry.<sup>31</sup>

X-ray photoelectron spectroscopy (XPS) and contact angle measurements were also conducted to characterize the properties of the polymer surfaces. The contact angles of three probe liquids of known surface tensions (water, ethylene glycol and diiodomethane) on the polymer films were measured using a Ramé-Hart contact angle goniometer to estimate the surface energies of the P(nBA-*r*-UPyA) polymers based on the method developed by van Oss et al.<sup>32</sup>

An SFA was used to investigate the adhesion and contact mechanics of the polymer films under different conditions. Details of the SFA experimental setup have been reported previously.<sup>33-35</sup> A top-view optical microscope was coupled with the SFA, as reported previously,<sup>25-27, 36</sup> to observe the surface patterns associated with the adhesion and detachment of the polymer films. The SFA experiments were performed at two relative humidities (RH) of RH=0% (dry condition) and RH=100% (saturated water vapour condition) and two different temperatures of  $T=23\text{ }^{\circ}\text{C}$  (room temperature) and  $T=40\text{ }^{\circ}\text{C}$ . The temperature of the SFA chamber was increased by inserting two heating rods into the walls of the SFA and the temperature was monitored by a thermistor. The surfaces were mounted in the SFA chamber one hour prior to each experiment in order to reach equilibrium under the desired temperature and humidity level. The surface features of the adhesive junctions of the polymer films after the adhesion tests were characterized by an optical microscope (Axioskop 40, Carl Zeiss,

Germany) and an atomic force microscope (AFM) (Asylum, MFP-3D-Bio, Santa Barbara, CA, USA).

### 4.3 Results and discussion

#### 4.3.1 Characterization of the polymer thin films and their surfaces

Typical AFM images of PBA-UPy4.0 and PBA-UPy7.2 thin films in dry air and after exposure to humid air for 1 hr are shown in Figure S1. Figure S1 shows that both polymer films are smooth, with rms roughnesses of 0.3 nm and 0.2 nm for PBA-UPy4.0 and PBA-UPy7.2 films, respectively, and that relative humidity does not have a significant effect on the morphology of the films at room temperature. The XPS spectra of nitrogen (N1s) for the two types of polymer films are shown in Figure S2. The nitrogen peak intensity is proportional to the amount of the UPy groups present on the polymer surface. As expected, Figure S2 confirms that higher amount of UPy groups are present on PBA-UPy7.2 surface than polymer PBA-UPy4.0.

The contact angles of three probe liquids (i.e., ethylene glycol, diiodomethane and water) on the polymer surfaces as a function of time are shown in Figure 4.2. The surface energy of the polymers was determined using the method developed by van Oss et al.<sup>32</sup> as follows. In general, when a droplet of liquid **2** forms a contact angle  $\theta$  on a surface of material **1** in medium **3**, the interfacial energies are related by Young's equation:

$$\gamma_{12} + \gamma_{23} \cos \theta = \gamma_{13} \quad (4.1)$$

If medium **3** is air, Equation 4.1 reduces to

$$\gamma_{12} + \gamma_2 \cos \theta = \gamma_1. \quad (4.2)$$

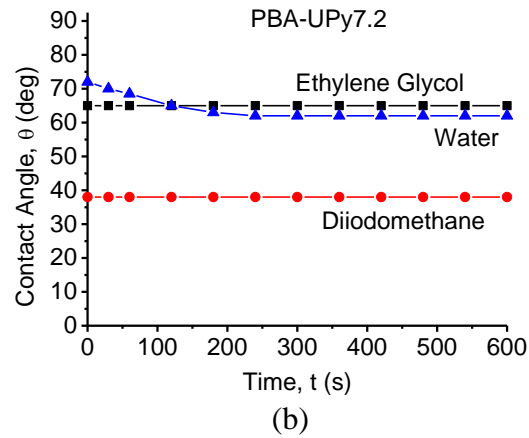
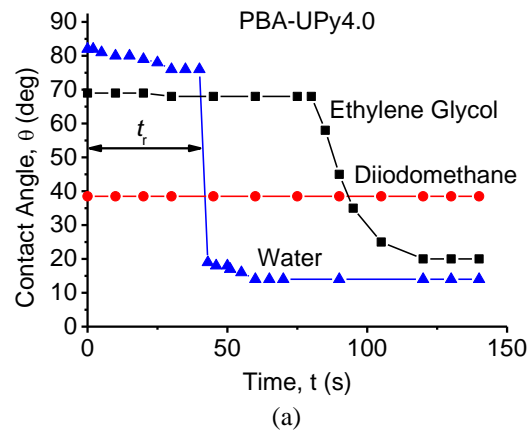


**Figure 4.2** Contact angles of three liquids on the polymer films of (a) PBA-UPy4.0 and (b) PBA-UPy7.2 of thickness 120 nm vs. time,  $t$ . PBA-UPy4.0 film became ruptured after contacting with water for time  $t_r$ , so-called rupture time.

According to the van Oss method the surface energy is comprised of two terms which take into account the contributions from Lifshitz-van der Waals ( $\gamma^{LW}$ ) and Lewis acid-base ( $\gamma^{AB}$ ) interactions as

$$\gamma = \gamma^{LW} + \gamma^{AB}. \quad (4.3)$$

The Lewis acid-base component of the surface energy is defined such that it comprises the electron-acceptor and electron-donor interactions given by

$$\gamma^{AB} = 2\sqrt{\gamma^+\gamma^-}. \quad (4.4)$$

Based on Equation 4.3 and 4.4, Young's equation can be written as

$$\gamma_2 (\cos \theta + 1) = 2 \left( \sqrt{\gamma_1^{LW} \gamma_2^{LW}} + \sqrt{\gamma_1^+ \gamma_2^-} + \sqrt{\gamma_1^- \gamma_2^+} \right). \quad (4.5)$$

By measuring the contact angle of three probe liquids and using the above equations, one can determine the Lifshitz-van der Waals and the acid-base components of the surface energy of polymers.<sup>37, 38</sup> The initial values at  $t=0$  of the contact angles in Figure 4.2 were used in the calculations of the surface energies of the PBA-UPy polymers. The surface energies  $\gamma$  of the polymers as estimated from the contact angle measurements and the above equations are summarized in Table 4.1.

**Table 4.1** Surface energy components of the three probe liquids<sup>39</sup> and the two polymers PBA-UPy4.0 and PBA-UPy7.2 in ( $\text{mJ m}^{-2}$ ) estimated from the initial contact angles (Figure 4.2) using Equation 4.1 to 4.5.

Material	$\gamma$	$\gamma^{LW}$	$\gamma^{AB}$	$\gamma^+$	$\gamma^-$
Diiodomethane	50.8	50.8	$\approx 0$	$\approx 0.01$	$\approx 0$
Ethylene glycol	48	29	19	3.0	30.1
Water	72.8	21.8	51	25.5	25.5
Polymer PBA-UPy4.0	51	40	11	2	15
Polymer PBA-UPy7.2	57	40	17	3	27

From Table 4.1, the surface energies of PBA-UPy4.0 and PBA-UPy7.2 were estimated to be  $\gamma=51$  and  $57 \text{ mJ m}^{-2}$ , respectively, which are much higher than the reported value of  $\gamma=33.7 \text{ mJ m}^{-2}$  for non-functionalized poly(*n*-butylacrylate) (PBA) at  $20^\circ\text{C}$ .<sup>39</sup> The enhanced surface energy of PBA-UPy is mainly due to the effect of hydrogen bonding among the UPy groups in increasing the

polar contributions of the surface energy, as  $\gamma^{AB}=11.2$  and  $16.8 \text{ mJ m}^{-2}$  for PBA-UPy4.0 and PBA-UPy7.2, respectively.

Figure 4.2a shows that the water contact angle on polymer PBA-UPy4.0 surface first dropped from  $82^\circ$  to  $76^\circ$  in  $t_r \sim 40$  seconds and then dropped abruptly which was coupled with the rupture of thin polymer film. Similar rupture behavior occurred for ethylene glycol on PBA-UPy4.0 film after  $t_r \sim 85$  seconds. The typical rupture patterns are shown in Figure S3. The effect of film thickness on the rupture time  $t_r$  and the possible rupture mechanism are discussed in Figure S4 and S5. Figure 4.2b shows that contact angles of the three probe liquids were stable on the polymer PBA-UPy7.2 surface and only the water contact angle slightly decreases from  $72^\circ$  to  $62^\circ$  after  $\sim 5$  minutes. The decrease of water contact angle ( $t < t_r$ , before rupture) is attributed to the overturning of the UPy segments and hydrogen bond formation between the UPy groups and water molecules on the polymer surface, which agrees with the increased  $\gamma$  values ( $\gamma=57$  and  $69 \text{ mJ m}^{-2}$  for PBA-UPy4.0 and PBA-UPy7.2, respectively) as estimated by using the decreased water contact angles.

#### **4.3.2 Contact and adhesion mechanics of polymer thin films: effects of relative humidity, temperature and time**

Contact mechanics tests<sup>22, 40</sup> were conducted to investigate the adhesion of the PBA-UPy4.0 and PBA-UPy7.2 films at  $T=23$  and  $40^\circ\text{C}$ . The classical theory of contact mechanics of surfaces was first studied by Hertz in 1888<sup>41</sup> and followed by Johnson, Kendall and Roberts (JKR model), Derjaguin, Muller and Toporov

(DMT model), and Maugis.<sup>42-44</sup> In general for soft materials of large radius with high surface energy (e.g., polymers) the JKR model is more applicable, while for hard materials of low surface energy and small radius of curvature the DMT model is more appropriate.<sup>38, 40</sup> According to the JKR model, for two *elastic* surfaces with surface energy  $\gamma$  under an external load  $F_{\perp}$ , the radius of the contact area  $a$  is given by

$$a^3 = \frac{R}{K} \left( F_{\perp} + 6\pi R\gamma + \sqrt{12\pi R\gamma F_{\perp} + (6\pi R\gamma)^2} \right), \quad (4.6)$$

where  $R$  is the radius of an elastic sphere pressed against a flat surface which is equivalent to two perpendicular cylinders of radius  $R$  based on Derjaguin approximation,  $K$  is the equivalent modulus, related to Young's moduli  $E$  and the Poisson ratios  $\nu$  by  $K=2E/3(1-\nu^2)$ .<sup>29</sup> The corresponding adhesion or pull-off force is given by

$$F_{\perp}^{\text{ad}} = 3\pi R\gamma. \quad (4.7)$$

The contact diameter  $2a$  as a function of applied load  $F_{\perp}$  during loading and unloading of PBA-UPy4.0 and PBA-UPy7.2 at  $T=23$  and  $40$  °C under two different relative humidity levels of  $\text{RH}=0\%$  and  $\text{RH}=100\%$  are shown in Figure 4.3a-d. The adhesion forces (or pull-off forces) and corresponding effective surface energies  $\gamma_{\text{eff}} (=F_{\perp}^{\text{ad}}/3\pi R)$ <sup>24, 38</sup> are summarized in Figure 4.3e. The loading and unloading rates were  $k_{\perp}V_{\perp}=0.3 \text{ mN s}^{-1}$  and  $k_{\perp}$  is the stiffness of the force measuring spring (corresponding to separation velocity  $V_{\perp}=0.33 \text{ }\mu\text{m s}^{-1}$ ). The waiting time at the maximum load  $F_{\perp,\text{max}} \approx 33 \text{ mN}$  was fixed at 15 s.



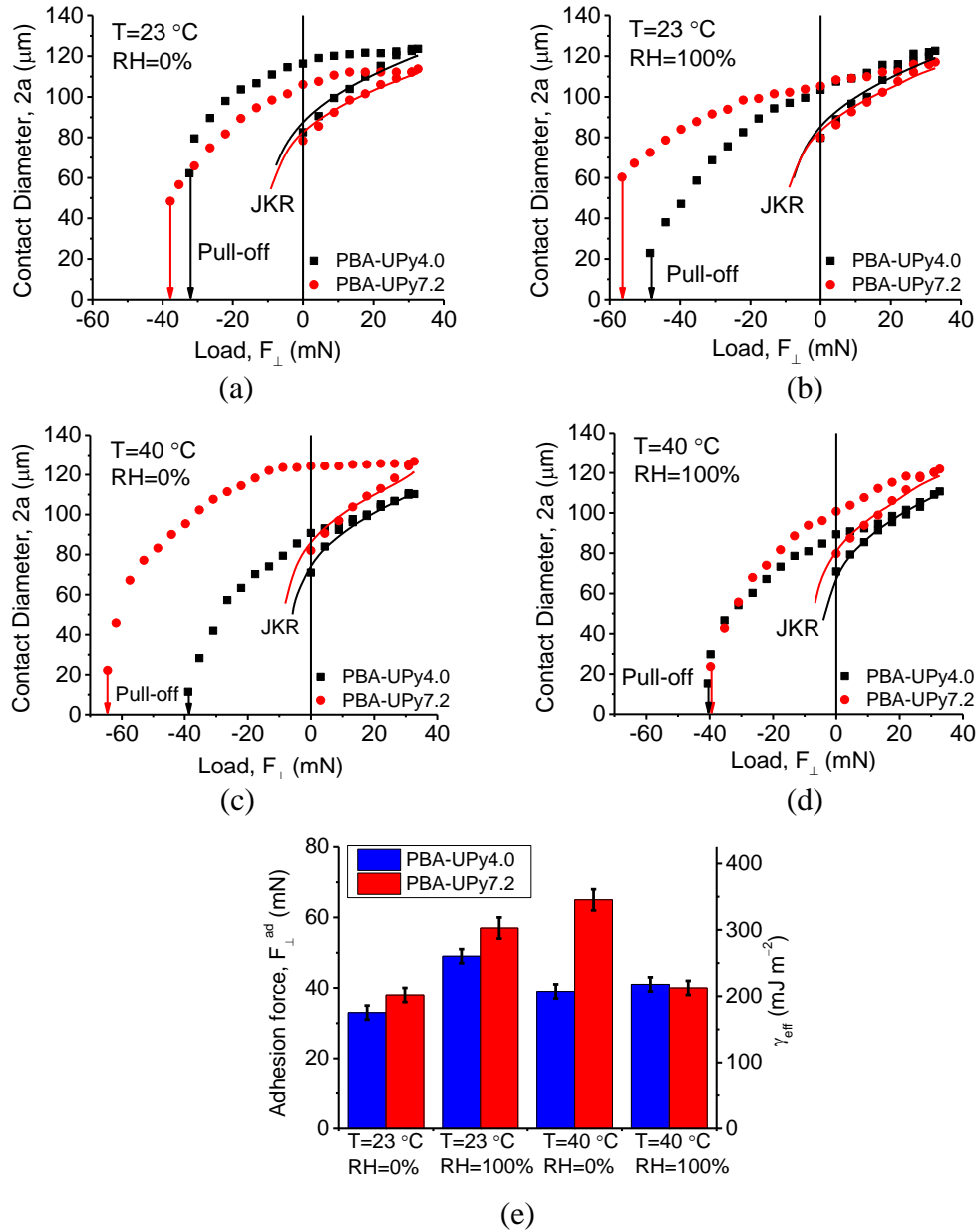


**Figure 4.3** Contact diameter vs. applied load for (a,c) PBA-UPy4.0, (b,d) PBA-UPy7.2 polymer films (thickness  $\sim 100$  nm) at (a,b) room temperature ( $T=23^{\circ}\text{C}$ ) and (c,d)  $T=40^{\circ}\text{C}$  and two relative humidity levels of  $\text{RH}=0\%$  and  $\text{RH}=100\%$ . (e) Summary of adhesion forces and effective surface energies of PBA-UPy polymers at different experiment conditions. Loading and unloading rates were  $k_{\perp}V_{\perp}=0.3$  mN  $\text{s}^{-1}$  or  $V_{\perp}=0.33$   $\mu\text{m s}^{-1}$  and waiting time at the maximum load  $F_{\perp,\text{max}}=33$  mN was 15 s.

As shown in Figure 4.3, hysteresis was observed for the loading and unloading paths under all the conditions tested above, and both relative humidity and

temperature show significant impact on the adhesion behavior of both copolymers. For example, at  $T=23\text{ }^{\circ}\text{C}$  and  $\text{RH}=0\%$ , the adhesion for PBA-UPy4.0 and PBA-UPy7.2 were  $F_{\perp}^{\text{ad}} \approx 33$  and  $38\text{ mN}$ , corresponding to  $\gamma_{\text{eff}}=170$  and  $202\text{ mJ m}^{-2}$  as shown in Figure 4.3a and 4.3e. When the relative humidity was increased to  $\text{RH}=100\%$  at  $T=23\text{ }^{\circ}\text{C}$ , the adhesion forces increased to  $F_{\perp}^{\text{ad}} \approx 49$  and  $57\text{ mN}$ , corresponding to  $\gamma_{\text{eff}}=260$  and  $302\text{ mJ m}^{-2}$  respectively, as shown in Figure 4.3b and 4.3e.

Although significant adhesion hysteresis was measured during unloading, the contact behavior during loading of the PBA-UPy polymers still roughly follows the predictions of the JKR model, as shown by the solid lines in Figure 4.3 and also reported for other polymer systems.<sup>22, 24, 25, 38, 45</sup> The fitted surface energies of the two polymers on loading under different experimental conditions are tabulated in Table 4.2.

**Table 4.2.** Surface energies of polymers PBA-UPy4.0 and PBA-UPy7.2 in  $\text{mJ m}^{-2}$  estimated from JKR fitting of the loading curves in contact mechanics tests (Figure 4.3).

Polymer	T=23 °C		T=40 °C	
	RH=0%	RH=100%	RH=0%	RH=100%
PBA-UPy4.0	45±3	42±2	31±3	26±3
PBA-UPy7.2	49±2	50±3	43±3	36±2

In general, the surface energies in Table 4.2 were close to the values in Table 4.1 that were calculated based on the initial contact angles measurements, for example PBA-UPy4.0 (JKR vs. contact angle method:  $\gamma \approx 45$  vs.  $51\text{ mJ m}^{-2}$ ) and PBA-UPy7.2 ( $\gamma \approx 49$  vs.  $57\text{ mJ m}^{-2}$ ) at room temperature. The difference

between the values obtained from the two methods could be due to several possible factors: the selection of probe liquids in contact angle measurements, and the partial elastic nature of the polymers. As the polymers become liquid-like, the presence of UPy groups play a minor role in the adhesion, and the surface energy values are closer to the value  $\gamma_0$  for poly(n-butyl acrylate) of  $\gamma_0 \sim 31\text{--}34 \text{ mJ m}^{-2}$ .<sup>39, 46</sup>

A higher adhesion force was measured for PBA-UPy7.2 than PBA-UPy4.0 for almost all the above cases (except at RH=100% and  $T=40^\circ\text{C}$ , discussed later), which is attributed to the higher amount of UPy groups for the PBA-UPy7.2 chains and at the polymer/dry air interface as confirmed by XPS (see supporting information). The UPy groups at the opposing polymer surfaces could form multiple hydrogen bonds during contact, enhancing the polymer adhesion. Exposing the polymer films to air at 100% relative humidity for 1 hr could increase the density of UPy functional groups on the polymer surfaces and led to an increase in the adhesion force. It is noted that the water contact angle on polymer PBA-UPy7.2 decreased by about 10 degrees after a few minutes due to the overturning of polar UPy groups at the polymer/air interface. Recent theoretical analysis shows that UPy-UPy binding energy can be reduced from  $\sim -161 \text{ kJ mol}^{-1}$  in vacuum to  $-69 \text{ kJ mol}^{-1}$  in water and that the binding energy of interaction between UPy and water molecules is competitive with that of UPy-UPy.<sup>47</sup> Temperature was also shown to have a significant impact on the adhesion of PBA-UPy polymers. Increasing  $T=23^\circ\text{C}$  to  $40^\circ\text{C}$  at RH=0% leads to an increase in the adhesion forces for both PBA-UPy4.0 and PBA-UPy7.1, which

is attributed to enhanced interpenetration of polymer chains across the contact interface at 40 °C as a result of increased mobility of polymer chains.<sup>22-24</sup>

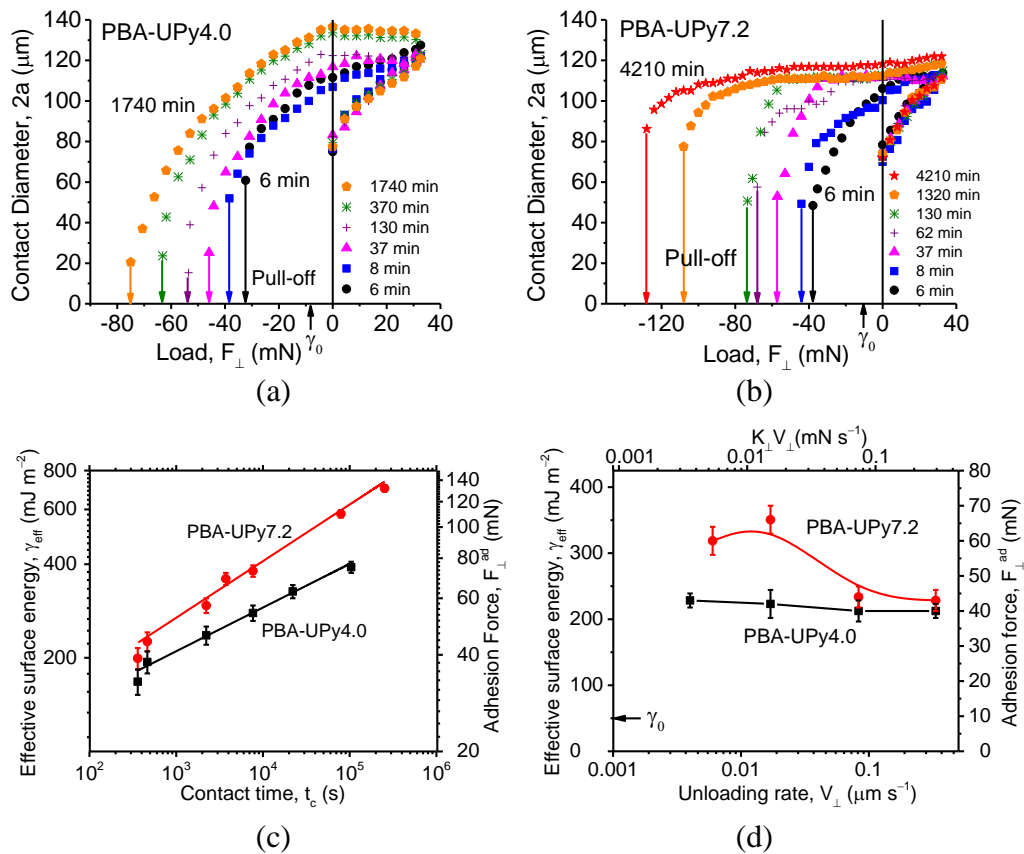
The above results show that the adhesion of PBA-UPy4.0 and PBA-UPy7.2 are affected mainly by the viscoelastic properties of the polymer films, the surface density of UPy groups, as well as the degree of interpenetration of polymer chains across the contact interface and temperature, rate and time (discussed later). The experimental temperatures were higher than the glass transition temperatures of PBA-UPy4.0 and PBA-UPy7.2, and the adhesion hysteresis and the contact behaviors (as also discussed later) indicate that both polymers behave viscoelastically.<sup>7</sup> As the relative humidity increases, water molecules interact with the free UPy functional groups on the polymer surface, and may also diffuse into the bulk of the polymer film, thus changing both the surface energy and the viscoelastic properties of polymer film, which is supported by the contact mechanics data of PBA-UPy4.0 at RH=0% and 100%, T=23 °C, as shown in Figure 4.3a and 4.3b (viz. the contact diameter right before pull-off was much smaller at RH=100% compared to that at RH=0%, therefore the polymer film was more liquid-like). It should be noted that the water-UPy interaction has to compete with the UPy-UPy interaction which involves four hydrogen bonds (see Figure 4.1). The higher  $T_g$ , longer effective bond lifetime  $\tau_b^*$  ( $\sim 3$  vs.  $\sim 20$  s)<sup>7</sup>, less mobility of the chains and stronger interaction of the higher amount of UPy groups make the PBA-UPy7.2 polymer more elastic<sup>7</sup> and the diffusion of water molecules in the PBA-UPy7.2 film would be *relatively* more difficult than that for the PBA-UPy4.0 case.<sup>48-52</sup> Increasing the relative

humidity also dramatically increases the density of free UPy functional groups on the surface,<sup>47</sup> and this effect is relatively more significant for PBA-UPy7.2 than for PBA-UPy4.0. The overall effect of relative humidity on the *bulk* viscoelastic properties (e.g.,  $G'$ ,  $G''$ ) and *surface* chemistry ( $\gamma$  values) of the two PBA-UPy polymers, is to increase their adhesion by ~50% when increasing the relative humidity from 0% to 100% at room temperature.

As shown in Figure 4.3e, on increasing the temperature from 23 to 40 °C at RH=0%, the adhesion of PBA-UPy4.0 and PBA-UPy7.2 increased by ~20% and ~70%, respectively. Increasing the relative humidity further to 100% at 40 °C has almost no effect on the adhesion of PBA-UPy4.0 while it decreases the adhesion of PBA-UPy7.2 to be the same value as PBA-UPy4.0. These results suggests that for PBA-UPy4.0, the UPy-UPy hydrogen bonds can easily form and break at 40 °C, and that the bulk properties dominate the polymer adhesion – the polymer essentially behaves like a viscous liquid, which was further supported by the viscous fingering phenomena associated with the detachment process similar to those shown later in Figure 4.6. For PBA-UPy7.2, increasing the temperature from 23 to 40 °C at RH=0% could further increase the interpenetration of polymer chains at the contact interface and form multiple UPy-UPy bonds, and PBA-UPy7.2 still behaves like a soft elastic solid as supported by the contact behavior (enhanced adhesion) and fracture patterns associated with the adhesion tests shown in Figure 4.5 (discussed later). When the relative humidity was further increased to 100% at 40 °C, PBA-UPy7.2 now

behaves more like a viscous liquid, and viscous fingering patterns were observed during the detachment process as shown in Figure 4.6 (discussed later).

It was observed that the contact time also plays an important role in the adhesion of the PBA-UPy polymers. To investigate the effect of total contact time,  $t_c$ , the polymer surfaces were kept in contact at the maximum load ( $F_{\perp, \max} \approx 33$  mN) for different times before separation, and the total contact time  $t_c$  is defined as the total time from first contact to final detachment. The effect of total contact time and unloading rate on the measured adhesion of PBA-UPy4.0 and PBA-UPy7.2 at room temperature is shown in Figure 4.4. The corresponding adhesion force is converted to the effective surface energy  $\gamma_{\text{eff}}$  by Equation 4.7.<sup>24, 38, 45</sup>



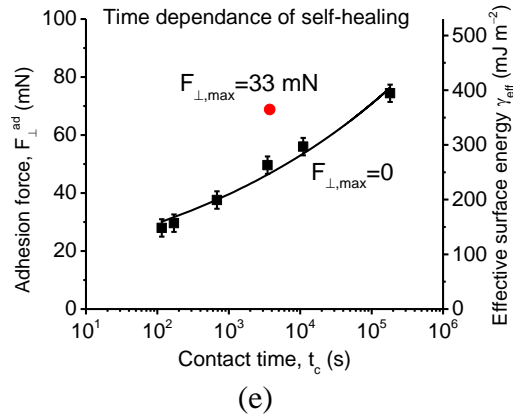


**Figure 4.4** Contact diameter vs. external load during JKR tests under different contact time for (a) PBA-UPy4.0 and (b) PBA-UPy7.2 polymer films of thickness  $\sim 100$  nm at room temperature, (c) the adhesion force measured vs. total contact time and (d) the adhesion force vs. unloading rate. Note that the unloading rate was  $k_{\perp}V_{\perp}=0.3 \text{ mN s}^{-1}$  or  $V_{\perp}=0.33 \text{ }\mu\text{m s}^{-1}$  for (a)–(c). (e) The effect of total contact time on the self-healing adhesion between two PBA-UPy7.2 films of thickness 107 nm under zero pre-loading condition ( $F_{\perp,\text{max}}=0$ ). The red data point shows the initial adhesion of the polymer films (for  $F_{\perp,\text{max}}=33 \text{ mN}$  and  $t_c \sim 3700 \text{ s}$ ).

Figure 4.4 shows that the effective adhesion of both PBA-UPy4.0 and PBA-UPy7.2 increase dramatically with  $t_c$  as

$$\gamma_{\text{eff}} \propto F_{\perp}^{\text{ad}} \propto t_c^n, \quad (4.8)$$

where  $n=0.13 \pm 0.01$  and  $0.18 \pm 0.01$  for PBA-UPy4.0 and PBA-UPy7.2, respectively. The increase of the adhesion with total contact time is mainly due to the formation of more UPy-UPy H-bonds (Figure 4.1) across the interface with time. As expected, the higher density of UPy groups on the PBA-UPy7.2 surfaces lead to a faster increase of the adhesion with contact time compared to PBA-UPy4.0, as shown in Figure 4.4. It is interesting to note in Figure 4.4a and 4.4b that with increasing contact time, the contact area ( $\pi a^2$ ) remained constant during the initial stage of separation. The constant contact area phenomenon was more pronounced for PBA-UPy7.2 at long contact times ( $t_c > 2 \text{ hrs}$ ), shown in

Figure 4.4b; the contact area only decreased at high negative loads close to detachment.

If the surfaces are kept in contact for a sufficiently long time the two surfaces totally coalesce and the contact interface is expected to “disappear”. In this limit we expect tensile failure to occur and the tensile failure strength would be obtained. For example when  $t_c \sim 2.5 \times 10^5 \text{ s}$ ,  $F_{\perp}^{\text{ad}} \sim 130 \text{ mN}$ ,  $\gamma_{\text{eff}} \approx 700 \text{ mJ m}^{-2}$ , and the contact diameter  $2a \sim 120 \text{ }\mu\text{m}$ , so that the tensile strength of the submicroscopic adhesive junction (or confined thin film) of PBA-UPy7.2 can be estimated to be at least  $\sigma_c = F_{\perp}^{\text{ad}} / \pi a^2 \sim 11 \text{ MPa}$ . Similarly, the minimum tensile strength of the submicroscopic adhesive junction of PBA-UPy4.0 is estimated to be  $\sigma_c \sim 4.8 \text{ MPa}$ . These tensile strengths (for the submicroscopic adhesive junctions of thickness  $\sim 200 \text{ nm}$ ) are much higher than reported values for the bulk tensile failure strengths of PBA-UPy polymers in the dogbone geometry (specimens of width  $\sim 1 \text{ cm}$  and thickness  $\sim 0.2 \text{ cm}$ ),<sup>53</sup> which gave  $\sim 1.7 \text{ MPa}$  and  $< 0.5 \text{ MPa}$  for PBA-UPy7.2 and PBA-UPy4.0, respectively. The results here on the enhanced tensile failure strengths of *confined* thin film of multiple hydrogen-bonded PBA-UPy polymers are consistent with our recent report on confined submicroscopic thin films of glassy polystyrene.<sup>28</sup>

The effect of unloading rate on the adhesion force and the corresponding effective surface energy is shown in Figure 4.4d, in which the surfaces were kept in contact under  $F_{\perp, \text{max}} \approx 33 \text{ mN}$  for 240 s. Figure 4.4d shows that with decreasing the unloading rate from  $V_{\perp} = \sim 0.33$  to  $\sim 0.004 \text{ }\mu\text{m s}^{-1}$  the adhesion force almost



keeps constant for PBA-UPy4.0 while slightly increases for PBA-UPy 7.2. The adhesion measured largely depends on the UPy-UPy H-bond life time,<sup>7</sup> debonding rate (related to the unloading rate), and enhanced surface density of UPy groups at the contact interface (related to the total contact time). It should be noted that during the measurements of Figure 4.4d, the total contact time  $t_c$  was actually different under the distinct unloading rates (the slower the unloading rate, the longer the total contact time). Therefore, the different trends measured between PBA-UPy4.0 and PBA-UPy 7.2 in Figure 4.4d are mainly attributed to the change in total contact time. Nevertheless, the effective surface energies measured in Figure 4.4d are much higher than the thermodynamic equilibrium value  $\gamma_0$ , which indicates that a much lower unloading rate would be needed to measure  $\gamma_0$ .

In summary, the contact and adhesion mechanics measurements of the two PBA-UPy polymer films show that their adhesive properties are determined by the surface density of H-bonding groups/segments that can interpenetrate across the contacting interface, and the bulk viscoelasticity of the polymer that determines its viscous forces, consistent with previous studies on polymer-polymer adhesion of uncrosslinked homopolymers.<sup>22, 24, 38, 45</sup> The presence of UPy functional groups can dramatically enhance the polymer adhesion mainly due to the formation of multiple hydrogen bonds across the contact interface. The adhesion of PBA-UPy polymers can be significantly affected by temperature, humidity, unloading rate and contact time.

### 4.3.3 Self-healing of multiple hydrogen-bonding PBA-UPy polymer

One of the more interesting aspects of multiple hydrogen-bonding polymers is their self-healing properties. The self-healing ability of PBA-UPy<sup>7.2</sup> was investigated as follows: two previously fractured films of the polymer were brought back into contact for different contact times at RH=0%. Each set of self-healing experiments was conducted at the same fractured position of the polymer films. The adhesion recovery of the surfaces under different contact times is shown in Figure 4.4e with the initial measured adhesion (under  $F_{\perp, \max} = 33$  mN and  $t_c \sim 3700$  s) shown by the red data point. Figure 4.4e shows that the adhesion recovered to more than 40% of the original value in  $\sim 10$  seconds (viz., the time for surfaces in contact before separation), and to  $\sim 81\%$  in 3 hrs, and continued to recover with time, reaching  $\sim 108\%$  of the original adhesion after  $\sim 50$  hrs of contact. It should be noted that the self-healing tests in Figure 4.4e were all under zero external load (viz., the force measuring spring was brought to the same position as the zero load condition for the first measurement,<sup>34</sup> as illustrated in Figure 4.5a). It is also noted that the self-healing process could be further expedited under a finite external load which presumably enhances the intimate contact of the two fractured surfaces.<sup>5</sup> The adhesion results in Figure 4.4e indicate that PBA-UPy polymer has excellent self-healing ability, which is mainly attributed to the reversible multiple hydrogen bonding of opposing UPy groups between PBA-UPy surfaces.

#### 4.3.4 Characterization of surface patterns associated with adhesion tests

As mentioned earlier, various types of surface deformations and patterns were observed during the adhesion tests of viscoelastic PBA-UPy polymers. Classic theories of contact and adhesion mechanics deal with the adhesion of two purely *elastic* materials and are static (equilibrium) models that describe the mechanical equilibrium states of the materials in contact. The adhesion of viscous and viscoelastic materials involves the dynamic growth of the adhesive junction and transient surface patterns during adhesive contact or “coalescence” as well as during detachment that cannot be described by classic theories. Molecular diffusion (interpenetration) across the interface alters the adhesion energy with time, which is also not included in the JKR theory that assumes  $\gamma=\text{constant}$ . Experimental and theoretical works have been conducted on the contact and adhesion *dynamics* of viscoelastic and viscous materials and polymers to study these complex transient patterns, although a unified theory is still not available.<sup>24-28, 54-61</sup>

The FECO patterns and corresponding top-view optical microscope images during four different stages in contact mechanics experiments of PBA-UPy7.2 at  $T=40\text{ }^{\circ}\text{C}$  and  $\text{RH}=0$  and  $100\%$  are shown in Figure 4.5 and 4.6, respectively: (a) the instant after the polymer surfaces came into adhesive contact ( $F_{\perp}=0$ ), (b) contact under the maximum compressive load ( $F_{\perp}=F_{\text{max}}$ ), (c) the instant just before pull-off or detachment, and (d) after detachment.

PBA-UPy7.2, RH=0

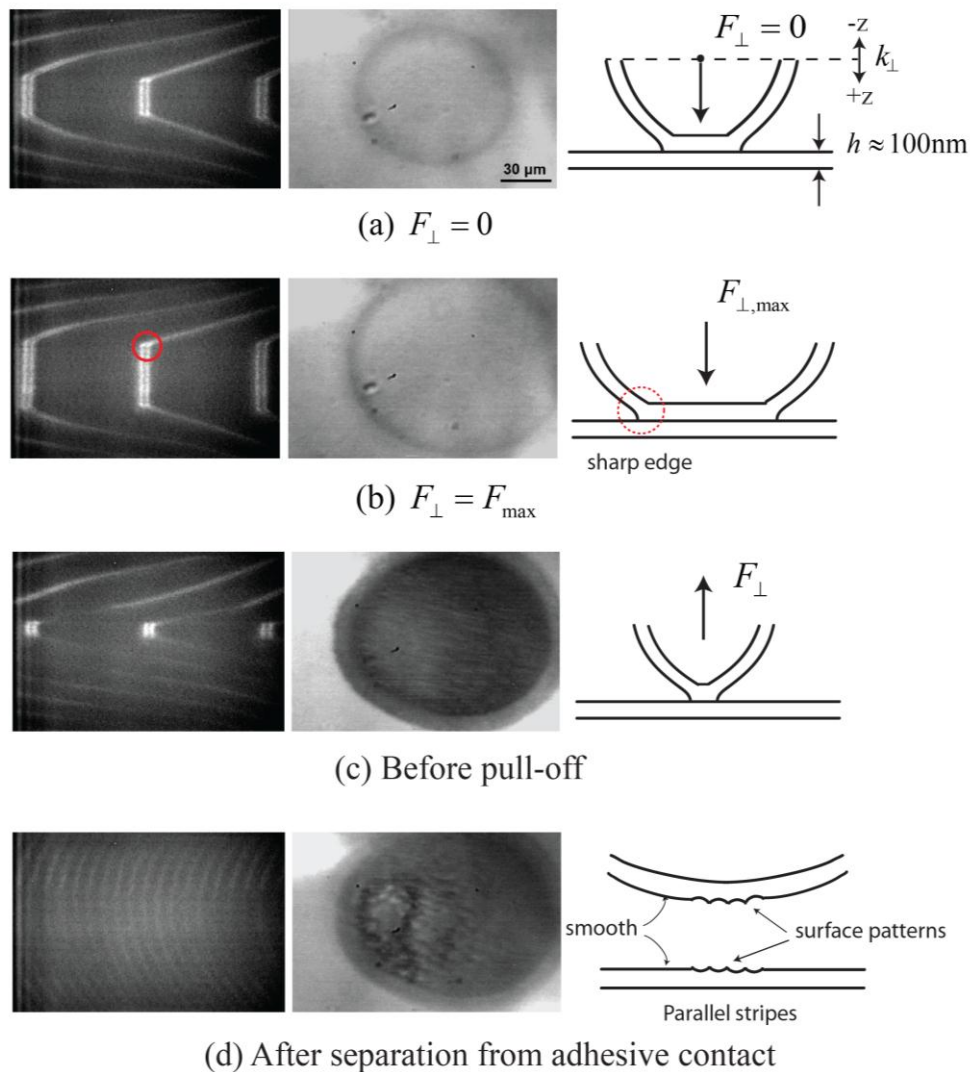


**Figure 4.5** FECD fringe patterns (left), corresponding top-view optical microscope images (middle) and illustrations (right) of the contact junction of PBA-UPy7.2 polymer of thickness 100 nm at  $T=40\text{ }^{\circ}\text{C}$  and  $\text{RH}=0\%$ . Illustration in (a) shows that one surface is supported by a force measuring spring with stiffness  $k_{\perp}$  which can drive the surface close to or away from the opposing surface.

PBA-UPy7.2, RH=100%

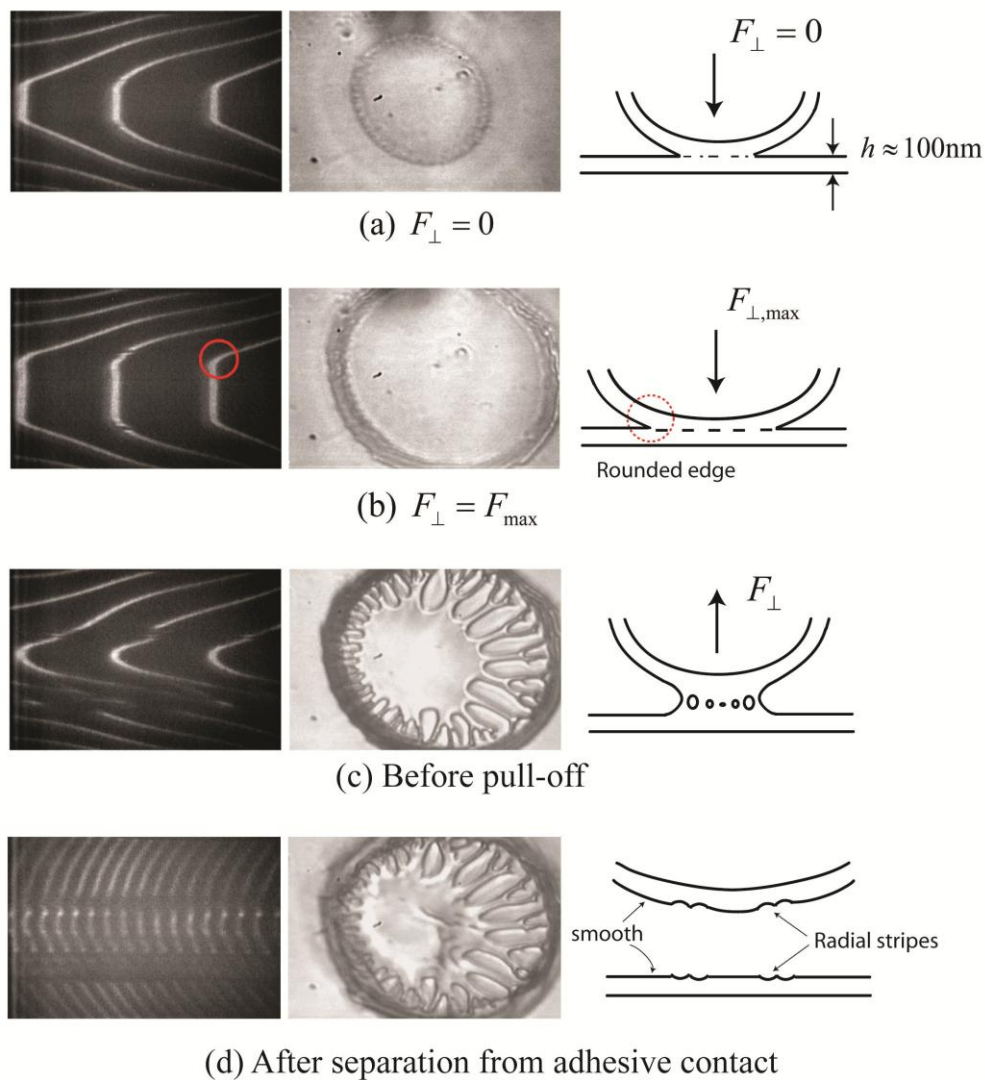


**Figure 4.6** FECO fringe patterns (left), corresponding top-view optical microscope images (middle) and illustrations (right) of the contact junction of PBA-UPy7.2 polymer of thickness 100 nm at  $T=40\text{ }^{\circ}\text{C}$  and  $\text{RH}=100\%$ .

We may note the sharp contact edge in the FECO patterns in Figure 4.5b compared to the “rounded” (or meniscus-like) contact edge in Figure 4.6b (see the red circles) which indicates that the PBA-UPy7.2 film is more elastic at  $T=40\text{ }^{\circ}\text{C}$  and  $\text{RH}=0\%$  (Figure 4.5b) while it is more viscous and liquid-like at  $T=40\text{ }^{\circ}\text{C}$  and  $\text{RH}=100\%$  (Figure 4.6b). The discontinuity of the contact edge

observed in the even fringe of the FECO fringes in Figure 4.6a and 4.6b indicates formation of a meniscus during the coalescence of the two PBA-UPy7.2 films.<sup>24, 62</sup> The top-view images in Figure 4.6 further show the surface deformation at the contact boundary (interface between air and polymer neck), which is evident of the formation of transient fingering patterns associated with coalescence/detachment of viscous polymer films, as reported recently.<sup>25-27</sup>

Interesting radially or randomly parallel bands or stripe patterns (Figure 4.5c and 4.5d) and viscous fingering patterns (Figure 4.6c and 4.6d) were observed during the separation of PBA-UPy7.2 at  $T=40\text{ }^{\circ}\text{C}$ ,  $\text{RH}=0$  and  $100\%$ . It is evident from the fingering instability patterns observed at  $\text{RH}=100\%$  that the polymer becomes more viscous as the relative humidity increases which supports the results of Figure 4.3d.

The surfaces were further characterized after the contact mechanics experiments. Figure 4.7 and Figure S6 show AFM images and optical microscopy images of typical surface deformation patterns associated with detachment of PBA-UPy7.2 films at  $T=40\text{ }^{\circ}\text{C}$ ,  $\text{RH}=0\%$  and  $\text{RH}=100\%$ .

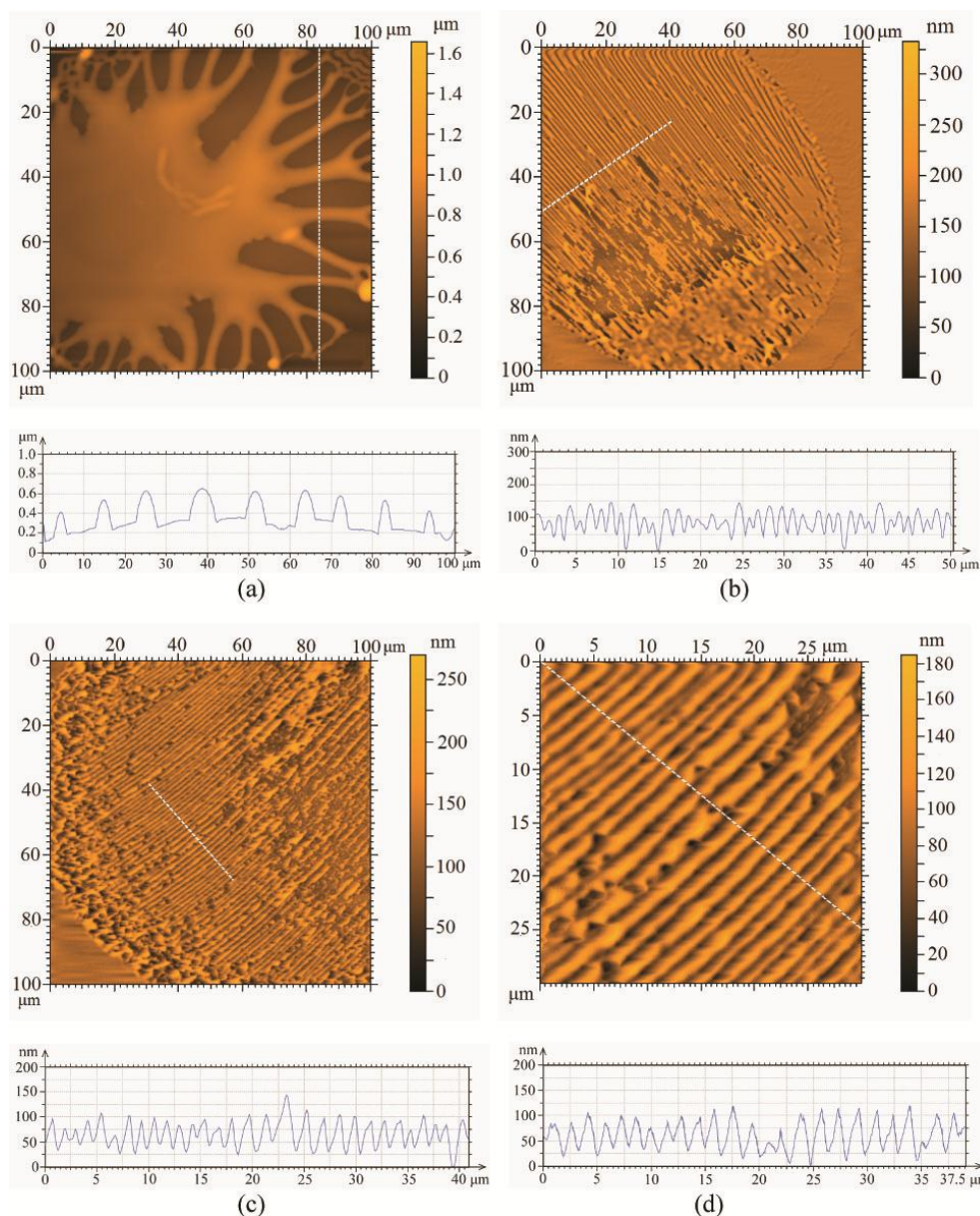


**Figure 4.7** Typical topographical AFM images of surface patterns associated with the detachment of two PBA-UPy7.2 films (of thickness ~100 nm) from adhesive contact in contact mechanics tests: (a) more viscous state, RH=100%, (b-d) more elastic state, RH=0%. The experiment temperature was  $T=40\text{ }^{\circ}\text{C}$ .

As clearly shown in Figure 4.7, the surface patterns are significantly different as the relative humidity changes. At RH=0% the surface patterns are in the form of linear and almost parallel bands or stripes while at RH=100% much larger branched radial fingers are developed. Similar fracture patterns were reported

previously for polystyrene in which radial fingering instabilities and linear parallel fractures were developed for viscous and elastic films, respectively.<sup>24, 25, 28, 63</sup> Therefore PBA-UPy7.2 undergoes a transition from elastic to viscous state failure or rupture as the relative humidity increases from RH=0% to RH=100% at T=40 °C, which corroborates our results and discussion in the previous sections.

Figure 4.7a shows that for PBA-UPy7.2 at RH=100% and T=40 °C, the viscous fingers have a typical wavelength of  $\lambda=9\pm1$   $\mu\text{m}$  with a height amplitude of about 200–300 nm. Similar fingering instabilities were previously observed during the separation of confined viscous or viscoelastic films which was attributed to a mechanism involving Saffman-Taylor (fingering) instabilities.<sup>24-26, 28, 64</sup> According to Saffman-Taylor theory<sup>65</sup> when a high viscous fluid is displaced by a low viscous fluid in a confined geometry, viscous fingers with wavelength greater than  $\lambda_c$  can occur, where  $\lambda_c$  is given by

$$\lambda_c = 2\pi h \sqrt{\gamma/12V(\eta_1 - \eta_2)} \quad (4.9)$$

where  $h$  is the gap height or confined film thickness (in SFA experiments),  $\gamma$  is the interfacial tension,  $V$  is the velocity of the moving interface, and  $\eta_1$ ,  $\eta_2$  are the viscosities of polymer and air, respectively. Using some typical values before detachment in experiments:  $h \approx 200$  nm,  $\gamma \approx 36$  mJ m<sup>-2</sup> (see table 4.2),  $V \sim 0.2\text{--}5$   $\mu\text{m s}^{-1}$ ,  $\eta_2 \approx 0$ , and  $\eta_1 \sim 10^3$  Pa•s at 40 °C and RH=100%, Equation 4.9 yields  $\lambda_c \sim 1\text{--}5$   $\mu\text{m}$  which is consistent with the experimental observation in Figure 4.7a.

In contrast Figure 4.7b-d show that the surface patterns for PBA-UPy7.2 at T=40 °C and RH=0% are parallel bands with typical wavelength of  $\lambda \sim 1$   $\mu\text{m}$  and height



amplitude of about 80–100 nm. Several previous studies on deformation of confined soft *elastic* films showed that instability patterns are different from those of *viscous* films described by Saffman-Taylor theory. Recent studies<sup>25, 28, 64, 66, 67</sup> show that the wavelength of elastic instabilities are given by  $\lambda \propto \pi h \sqrt{\gamma/Eb}$ , where  $E$  is the elastic modulus of the polymer film and  $h$  is the confined film thickness; and it was also found that the wavelength  $\lambda$  depends on confined film thickness  $h$  according to  $\lambda \sim (2.0-4.5)h$  and is independent of the crack propagation velocity. Therefore, putting  $h \approx 200$  nm yields  $\lambda \sim 900$  nm, which agrees well with the experimental value of  $\lambda \sim 1 \mu\text{m}$  shown in Figure 4.7b-d. It should be noted that similar parallel stripe patterns were also observed for PBA-UPy4.0 and PBA-UPy7.2 at  $T=23^\circ\text{C}$  and  $\text{RH}=0\%$ , indicating that the copolymers is more elastic under these conditions.

The highly self-organized surface patterns associated with the contact mechanics tests of multiple hydrogen-bonded PBA-UPy polymer films show important implications in fabricating patterned surfaces with various applications in materials science and nanotechnology.<sup>25, 28, 63</sup>

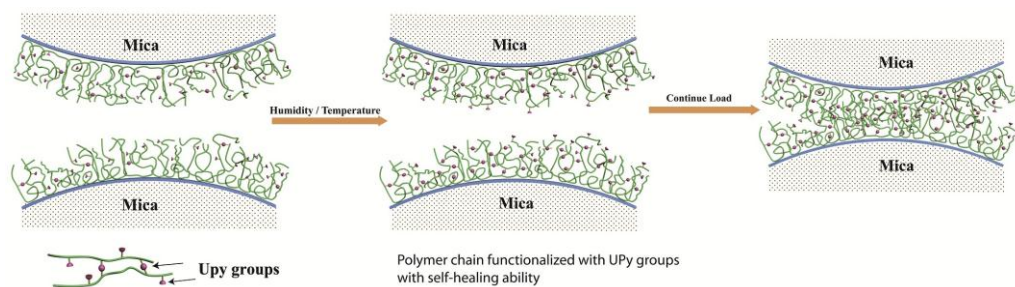


**Figure 4.8** Schematic of the adhesion mechanisms of multiple hydrogen-bonding polymers.

#### 4.4 Conclusion

The surface characteristics and adhesion properties of two self-healing polymers with quadrupole hydrogen bonding UPy groups PBA-UPy were investigated using different complementary techniques. The surface energies of PBA-UPy4.0 and PBA-UPy7.2 were estimated to be 45–56 mJ m<sup>-2</sup> under dry conditions by contact angle measurements using a three probe liquid method and also by contact and adhesion mechanics tests, which depend on the UPy content, temperature and relative humidity. These surface energies are somewhat higher than the reported literature value of  $\gamma \sim 31\text{--}34$  mJ m<sup>-2</sup> for poly (n-butyl acrylate), which is attributed to the strong UPy-UPy H-bonding interactions. We further conclude that the “effective” adhesion properties of PBA-UPy polymers are determined by the surface density of chains that can interpenetrate across the contacting interface as well as the bulk viscoelasticity of the polymers that determines their viscous forces, both of which are sensitive to humidity and temperature, as illustrated in Figure 4.8.<sup>24, 38, 45</sup> The presence of UPy functional groups can dramatically enhance the polymer adhesion mainly due to the formation of multiple hydrogen bonds at the contact interface as shown in Figure 4.8. The adhesion of PBA-UPy polymers also increases dramatically with contact time due to enhanced chain interpenetration and formation of UPy-UPy bonds at (or across) the interface. The PBA-UPy polymers show excellent self-healing ability after the two surfaces are separated and then brought back to contact multiple times, which is attributed to the reversibility, stability, long lifetime and strength of UPy-UPy bonds.<sup>18</sup> Interesting surface deformations and

fracture patterns were observed during the separation of PBA-UPy surfaces from adhesive contact. The viscous fingering patterns for PBA-UPy films at relatively high temperature and high humidity level could be well described by the Saffman-Taylor instability theory for *viscous* failure/rupture. Highly self-organized parallel stripe patterns were obtained for PBA-UPy films at relatively low temperature and low humidity level when the polymers behave more *elastic*, which shows great implications in fabricating patterned surfaces with various applications in materials science and nanotechnology. Our results provide new insights into the fundamental understanding of the adhesive mechanisms of multiple hydrogen-bonding polymers and development of novel self-healing and stimuli-responsive materials.

## 4.5 Supporting information

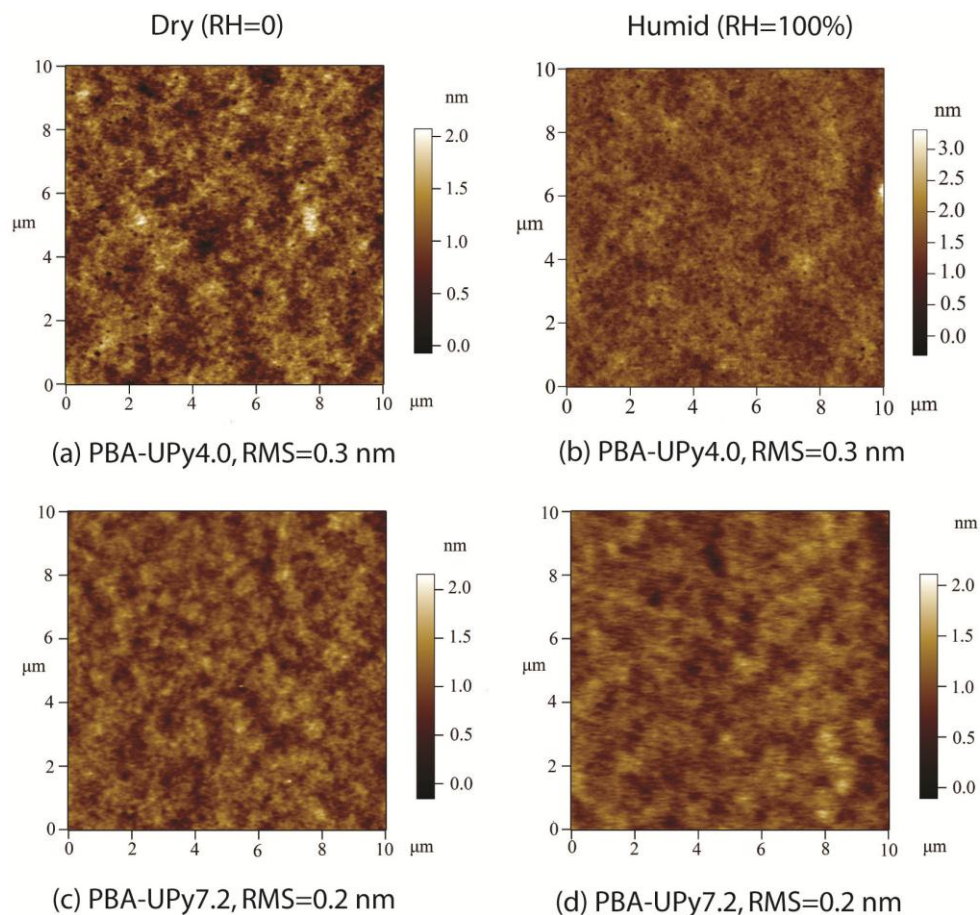


**Figure S4.1** Typical tapping mode AFM images (height) of (a, b) PBA-UPy4.0 and (c, d) PBA-UPy7.2 films of thickness 100 nm in (a, c) dry air (RH=0) and (b, d) after exposure to humid air (RH=100%).

The XPS spectra of nitrogen (N1s) for the two polymers PBA-UPy4.0 and PBA-UPy7.2 is shown in Figure S4.2. The nitrogen peak is representative of the amount of the UPy group present on the surface and as expected for polymer PBA-UPy7.2 with higher UPy content (7.2% UPy), more nitrogen is detected compared to polymer PBA-UPy4.0 (4.0% UPy).

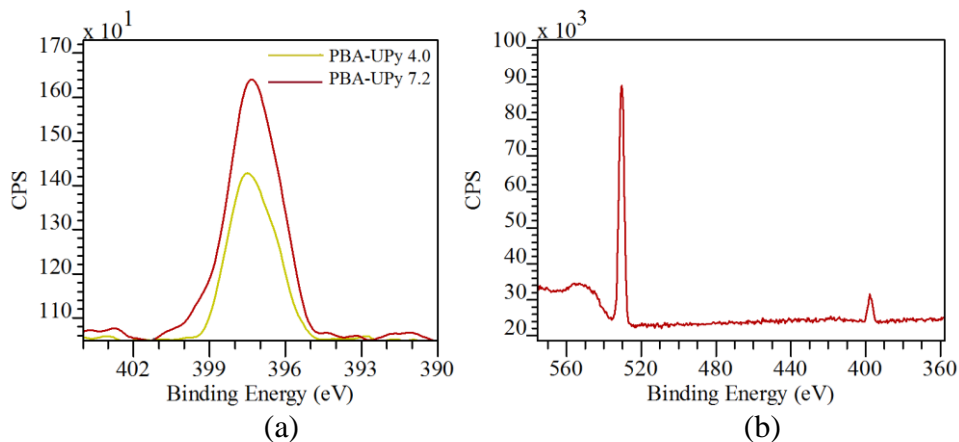


**Figure S4.2** Normalized XPS spectra of (a) nitrogen (N1s) for polymer surfaces of PBA-UPy4.0 (green curve) and PBA-UPy7.2 (red curve), and (b) nitrogen (N1s) and oxygen (O1s) for PBA-UPy7.2 surface.

The typical rupture patterns of the polymer PBA-UPy4.0 films after water contact angle measurements are shown in Figure S4.3, associated with the abrupt decrease of the contact angle.

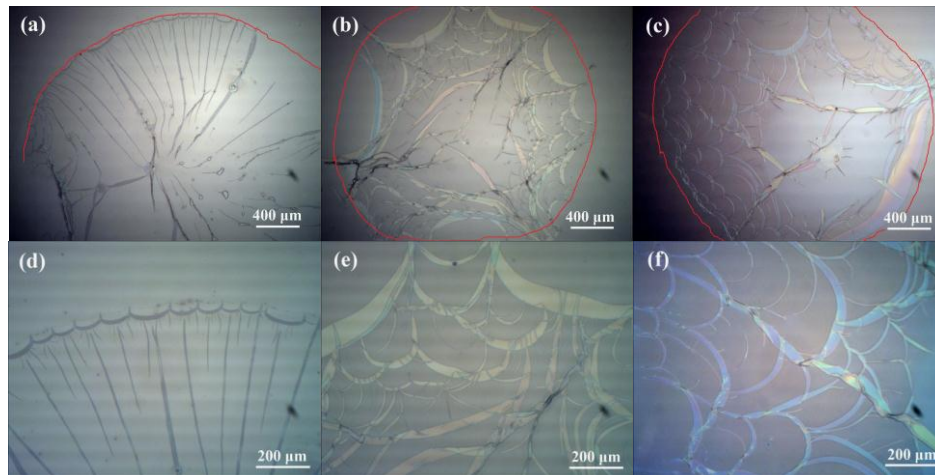


**Figure S4.3** Morphological patterns of ruptured polymer PBA-UPy4.0 films on mica after contacting with water for a time  $t > t_r$ . Film thicknesses were 25, 90, 120 nm for (a)-(c), respectively. Panels (d)-(f) are higher resolution of panels (a)-(c), respectively. The original contact boundary is shown by the red line.

The effect of polymer film thickness on rupture patterns and rupture time was also investigated (Figure S4.3 and S4.4), and the rupture time ( $t_r$ ) was defined as

the time required from the initial contact of the probe liquid and polymer film to the film rupture. The thicknesses of the polymer films in Figure S4.3a-c were ~25, 90 and 120 nm respectively. Figure S4.3 shows that different morphological patterns occurred during dewetting of the PBA-UPy4.0 films on mica, and Figure S4.3d-f are higher resolution images of Figure S4.3a-c respectively. For the rupture of very thin films, almost concentric thin ribbons were formed from the periphery of the contact area to the center (see Figure S4.3a,d). For thicker films, the fracture patterns were much more complex, and generally polygonal (Figure S4.3f) or branched-like (Figure S4.3e) patterns were observed. Similar polygonal patterns were reported previously for dewetted polystyrene thin films when heated above glass transition temperature ( $T_g$ ).<sup>68-70</sup>

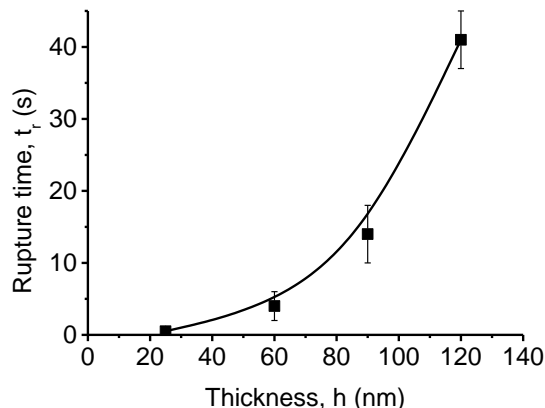


**Figure S4.4** Rupture time of polymer PBA-UPy4.0 film in contact with water droplet vs. polymer film thickness.

The rupture time was found to be strongly dependent on the polymer film thickness as shown in Figure S4.4. Very thin films (~25 nm) ruptured readily and the rupture time increased to ~40 s for films of 120 nm. For films thicker than 250 nm, the water droplet was still stable after 5 min and no obvious dewetting of the polymer films was observed.

The dewetting of thin liquid films has been studied both theoretically and experimentally and most studies were focused on polymer thin films because of their high viscosity and low vapor pressure that allow experiments within a reasonable time scale.<sup>68-78</sup> A complete theoretical simulation of the dewetting of polymer films is out of the scope of the current work. A simplified discussion is given here instead to provide some insights in understanding the surface properties of PBA-UPy4.0 films with multiple hydrogen-bonded groups. In general, a fluid-fluid interface can be considered distorted at the molecular scale due to the thermal motion of fluid molecules and presence of interfacial capillary waves. The capillary wave fluctuations are always present at the fluid-fluid interface which increase the interfacial area and are opposed and stabilized by surface tension force (see Figure S4.5a). When the liquid film thickness becomes less than ~100 nm, the intermolecular and interfacial forces across the interface and film become important. The attractive intermolecular forces (i.e. van der Waals forces) would increase the amplitude of the capillary waves and enhance the fluctuations. The stability of thin liquid films thus depends on the competition between the intermolecular attractive forces that destabilize the film and the interfacial tension and other repulsive short-range forces which tend to stabilize the interface. If the attractive interactions surpass the stabilizing interactions (i.e. surface tension), the amplitude of the interfacial fluctuation would increase (see Figure S4.5b). When the fluctuation amplitude is comparable with the film thickness, rupture of thin film starts through formation of holes within the film (see Figure S4.5c). The holes would then grow in size

due to surface tension forces that tend to retract the three-phase contact line because of high circumferential curvature which eventually leads to further dewetting of the film and formation of different morphological patterns similar to those observed in Figure S4.3 (see Figure S4.5d).<sup>70, 77</sup>

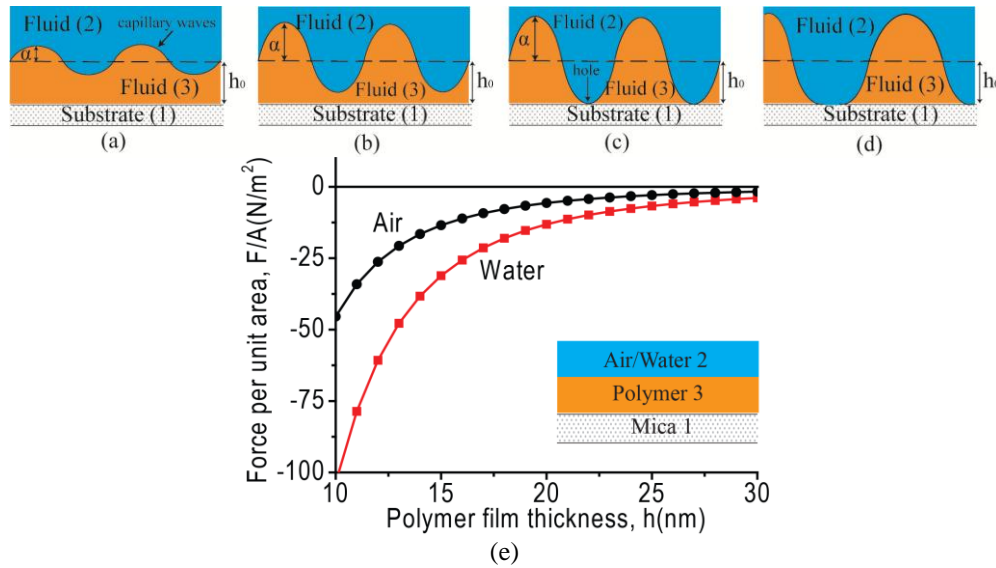


**Figure S4.5** Different stages of a thin film dewetting/rupture: (a) capillary waves always exist at the fluid-fluid interface ( $\alpha < h_0$ ); (b) capillary waves grow if the attractive interfacial forces across the interface surpass the stabilizing effects of surface tension ( $\alpha < h_0$ ); (c) rupture of the film starts through formation of holes ( $\alpha \approx h_0$ ); (d) holes grow in size due to surface tension forces leading to different morphological patterns such as polygonal and branched-like; (e) total interfacial forces between mica and air/water surfaces separated by a thin film of polymer PBA-UPy4.0.

In the current study the mica substrate (1) is separated from water (2) by a thin film of polymer (3). The interfacial interactions in this system comprised of van der Waals forces and polar interactions.<sup>71</sup> The van der Waals forces per unit area between flat surfaces of mica 1 and water 2 separated by a film of polymer 3 is given by

$$F_{vdw} = -A_{132}/6\pi D^3, \quad (S1)$$



where  $A_{132}$  is the Hamaker constant and  $D$  is the separation distance between the surfaces (i.e. polymer film thickness). The Hamaker constant  $A_{132}$  can be calculated based on Lifshitz theory as

$$A_{132} \approx \frac{3}{4} k_B T \left( \frac{\varepsilon_1 - \varepsilon_3}{\varepsilon_1 + \varepsilon_3} \right) \left( \frac{\varepsilon_2 - \varepsilon_3}{\varepsilon_2 + \varepsilon_3} \right) + \frac{3h\nu_e}{8\sqrt{2}} \frac{(n_1^2 - n_3^2)(n_2^2 - n_3^2)}{(n_1^2 + n_3^2)^{1/2} (n_2^2 + n_3^2)^{1/2} \left\{ (n_1^2 + n_3^2)^{1/2} + (n_2^2 + n_3^2)^{1/2} \right\}} \quad (S2)$$

where  $k_B$  is the Boltzmann constant,  $\varepsilon$  is the dielectric constant,  $h$  is Planck constant,  $\nu_e$  is the absorption frequency and  $n$  is the refractive index. The polar interactions decay exponentially with film thickness and is given by<sup>71, 77</sup>

$$F_{polar} = -\frac{S^P}{l^P} \exp\left(-\frac{D}{l^P}\right) \quad (S3)$$

where  $l^P$  is the characteristic decay length and  $S^P$  is the polar component of spreading coefficient. The polar component of spreading coefficient  $S^P$  can be calculated based on the acid and base components of the surface energies of the three media as<sup>71</sup> (see Table 4.1)

$$S^P = 2 \left\{ \sqrt{\gamma_3^+} \left( \sqrt{\gamma_1^-} + \sqrt{\gamma_2^-} - \sqrt{\gamma_3^-} \right) + \sqrt{\gamma_3^-} \left( \sqrt{\gamma_1^+} + \sqrt{\gamma_2^+} - \sqrt{\gamma_3^+} \right) - \sqrt{\gamma_1^+ \gamma_2^-} - \sqrt{\gamma_1^- \gamma_2^+} \right\}. \quad (S4)$$

The total interfacial forces between mica and air/water surfaces separated by a thin film of polymer PBA-UPy4.0 can be calculated as a function of polymer film thickness based on Equation S1 to S4 using  $A_{132}=2 \times 10^{-21}$  and  $8.6 \times 10^{-22}$  J for water and air, respectively, as shown in Figure S4.5e. It is clear from Figure S4.5e that for both air-polymer-mica and water-polymer-mica the interactions are attractive which suggests that the films are thermodynamically unstable.<sup>50</sup>

However the interaction is much more attractive for the water case as compared to the air case which eventually leads to film dewetting. Moreover as the polymer film thickness decreases, the attractive interactions increase dramatically, thus thinner film is more susceptible to dewetting which agrees with the experimental observations shown in Figure S4.4.

It should be noted that the above discussions apply to dewetting of *liquid* films. As shown in Figure 4.2, different from PBA-UPy4.0, no significant dewetting was observed for PBA-UPy7.2 films during contact angle measurements, which suggests that polymer PBA-UPy4.0 tends to behave more like a viscous liquid in contact with water as compared to polymer PBA-UPy7.2. This phenomenon could be further understood by the fact that the glass transition temperature of polymers PBA-UPy4.0 and PBA-UPy7.2 is  $-40\text{ }^{\circ}\text{C}$  and  $-29\text{ }^{\circ}\text{C}$  respectively, while the UPy-UPy bond lifetime was  $\sim 3$  and  $20\text{ s}$  for PBA-UPy4.0 and PBA-UPy7.2, respectively.<sup>79</sup> Therefore the relaxation of the polymer molecules and fluctuations of polymer film is much faster for PBA-UPy4.0 than that of PBA-UPy7.2 during contact angle measurement at room temperature (viz. water-polymer-substrate interaction and hydrogen bonding formation between water molecules and UPy groups at the polymer-water interface).<sup>79</sup> It should be noted that thermodynamically, dewetting could eventually occur for both PBA-UPy4.0 and PBA-UPy7.2 films however with quite different time scales.

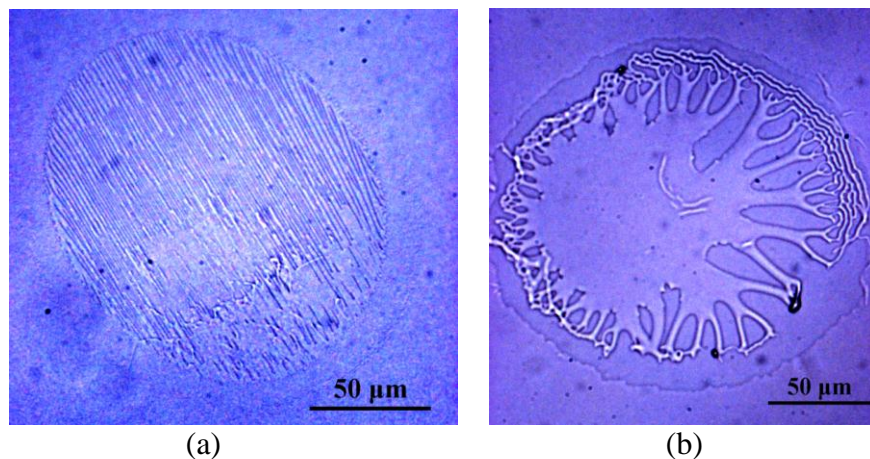


**Figure S4.6** Microscope images of typical surface patterns (parallel or radial stripes) associated with detachment from adhesive contact of (a) more elastic polymer films (PBA-UPy7.2 at  $T=40\text{ }^{\circ}\text{C}$ ,  $\text{RH}=0\%$ ) and (b) more viscous polymer films (PBA-UPy7.2 at  $T=40\text{ }^{\circ}\text{C}$ ,  $\text{RH}=100\%$ ). Polymer film thickness  $\sim 100\text{ nm}$ .

## References

- (1) T. Annable, R. Buscall, R. Ettelaie, *Colloids Surf. , A*. **1996**, *112*, 97-116.
- (2) K. C. Tam, R. D. Jenkins, M. A. Winnik, D. R. Bassett, *Macromolecules*. **1998**, *31*, 4149-4159.
- (3) R. P. Sijbesma, F. H. Beijer, L. Brunsveld, B. J. B. Folmer, J. J. Hirschberg, R. F. M. Lange, J. K. L. Lowe, E. W. Meijer, *Science*. **1997**, *278*, 1601-1604.
- (4) S. Sivakova, D. A. Bohnsack, M. E. Mackay, P. Suwanmala, S. J. Rowan, *J. Am. Chem. Soc.* **2005**, *127*, 18202-18211.
- (5) P. Cordier, F. Tournilhac, C. Soulie-Ziakovic, L. Leibler, *Nature*. **2008**, *451*, 977-980.
- (6) D. Montarnal, F. Tournilhac, M. Hidalgo, J. Couturier, L. Leibler, *J. Am. Chem. Soc.* **2009**, *131*, 7966-7967.

- (7) a) K. E. Feldman, M. J. Kade, E. W. Meijer, C. J. Hawker, E. J. Kramer, *Macromolecules*. **2009**, *42*, 9072-9081; b) K. E. Feldman, M. J. Kade, E. W. Meijer, C. J. Hawker, E. J. Kramer, *Macromolecules*. **2010**, *43*, 5121-5127.
- (8) K. E. Feldman, M. J. Kade, de Greef, T. F. A., E. W. Meijer, E. J. Kramer, C. J. Hawker, *Macromolecules*. **2008**, *41*, 4694-4700.
- (9) J. B. Beck, S. J. Rowan, *J. Am. Chem. Soc.* **2003**, *125*, 13922-13923.
- (10) W. Weng, J. B. Beck, A. M. Jamieson, S. J. Rowan, *J. Am. Chem. Soc.* **2006**, *128*, 11663-11672.
- (11) H. Zeng, D. S. Hwang, J. N. Israelachvili, J. H. Waite, *Proc. Natl. Acad. Sci. U. S. A.* **2010**, *107*, 12850-12853.
- (12) J. N. Hunt, K. E. Feldman, N. A. Lynd, J. Deek, L. M. Campos, J. M. Spruell, B. M. Hernandez, E. J. Kramer, C. J. Hawker, *Adv. Mater.* **2011**, *23*, 2327-2331.
- (13) S. I. Stupp, V. LeBonheur, K. Walker, L. S. Li, K. E. Huggins, M. Keser, A. Amstutz, *Science*. **1997**, *276*, 384-389.
- (14) A. M. Kumar, S. Sivakova, R. E. Marchant, S. J. Rowan, *Small*. **2007**, *3*, 783-787.
- (15) L. Bouteiller, *Adv. Polym. Sci.* **2007**, *207*, 79-112.
- (16) M. M. Caruso, D. A. Davis, Q. Shen, S. A. Odom, N. R. Sottos, S. R. White, J. S. Moore, *Chem. Rev.* **2009**, *109*, 5755-5798.
- (17) T. F. De Greef, M. M. Smulders, M. Wolffs, A. P. Schenning, R. P. Sijbesma, E. W. Meijer, *Chem. Rev.* **2009**, *109*, 5687-5754.
- (18) T. F. de Greef, E. W. Meijer, *Nature*. **2008**, *453*, 171-173.

- (19) E. B. Murphy, F. Wudl, *Prog. Polym. Sci.* **2010**, *35*, 223-251.
- (20) P. Y. W. Dankers, Z. Zhang, E. Wisse, D. W. Grijpma, R. P. Sijbesma, J. Feijen, E. W. Meijer, *Macromolecules*. **2006**, *39*, 8763-8771.
- (21) van Beek, D. J. M., A. J. H. Spiering, G. W. M. Peters, K. Nijenhuis, R. P. Sijbesma, *Macromolecules*. **2007**, *40*, 8464-8475.
- (22) N. Maeda, N. Chen, M. Tirrell, J. N. Israelachvili, *Science*. **2002**, *297*, 379-382.
- (23) N. Chen, N. Maeda, M. Tirrell, J. Israelachvili, *Macromolecules*. **2005**, *38*, 3491-3503.
- (24) H. Zeng, N. Maeda, N. Chen, M. Tirrell, J. Israelachvili, *Macromolecules*. **2006**, *39*, 2350-2363.
- (25) H. Zeng, Y. Tian, B. Zhao, M. Tirrell, J. Israelachvili, *Macromolecules*. **2007**, *40*, 8409-8422.
- (26) H. Zeng, B. Zhao, Y. Tian, M. Tirrell, L. G. Leal, J. N. Israelachvili, *Soft Matter*. **2007**, *3*, 88-93.
- (27) H. Zeng, Y. Tian, B. Zhao, M. Tirrell, J. Israelachvili, *Langmuir*. **2007**, *23*, 6126-6135.
- (28) H. Zeng, B. Zhao, J. N. Israelachvili, M. Tirrell, *Macromolecules*. **2010**, *43*, 538-542.
- (29) J. N. Israelachvili, *Intermolecular and Surface Forces*, 3rd edn., Academic Press **2011**.
- (30) D. Leckband, J. Israelachvili, *Q. Rev. Biophys.* **2001**, *34*, 105-267.
- (31) J. N. Israelachvili, *J. Colloid Interface Sci.* **1973**, *44*, 259-272.

- (32) C. J. van Oss, M. K. Chaudhury, R. J. Good, *Adv. Colloid Interface Sci.* **1987**, 28, 35-64.
- (33) J. N. Israelachvili, P. M. McGuiggan, *J. Mater. Res.* **1990**, 5, 2223-2231.
- (34) J. Israelachvili, Y. Min, M. Akbulut, A. Alig, G. Carver, W. Greene, K. Kristiansen, E. Meyer, N. Pesika, K. Rosenberg, H. Zeng, *Rep. Prog. Phys.* **2010**, 73, 1-16.
- (35) H. Zeng, Y. Tian, T. H. Anderson, M. Tirrell, J. N. Israelachvili, *Langmuir.* **2008**, 24, 1173-1182.
- (36) A. Faghihnejad, H. Zeng, *Soft Matter.* **2012**, 8, 2746-2759.
- (37) F. Teng, H. Zeng, Q. Liu, *J. Phys. Chem. C.* **2011**, 115, 17485-17494.
- (38) H. Zeng, *Polymer adhesion, friction and lubrication*, Wiley **2013**.
- (39) D. Ahn, K. R. Shull, *Langmuir.* **1998**, 14, 3646-3654.
- (40) R. G. Horn, J. N. Israelachvili, F. Pribac, *J. Colloid Interface Sci.* **1987**, 115, 480-492.
- (41) H. R. Hertz, *Miscellaneous Papers* **1896**, 340.
- (42) K. L. Johnson, K. Kendall, A. D. Roberts, *Proc. R. Soc. London, Ser. A.* **1971**, 324, 301-313.
- (43) B. V. Derjaguin, V. M. Muller, Y. P. Toporov, *J. Colloid Interface Sci.* **1975**, 53(2), 314-326.
- (44) D. Maugis, *J. Colloid Interface Sci.* **1992**, 150, 243-269.
- (45) H. Zeng, M. Tirrell, J. Israelachvili, *J. Adhes.* **2006**, 82, 933-943.
- (46) J. Brandrup, E. H. Immergut, E. A. Grulke, A. Abe, D. R. Bloch, *Polymer Handbook*, Wiley **2005**.

- (47) H. Sun, H. H. Lee, I. Blakey, B. Dargaville, T. V. Chirila, A. K. Whittaker, S. C. Smith, *J. Phys. Chem. B* **2011**, *115*, 11053-11062.
- (48) R. M. Barrer, E. K. Rideal, *Trans. Faraday Soc.* **1939**, *35*, 628-643.
- (49) G. J. Van Amerongen, *Journal of Polymer Science*. **1950**, *5*, 307-332.
- (50) S. Prager, F. A. Long, *J. Am. Chem. Soc.* **1951**, *73*, 4072-4075.
- (51) P. Meares, *J. Am. Chem. Soc.* **1954**, *76*, 3415-3422.
- (52) A. S. Michaels, R. B. Parker, *J. Polym. Sci.* **1959**, *41*, 53-71.
- (53) K. E. Feldman, PhD thesis, University of California, Santa Barbara **2009**.
- (54) K. Kendall, *Science*. **1994**, *263*, 1720-1725.
- (55) C. -Y. Hui, J. M. Baney, E. J. Kramer, *Langmuir*. **1998**, *14*, 6570-6578.
- (56) M. O. Robbins, D. Andelman, J. F. Joanny, *Phys. Rev. A*. **1991**, *43*, 4344-4354.
- (57) E. Barthel, G. Haiat, *Langmuir*. **2002**, *18*, 9362-9370.
- (58) B. Q. Luan, M. O. Robbins, *Nature*. **2005**, *435*, 929-932.
- (59) J. A. Greenwood, K. L. Johnson, *J. Colloid Interface Sci.* **2006**, *296*, 284-291.
- (60) L. Leger, J. F. Joanny, *Rep. Prog. Phys.* **1992**, *55*, 431-486.
- (61) C. Creton, E. J. Kramer, H. R. Brown, C. Y. Hui, *Adv. Polym. Sci.* **2002**, *156*, 53-136.
- (62) H. Zeng, Y. Tian, B. X. Zhao, M. Tirrell, J. Israelachvili, *Langmuir*. **2009**, *25*, 4954-4964.
- (63) L. F. Pease, P. Deshpande, Y. Wang, W. B. Russel, S. Y. Chou, *Nat. Nanotechnol.* **2007**, *2*, 545-548.

- (64) J. Nase, A. Lindner, C. Creton, *Phys. Rev. Lett.* **2008**, *101*, 074503.
- (65) P. G. Saffman, G. Taylor, *Proc. R. Soc. London, Ser. A.* **1958**, *245*, 312-329.
- (66) V. Shenoy, A. Sharma, *Phys. Rev. Lett.* **2001**, *86*, 119-122.
- (67) A. Ghatak, M. K. Chaudhury, *Langmuir.* **2003**, *19*, 2621-2631.
- (68) G. Reiter, *Phys. Rev. Lett.* **1992**, *68*, 75-78.
- (69) G. Reiter, *Langmuir.* **1993**, *9*, 1344-1351.
- (70) A. Sharma, G. Reiter, *J. Colloid Interface Sci.* **1996**, *178*, 383-399.
- (71) A. Sharma, *Langmuir.* **1993**, *9*, 861-869.
- (72) P. Lambooy, K. C. Phelan, O. Haugg, G. Krausch, *Phys. Rev. Lett.* **1996**, *76*, 1110-1113.
- (73) A. M. Higgins, R. A. L. Jones, *Nature.* **2000**, *404*, 476-478.
- (74) R. Seemann, S. Herminghaus, K. Jacobs, *Phys. Rev. Lett.* **2001**, *86*, 5534-5537.
- (75) J. Sarkar, A. Sharma, *Langmuir.* **2010**, *26*, 8464-8473.
- (76) S. Y. Choi, C. Lee, J. W. Lee, C. Park, S. H. Kim, *Macromolecules.* **2012**, *45*, 1492-1498.
- (77) R. Mukherjee, in *Mechanics Over Micro and Nano Scales* (Ed: S. Chakraborty), Springer **2011**, pp. 193-215.
- (78) A. Sharma, *Eur. Phys. J. E.* **2003**, *12*, 397-408.
- (79) K. E. Feldman, M. J. Kade, E. W. Meijer, C. J. Hawker, E. J. Kramer, *Macromolecules.* **2009**, *42*, 9072-9081.



## Chapter 5. Conclusion

In order to study the hydrophobic interactions between polymer surfaces, SFA was coupled with a top-view optical microscope and used to measure the forces between two PS surfaces in different electrolyte solutions of different concentrations from 0.001 to 1.0 M. A long-range attraction of 100-300 nm was measured between two PS surfaces which was found to be due to the bridging of microscopic and sub-microscopic bubbles on PS surfaces. The measured attraction depended on the electrolyte type and concentration as for NaCl and CaCl<sub>2</sub> the range of attraction reduced to <40 nm as the concentration increased to 1.0 M while HCl and CH<sub>3</sub>COOH showed no significant change. The observed ion specificity is due to the ion-pair complex adsorption at the bubble/solution interface. The electrolyte ions that are depleted from the air/water interface (i.e. NaCl, CaCl<sub>2</sub>), tend to increase the surface tension of water, decrease air solubility and suppress the formation and stability of air bubbles on PS surfaces and thus decrease the range of the hydrophobic attraction. In contrast, the electrolyte ions that tend to adsorb at the air/water interface (i.e. HCl, CH<sub>3</sub>COOH), would increase the surface tension of water and air solubility and does not affect the formation and stability of air bubbles on PS surfaces and the hydrophobic interactions. The range of the hydrophobic interaction significantly reduced to <20 nm upon degassing the solutions and the analysis of top-view optical microscope and SFA images showed that the possible mechanisms could be either the spontaneous cavitation of water between hydrophobic surfaces or bridging of nanoscopic bubbles. The surface deformation patterns associated

with the separation of PS surfaces from contact in aqueous solutions were investigated and it was found that the cracks initiated from the periphery of the contact area where the stress is maximum according to contact mechanics theories. The corresponding interfacial energy of PS in aqueous solutions was found to be  $\gamma = 42 \pm 5 \text{ mJ/m}^2$  which is very close to the measured values in air 35-43  $\text{mJ/m}^2$ . A three-regime hydrophobic interaction model was proposed comprised of (1) very long-range attraction from  $\sim 20 \text{ nm}$  to hundreds of nanometers due to bridging of microscopic and sub-microscopic bubbles, (2) the intermediate regime (from 10 to 20 nm) due to bridging of nanoscopic bubbles, or enhanced Hamaker constant or cavitation of water and (3) a short-range regime (from  $<1 \text{ nm}$  to several nanometers) due to water structure changes near hydrophobic surfaces or particles.

The interactions between hydrophobic and hydrophilic molecules, particles or surfaces occur in many biological phenomena and industrial processes. In this work, polystyrene (PS) and mica were chosen as a model system to investigate the interaction mechanism between hydrophilic and hydrophobic surfaces. Using a surface forces apparatus (SFA) coupled with a top-view optical microscope, interaction forces between PS and mica surfaces were directly probed in five different electrolyte solutions (*i.e.*, NaCl,  $\text{CaCl}_2$ , NaOH, HCl and  $\text{CH}_3\text{COOH}$ ) of various concentrations. Long-range repulsion of  $\sim 50\text{-}100 \text{ nm}$  was observed in low electrolyte concentration (e.g. 0.001 M) which was mainly due to the presence of microscopic and sub-microscopic bubbles on PS surface. A modified DLVO theory well fits the interaction forces by taking

into account the effect of bubbles on PS surface. The range of the repulsion was dramatically reduced in 1.0 M solutions of NaCl, CaCl<sub>2</sub> and NaOH, but did not significantly change in 1.0 M HCl and CH<sub>3</sub>COOH, which was due to ion specificity effect on the formation and stability of bubbles on PS surface. The range of repulsion was also significantly reduced to <15 nm in degassed electrolyte solutions. UV-ozone treatment changed the hydrophobic attraction of untreated PS-PS to pure repulsion between untreated PS and treated PS, and the range of repulsion increased with increasing the hydrophilicity of treated PS surface, demonstrating the important role of surface hydrophobicity on the formation and stability of bubbles on substrates. Our results indicate that DLVO forces dominate the interaction between hydrophilic surface (i.e. mica) and hydrophobic polymer (i.e. PS), while the types of electrolytes (ion specificity), electrolyte concentration, degassing and surface hydrophobicity can significantly affect the formation and stability of bubbles on the interacting surfaces, thus affecting the range and magnitude of the interaction forces.

In order to study the effect of hydrogen bonding on the surface interactions of polymers, the adhesion mechanism and surface properties of functionalized poly(butyl acrylate) (PBA) containing a quadruple hydrogen bonding group called '2-ureido-4[1*H*]-pyrimidinone' (UPy) were investigated using several complementary techniques such as a surface forces apparatus (SFA) coupled with a top-view optical microscope and an atomic force microscope (AFM). The adhesion and mechanical properties of PBA-UPy were found to be significantly enhanced by the UPy groups and strongly depend on

the temperature, relative humidity in air and contact time. Interesting surface deformations and fracture patterns were observed during the contact and separation of PBA-UPy films at different temperatures and relative humidity levels. The viscous fingering patterns could be well described by the viscous Saffman-Taylor instability theory. While the highly self-organized parallel stripe patterns obtained in more elastic state shows great implications in fabricating patterned surfaces with various applications in materials science and nanotechnology. The interesting adhesion properties and self-healing capability offer the multiple hydrogen-bonded PBA-UPy polymers great potential as novel self-healing and stimuli-responsive coatings, adhesives and functional composites. Results of this study provide new insights into fundamental understanding of the role of hydrophobic effect and hydrogen bonding on polymer surface interactions. Nevertheless many challenges are open to be addressed in future studies. The effect of pH, temperature, 'complete' degassing of the solution and molecular weight of the polymer on hydrophobic interactions of polymer surfaces should be considered in future studies. The role of bubbles and specific ion adsorption at the air-water interface can be further investigated by molecular dynamics simulations and spectroscopic methods such as second harmonic generation. The role of hydrogen bonding on polymer surface interactions can be further studied in different electrolyte solutions. Finally, as many polymers have both hydrophobic and hydrogen bonding moieties, the systematic study of surface interactions of such model polymers can provide new

insights into many surface and colloidal phenomena where proteins and complex macromolecules are involved.